QUANTITATIVE BIOLUMINESCENCE TOMOGRAPHY: HARDWARE AND SOFTWARE DEVELOPMENT FOR A MULTI-MODAL OPTICAL IMAGING SYSTEM

by

SHELLEY LOUISE TAYLOR

A thesis submitted to
The University of Birmingham
for the degree of
DOCTOR OF PHILOSOPHY

PSIBS Doctoral Training Centre
College of Engineering and Physical Sciences
University of Birmingham

June 2017

Abstract

Bioluminescence imaging (BLI) is widely used in pre-clinical research to monitor the location and migration of different cell types, and the growth of cancerous tumours and response to treatments within murine models. However, the quantitative accuracy of the technique is limited. The position of the animal is known to affect the measured bioluminescence, with a change in position causing a change in measurement. Work presented here will address this problem, validating a free space model in a murine model to produce surface bioluminescence measurements which are independent of the position of the animal.

The position of the source within the animal and the underlying tissue attenuation also affect the quantitative accuracy of bioluminescence measurements. An extension to bioluminescence imaging, bioluminescence tomography (BLT), aims to overcome these problems by recovering the three-dimensional distribution of the source within the animal. However, there are limitations to the quantitative accuracy of BLT. Current reconstruction algorithms ignore the bandwidth of band pass filters used for multi-spectral data collection for BLT. This work develops a model which accounts for filter bandwidth in the BLT reconstruction. Simulation data shows that when ignoring bandwidth the intensity of a bioluminescent source reconstructed assuming a bandwidth of 20 nm is $\sim 20\times$ that reconstructed assuming a bandwidth of 1 nm. When the filter bandwidth was accounted for in the reconstruction this variation is reduced to $\sim 0.9\times$. When applied experimentally to data taken using a multi-modal optical imaging system using a mouse-shaped phantom, the variation in intensity is reduced from

$\sim 5\times$ to $\sim 1.5\times$ when considering data acquired using filters of bandwidth 10 and ~ 20 nm. The model is also validated in a *post mortem* murine model with the intensity of the recovered sources quantitatively comparable to the target source intensity, and two orders of magnitude lower than the sources recovered ignoring the bandwidth. These results all demonstrate the increased quantitative accuracy achieved when using the filter bandwidth model presented in this thesis.

An additional limitation to the quantitative accuracy of BLT is that accurate knowledge of the optical properties of the animal are required but are difficult to acquire. Work to improve the quantitative accuracy by obtaining subject-specific optical properties through use of a spectral derivative reconstruction method for diffuse optical tomography (DOT) is presented. The model thus far has not been applied to measurements acquired using a non-contact imaging system. The efficacy of the spectral derivative method as applied to non-contact data is demonstrated through simulation using a heterogeneous mouse model, and experimentally using a *post mortem* murine model. In both cases the recovered optical properties are used as prior knowledge for BLT source recovery, producing promising results for the application of the spectral derivative method *in vivo*.

"If a thing is worth doing, it is worth doing well.

If it is worth having, it is worth waiting for.

If it is worth attaining, it is worth fighting for.

If it is worth experiencing, it is worth putting aside time for."

Oscar Wilde

Acknowledgments

I have a huge number of people to thank for help, support and collaboration over the course of my PhD, without whom this thesis would not have been possible. The progression and success of the work presented in this thesis is in a large part due to the training and supervision I received. Firstly to my primary supervisor Hamid Dehghani, thank you for going above and beyond what was required of you, for pushing me way out of my comfort zone and always being there for advice and support when I needed it. I thank my secondary supervisor, Iain Styles, for discussion, guidance and always being available when a third pair of eyes were needed. Thank you to Mark Cobbold, my third supervisor for the first 12 months of my PhD, for biological input and your enthusiasm about my work. Thanks also for allowing me to move the imaging system to your labs in the Medical School to enable me to start doing animal work. Philip Newsome took over the role of third supervisor when Mark took up a position at Harvard Medical School and I thank him for stepping in at short notice.

I can't thank James Guggenheim enough - he built the imaging system discussed in this thesis during his PhD and wrote the algorithms on which the work in this thesis is based. He was always on hand for help and advice even though he had moved on to pastures new. Similarly, I would like to thank Hector Basevi, who developed the surface capture component of the imaging system with James, for advice and many valuable discussions.

Manuela Carvalho Gaspar and Tracey Perry (Post-Doctoral researcher and Research Assistant respectively in Mark Cobbold's group) spent hours with me, showing me how they

performed pre-clinical bioluminescence imaging of cancer models and let me be involved with their work. They were both invaluable when I started doing animal work and were always there to help me and give me advice.

Thanks must also go to Caroline Chadwick, who runs the Biomedical Services Unit. Caroline, along with Rob Shaw and Dale Taylor, arranged for the imaging system to be moved into the Biomedical Services Unit with a view to using the system for *in vivo* imaging in the future. Caroline worked closely with us and was extremely accommodating and interested in helping with the progression of this work, and through Julie Smith provided the animals used for the work presented in this thesis.

To all members of the Imaging Group, thank you for endless discussion and advice and for being great office mates. Special thanks to Suzie and Sophie who also helped with data collection and initial work on the filter bandwidth work presented in Chapter 4.

Thank you to all past and present members of the Physical Sciences for Imaging in the Biomedical Sciences (PSIBS) Centre for Doctoral Training. My thanks to both the students and staff, for teaching and support throughout the last four years, and for providing such a friendly environment to spend so much time in. Particular thanks go to my PSIBS ladies who became great friends throughout this experience and have always been available for coffee and cake!

I must also thank my colleagues at my new job at the Royal Preston Hospital for being so understanding and supportive whilst I have been writing up and starting a new job at the same time. They have all made this last 6 months much easier to cope with.

Finally I thank my parents Liz and Mick and my boyfriend Mike, for endless support, understanding and pep talks. This whole experience would have been much more difficult without your support. Thank you for everything you all do for me.

Funding for this work was provided by the Engineering and Physical Sciences Research Council (EPSRC) via grant EP/F50053X/1 through the PSIBS Centre for Doctoral Training.

Publications

Journal Papers

The incorporation of filter bandwidth modelling into the bioluminescence tomography reconstruction algorithm presented in Chapter 4 was published in the paper:

Shelley L. Taylor, Suzannah K. G. Mason, Sophie L. Glinton, Mark Cobbold and Hamid Dehghani; "Accounting for filter bandwidth improves the quantitative accuracy of bioluminescence tomography", *Journal of Biomedical Optics* 20(9), 096001 (September 2015)

Conference Proceedings

The data presented in Chapter 4 on the effect of using fewer wavelengths for multi-spectral data collection for BLT, and including filter bandwidth modelling in the BLT reconstruction was presented (poster presentation) at SPIE Photonics West 2015 and published in the manuscript:

Shelley L. Taylor, Suzannah Mason, Sophie Glinton, Mark Cobbold, Iain B. Styles and Hamid Dehghani; "Optimisation of Acquisition Time in Bioluminescence Imaging;" *Proc. SPIE 9319*, Optical Tomography and Spectroscopy of Tissue XI, 93191T (March 5, 2015)

The application of the Free Space Model to murine data presented in Chapter 3 was presented (oral presentation) at the European Conferences on Biomedical Optics (ECBO) 2015, and published in the manuscript:

Shelley L. Taylor, Tracey A. Perry, Iain B. Styles, Mark Cobbold and Hamid Dehghani; "Accounting for Systematic Errors in Bioluminescence Imaging to Improve Quantitative Accuracy;" *Proc. SPIE 9538*, Diffuse Optical Imaging V, 95380J (July 16, 2015)

The application of the Free Space Model to phantom and murine data, along with other murine BLT data not presented in this thesis, was presented (poster presentation) at the World Molecular Imaging Congress (WMIC) 2015. The abstract submitted to the conference was as follows:

Shelley L. Taylor, Tracey A. Perry, Iain B. Styles, Mark Cobbold and Hamid Dehghani; "Advancing Bioluminescence Imaging and Tomography Toward a True Quantitative Imaging Modality for Reliable Pre-Clinical Studies," paper P702

Development of the diffuse optical imaging component of the imaging system presented in Chapter 6 was presented (oral presentation) at the OSA Biomedical Optics Congress 2016:

Shelley L. Taylor, Philip N. Newsome and Hamid Dehghani; "Development of a Multi-Modal Optical Imaging System;" Biomedical Optics 2016, OSA Technical Digest (online) (Optical Society of America, 2016), paper OTu2C.2

Contents

List of Figures

List of Tables

List of Abbreviations and Acronyms

BLDOT - Bioluminescence Tomography and Diffuse Optical Tomography imaging system

BLI - Bioluminescence Imaging

BLT - Bioluminescence Tomography

CCD - Charge Coupled Device

CSCG - Compressive Sensing Conjugate Gradient

CT - X-ray Computed Tomography

deoxyHb - Deoxyhaemoglobin

DLIT - Diffuse Luminescence Imaging Tomography

DOT - Diffuse Optical Tomography

DOT-BLT - combined Diffuse Optical Tomography and Bioluminescence Tomography

FEM - Finite Element Method

FLI - Fluorescence Imaging

FLT - Fluorescence Tomography

fluc - Firefly Luciferase

fMRI - Functional Magnetic Resonance Imaging

FOV - Field of View

FWHM - Full Width at Half Maximum

HbO - Oxyhaemoglobin

IRF - Instrument Response Function

IVIS - IVIS Spectrum *In Vivo* Imaging System

LED - Light Emitting Diode

MRI - Magnetic Resonance Imaging

NBW - Narrow Bandwidth (when referring to the NBW Jacobian model)

NIR - Near Infrared

NMR - Nuclear Magnetic Resonance

NS - Normal Spectral

NSR - Normal Spectral Region-Based

PAT - Photoacoustic Tomography

PET - Positron Emission Tomography

RF - Radiofrequency

ROI - Region of Interest

SD - Spectral Derivative

SDR - Spectral Derivative Region-Based

SNR - Signal-to-noise Ratio

SPECT - Single Photon Emission Computed Tomography

US - Ultrasound

WBW - Wide Bandwidth (when referring to the WBW Jacobian model)

Chapter 1

Introduction to Pre-Clinical Imaging

Pre-clinical studies use animal models to study the progression of a disease or efficacy of a potential clinical therapy *in vivo* before moving forward to full in-human clinical trials. They are vital for developing understanding of disease behaviour and the efficacy of novel drugs and treatments *in vivo*, following preliminary *in vitro* and *ex vivo* studies. Further developments to a treatment can then be made before proceeding to clinical trials and finally clinical use. It is important to understand the behaviour of a certain condition or treatment *in vivo* and animal models provide a complex environment in which to develop this understanding.

Imaging is an effective way to anatomically or functionally monitor disease progression and response to treatment noninvasively during pre-clinical studies. Traditionally studies into cancerous tumour growth for example, involved using a group of animals, all injected with cancer cells at the same time point. To assess tumour growth, animals were sequentially sacrificed and the tumour in each animal measured with calipers [1, 2]. This introduced inter-animal variability, as the tumour measurement at each time point was made using a different animal, as well as ethical issues in using a large number of animals. Imaging, such as: magnetic resonance imaging (MRI); X-ray computed tomography (CT) or bioluminescence imaging (BLI), enables the same study to be performed using a reduced number of animals,

as the growth of the tumour in each animal can be monitored longitudinally throughout the experimental timescale. Therefore, imaging reduces the number of animals used in the experiment and removes the inter-animal variability of tumour growth, with each animal acting as a self-control, which can improve the quantitative accuracy of the pre-clinical study [1, 2].

This chapter will provide an overview of pre-clinical imaging techniques relevant to this work: BLI, bioluminescence tomography (BLT) and diffuse optical tomography (DOT); and a brief review of bioluminescence imaging systems, before a comparison of BLI and BLT with other commonly used pre-clinical imaging modalities is made.

1.1 Pre-Clinical Imaging Techniques Relevant to this Work

1.1.1 Bioluminescence Imaging (BLI)

Bioluminescence imaging involves labelling cells of interest, for example cancer cells or stem cells, with a bioluminescent reporter gene which emits light when a substrate is introduced. Luciferases are often used as the bioluminescent source, these enzymes emit light through a metabolic reaction, as described by simplified Eq. 1.1 [3, 4].

$$Luciferase + Luciferin + ATP + O_2 \longrightarrow Light + oxyluciferin \tag{1.1}$$

The process by which firefly luciferase (fluc) emits light is detailed in ref. [5]. Images of the light which reaches the surface of the animal (via diffuse propagation through tissue, as shown in Fig. 1.1) are taken, enabling the intensity or radiance to be measured and can be used to gain information about the number of cells which are bioluminescently labelled. BLI has many applications, for example in investigations of: the growth of cancerous tumours and their response to treatments [1, 4, 6–12]; migration and location of stem cells [13–15];

immune cells [12, 16, 17]; bacteria [18–21] and viruses [19, 22, 23].

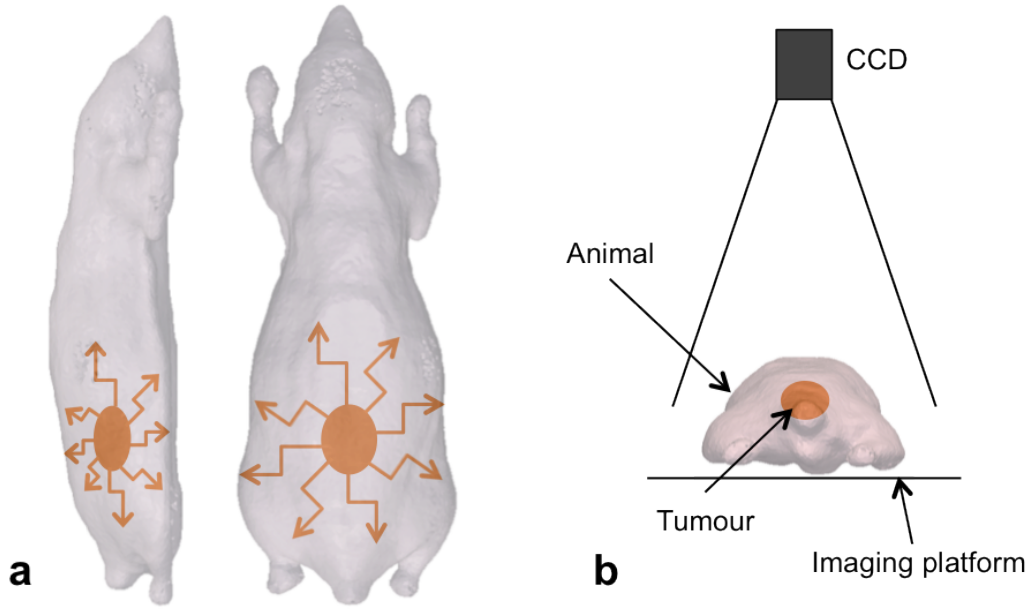

Figure 1.1: Diagram to demonstrate BLI in a murine model. (a) Schematic of diffuse propagation of bioluminescent light through tissue from a tumour. (b) BLI set-up, typically an animal will be placed on an imaging platform with a CCD camera positioned above to capture images of the bioluminescent light which has reached the surface of the animal.

A study performed by Jenkins *et al.* in 2003 demonstrated the ability of BLI to monitor tumour growth and effect of treatment in a murine model [1]. Prostate cancer cells were injected subcutaneously into the left flank of the mice. The size of the subcutaneous tumours was measured at intervals over the course of 35 days using calipers and the volume calculated from these measurements (measurement timeline shown in Fig. 1.2). Bioluminescence images were also taken using an IVIS imaging system (Perkin Elmer) enabling the bioluminescent signal to be monitored over the time-course of the experiment and therefore the growth of the tumour to be monitored via the BLI measurement variation.

Fig. 1.2 A shows BLI images of mice from 0 to 28 days after injection of cells, without treatment ('Vehicle') and with two different treatments: 5-FU which inhibits tumour growth, and Mitomycin C which causes tumour regression [1]. As is seen in Fig. 1.2 A and B the

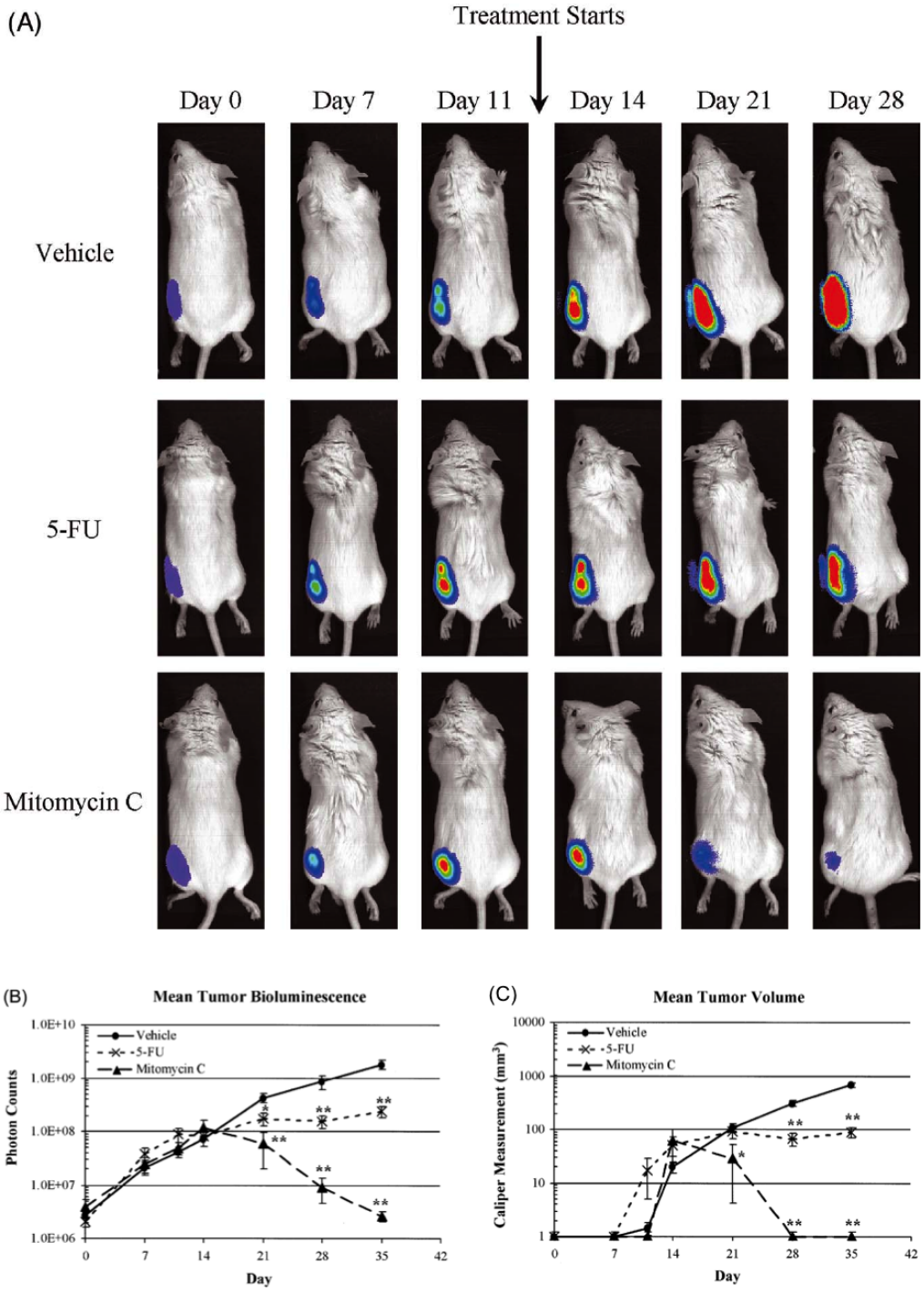

Figure 1.2: (A) Bioluminescence images of a subcutaneous tumour, labelled with luciferase, treated in three different ways: 'Vehicle' animals received no treatment; middle row treated with '5-FU' which inhibits tumour growth; bottom row treated with 'Mitomycin C' which causes tumour regression. (B) Mean bioluminescence intensity (photon counts) of tumour. (C) Mean tumour volume (mm^3) as measured using calipers. Reproduced from ref. [1].

bioluminescent signal in the untreated tumour increased over the course of 28 days, while that from the 5-FU tumour increased until treatment at day 11, after which it remained constant, and the signal from the Mitomycin C-treated tumour increased until treatment at day 11, before decreasing. The trends observed were as expected from knowledge of the treatment given in each case. The tumour volume measured using calipers (Fig. 1.2 C) follows a similar trend to the BLI measurements, but BLI was able to detect smaller tumours, or groups of cells, than were measurable by the calipers [1]. The study demonstrated how BLI can be used to monitor tumour growth and treatment efficacy in a murine model longitudinally using the same animal throughout the course of the experiment, thus decreasing the number of animals required for the study.

It is important to choose the bioluminescent reporter carefully. Tissue is strongly absorbing at wavelengths shorter than approximately 600 nm (Fig. 1.3 a) and so the bioluminescent signal will be highly attenuated at these wavelengths. It is therefore desirable for bioluminescent reporters to emit light at near-infrared (NIR) wavelengths where the attenuation is lower. Multiple luciferase reporters are available, all with different spectral emission characteristics [24,25], the emission spectra of a selection of luciferases are shown in Fig. 1.3 b. The peak emission wavelength of fluc is 612 nm [25], tissue attenuation is low for wavelengths above this peak emission wavelength (Fig. 1.3 a) and the signal is therefore subject to minimum attenuation and is able to propagate through the animal to the surface. However, longer wavelength reporters are desirable.

BLI is extremely useful in a range of pre-clinical studies. However, the quantitative accuracy of the technique is limited. The planar images obtained during BLI (such as those shown in Fig. 1.2) give very little information about the position or size of the bioluminescent source within the imaging subject, from these images it is impossible to determine any three-dimensional information about the source. It is possible that a weak, diffuse source near the surface of an animal could produce identical surface fluence to that from a stronger, more

compact source deeper within the animal (demonstrated in Fig. 1.4) [26]. Bioluminescence Tomography (BLT, Section 1.1.2) aims to address this. Further limitations to BLI include: dependence of the measured bioluminescence on the position of the animal [27, 28] and the underlying tissue attenuation [29, 30] (these limitations will be addressed and discussed in more detail in Chapter 3, and Chapters 5 and 6 respectively), and additionally depends on the level and type of anaesthesia [21,31], temperature [25,32] and substrate concentration [33] (Eq. 1.1).

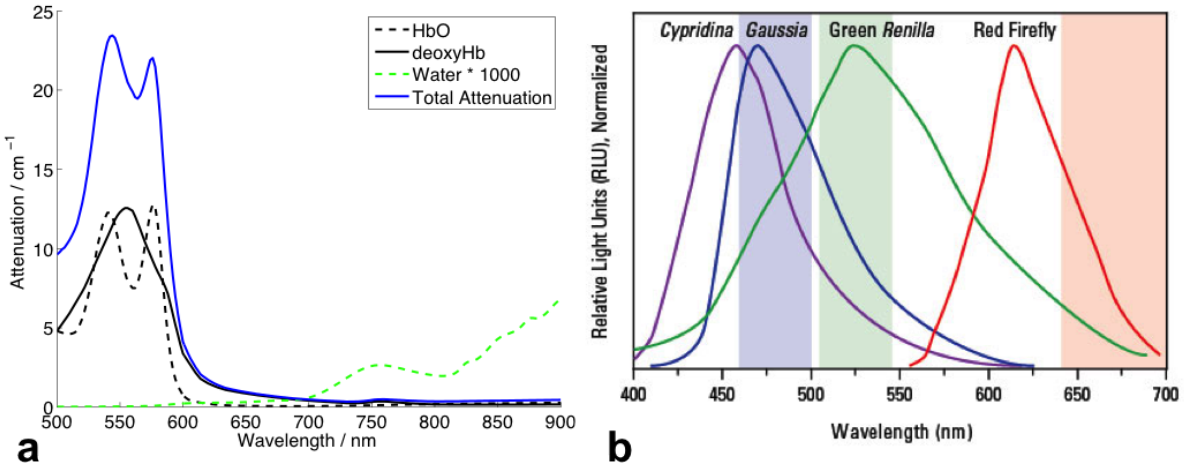

Figure 1.3: (a) Total attenuation of tissue, with contributions by oxy- and deoxy-haemoglobin (HbO and deoxyHb) and water, assuming equal concentrations of HbO and deoxyHb (1 mM). The water attenuation has been multiplied by a factor of 1000 due to the low contribution compared to HbO and deoxyHb. (b) Emission spectra of four different luciferases which are currently available for bioluminescence studies, reproduced from ref. [24].

1.1.2 Bioluminescence Tomography (BLT)

BLT is an extension to BLI which provides three-dimensional volumetric information about the bioluminescent source, i.e. providing more information about the size and shape of a tumour for example, than BLI. BLT uses multi-spectral BLI data to reconstruct the three dimensional position of the source within the animal, using reconstruction algorithms which

use models of light propagation through tissue to estimate the true three-dimensional source distribution (more detail on these algorithms in Chapter 2). Using multi-spectral BLI data rather than data encompassing the entire emission spectrum of the reporter has been shown to improve the quantitative accuracy of BLT by reducing the non-unique, ill-posed nature of the reconstruction [26, 34]. The non-unique nature of BLT is shown in Fig. 1.4, both sources (one deeper and more localised with a higher intensity, one superficial and diffuse with a low intensity) give rise to the same surface measurements (Fig. 1.4 c). Acquiring data at multiple wavelengths will enable these sources to be distinguished due to the differing attenuation experienced by different wavelengths of light (Fig. 1.3 a).

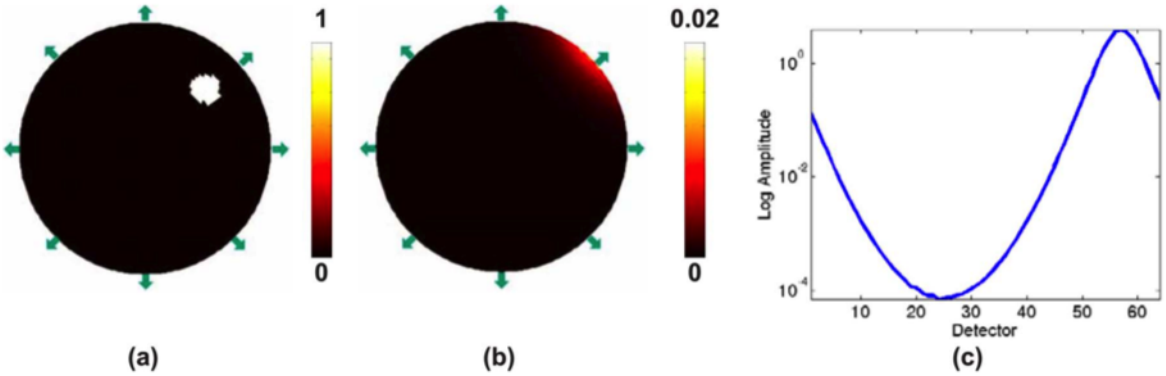

Figure 1.4: (a) and (b) show two different bioluminescent sources, with different intensities, as shown in the colourbars, which both give rise to identical surface measurements at the positions shown by the arrows. Surface measurements of both sources shown in (c). Reproduced from ref. [26].

Model-based tomographic reconstruction requires knowledge of the shape of the imaging subject (a three-dimensional model is required by the reconstruction algorithm), the internal tissue attenuation and a model of light propagation through the medium. In this work, NIRFAST, a numerical modelling software package which implements the diffusion approximation to the radiative transport equation via a finite element method (FEM) framework [35], is used for all modelling of light transport through tissue. The application of NIRFAST to this work will be described in Chapter 2.

However, truly quantitative BLT is a challenge. It is vital to have accurate knowledge of the optical properties of the imaging subject in order to perform quantitatively accurate BLT [36, 37]. When using BLT as a pre-clinical imaging technique the optical properties are highly heterogeneous due to the underlying anatomy of the animal being imaged, so using heterogeneous models of optical property distribution as opposed to homogeneous models is important [29,30,32,38]. However, in practice heterogeneous models are not always adopted. For example, a commonly used commercial optical imaging system, the IVIS Spectrum Pre Clinical *In Vivo* Imaging System (IVIS), assumes homogeneous models of tissue attenuation for use in BLT source recovery [39, 40]. Heterogeneous models can be derived from atlas data [41, 42] or from complementary imaging modalities such as DOT [37, 43–47] and there are multi-modal optical imaging systems which are able to perform both DOT and BLT measurements [43, 46–49]. Chapters 5 and 6 present data applying a spectral derivative (SD) DOT algorithm to data taken using a multi-modal optical imaging system, to obtain underlying tissue attenuation for use in BLT source recovery.

Additionally, current reconstruction algorithms do not account for the bandwidth of band pass filters used for multi-spectral data collection [26, 34, 35, 50–52]. Thus far the effect this has on the quantitative accuracy of the recovered bioluminescent source has not been assessed. Work to investigate this is presented in Chapter 4, and a model which accounts for the filter bandwidth in the BLT reconstruction is introduced and validated. Chapter 6 presents data demonstrating the efficacy of the SD DOT algorithm in a murine model, utilising the recovered optical property distribution in combined DOT-BLT, to validate both the SD algorithm and the filter bandwidth model in a murine setting.

1.1.3 Diffuse Optical Tomography (DOT)

DOT is an optical imaging technique which is used to produce tomographic maps of attenuation of an imaging subject: either absorption and reduced scatter coefficients, μ_a and μ_s', or

tissue chromophore concentrations. An array of light sources on the surface of the imaging subject are illuminated sequentially, and the light which passes through the imaging subject is detected at a number of locations across the surface. The sources can either be broad-band illumination, with the detected signal filtered with band pass filters to measure the transmitted NIR light at different wavelengths [48, 49], or discrete NIR wavelengths, using light emitting diodes (LEDs) [53–55] or lasers or laser diodes [45, 56, 57]. The use of multi-spectral data enables the attenuation to be determined at multiple wavelengths and enables the chromophore concentrations to be determined if necessary. When performing DOT on human or animal tissue the main chromophores present are oxyhaemoglobin (HbO), deoxyhaemoglobin (deoxyHb) and water, and these are the chromophores which are considered in this work (attenuation spectra shown in Fig. 1.3 a). Each tissue has different total attenuation due to the different combinations of chromophores present, e.g. due to varying tissue oxygenation causing variation of the ratio between HbO and deoxyHb.

In humans DOT has been shown to provide brain functionalisation maps comparable to those achievable with functional magnetic resonance imaging (fMRI) [54, 55, 58]. At the bedside DOT can be used to assess haemodynamics during seizures of neonates [56, 59], and functional connectivity in infants [53, 54, 60] and adults [61] through monitoring of tissue oxygenation and blood volume changes. DOT can also be used to assess traumatic brain injury [62] through identification of changes in blood concentration. The technique is also used to differentiate cancerous from normal tissue by the different haemodynamic response of the two tissue types, for example in breast cancer studies [63–67], and to identify arthritis in joints in the human hand [68–71] through changes in attenuation of the joint due to chronic inflammation.

As mentioned in Section 1.1.2 DOT can be used as a complementary imaging modality to BLT, providing prior knowledge of the tissue optical properties, increasing the quantitative accuracy of the BLT reconstruction [37, 43–47]. This is how DOT is used in this work.

1.1.4 Bioluminescence Imaging Systems

Over the past two decades bioluminescence imaging and tomography systems have developed substantially. Early imaging systems with BLT capabilities consisted of a CCD camera focused on a 360° rotating imaging platform which enabled images to be taken of the surface fluence from multiple different angles [72–74]. Broadband emission data was collected, filters were not used to obtain multi-spectral data. A disadvantage of these systems was the long data acquisition time required due to separate images being taken at each angle, and so the imaging throughput of these systems was low. Additionally, the emission of bioluminescent reporters such as fluc have a window over which the maximum emission intensity of the reporter occurs, for fluc this is ∼10-20 minutes [75], but varies depending on the animal model and bioluminescent reporter used [75, 76]. So due to the long acquisition time, use of these early imaging systems *in vivo* presented a challenge.

Meanwhile, it was shown that using multi-spectral BLI data for tomographic source reconstruction enhanced the quantitative accuracy of the recovered source [26, 34]. This led to developments to imaging systems to facilitate multi-spectral imaging, e.g. by including filter wheels [40, 77]. Developments were also made to the 360° rotation stage to simplify and streamline the multi-view imaging process by fixing the imaging platform and including mirrors which were positioned around the imaging subject to provide multiple views of the animal via the mirrors [49, 77–79].

As stated earlier, both BLT and DOT reconstructions require knowledge of the three-dimensional shape of the imaging subject. Further developments to imaging systems has been made to enable this to be determined using a complementary modality such as CT or MRI [30, 37, 38, 77, 80–82]. This can be either through incorporation of the system within the optical imaging system or production of an animal holder to keep the animal in the same position while it is moved between imaging systems. Structured light techniques have also been used for acquisition of imaging subject topography [49, 83, 84], these are simpler to

incorporate into existing optical systems and are more cost-effective and user friendly than techniques such as CT or MRI.

The importance of accurately determining the optical properties of the imaging subject for use in the BLT reconstruction was described in Section 1.1.2. Some systems adopt the method of acquiring CT or MRI data and applying literature optical property values to segmented tissue types [36, 77], others use integrated DOT systems to gain subject-specific optical properties [43, 47, 49, 85].

The optical imaging system used for the work presented in this thesis (BLDOT system, Fig. 1.5) is a multi-modal optical imaging system with BLT, DOT and three-dimensional surface capture (using structured light [83]) capabilities [48, 49]. The system is based on the simple BLT systems, with a fixed imaging platform and two right-angled mirrors which are freely positioned on either side of the imaging subject to provide multi-view data in a single CCD image. A filterwheel with six possible filter positions enables multi-spectral imaging and DOT illumination is provided via patterned light projection (patterns customisable by the user) using a projector, coupled via an optical fibre to a tungsten-halogen lamp [48, 49], similarly to the method adopted in a combined DOT-fluorescence tomography system [86,87].

The remainder of this section will provide an overview of a selection of commercially available bioluminescence imaging systems which are used in pre-clinical studies, and a comparison of these systems with the BLDOT system.

The capabilities of the imaging systems are summarised in Table 1.1. The IVIS Spectrum *In Vivo* Imaging System (IVIS) produced by Perkin Elmer is the most commonly used commercial imaging system in pre-clinical research. The system is used in cancer research [1,4,6–12], stem cell research [14,15] and work with immune cells [12,17], bacteria and viruses [19–22]. The IVIS Spectrum is predominantly used for planar BLI imaging, where BLI images are overlaid onto a bright image of the animal. Due to the customisable field of view (FOV) of the system it is possible to image up to 5 animals simultaneously [88],

Table 1.1: Comparison of five bioluminescence imaging systems and their capabilities.

System	Bioluminescence capabilities	Single or multi-view for data collection?	Homogeneous or heterogeneous optical property model for BLT?	Three-Dimensional Surface Capture	Available wavelengths for multi-spectral data collection	Field of view (FOV)	*In vivo* imaging?	Multi-modal imaging
Perkin Elmer: IVIS Spectrum	Planar BLI, BLT [88]	Single view	Homogeneous [89]	Yes, using a laser galvanometer [84].	Filter wheel with 24 positions, band pass filters in the range 490-850 nm (bandwidth 20 nm) [88].	Ranging from 3.9×3.9 cm to 23×23 cm [88].	Yes. There is a gas anaesthesia manifold and heated sample stage [88].	Yes. The system also has fluorescence imaging capabilities [90].
Bruker: In-Vivo Xtreme II	Planar BLI [91]	Single view	N/A	No	Filter wheel with 8 positions, band pass filters in the range 535-830 nm (bandwidth ~20 nm) [91, 92].	Ranging from 7.2×7.2 cm to 19×19 cm [91, 92].	Yes. There is a gas anaesthesia manifold and the imaging chamber is temperature regulated [91].	Yes. Fluorescence imaging, direct radioisotopic imaging, Cerenkov imaging, X-ray imaging [91, 92].
BioSpace: PhotonIMAGER™	Planar BLI. An upgrade to the standard system to include the '3D module' enables 3D rendering of BLI data [93].	Single view. Upgrade to include the '3D module' includes multi-view data collection [93].	N/A	No (requires upgrade to include '3D Module' [93]).	Filter wheel with 15 emission filters (band pass and high pass, bandwidth and wavelength unknown) [93].	Ranging from 8×6 cm to 22×16.5 cm. Addition of the 'Macrolens module' can reduce the FOV to 3.2×2.8 mm [93].	Yes. There is a gas anaesthesia manifold and temperature controlled imaging stage [93].	Yes. Fluorescence imaging and X-ray imaging on addition of an X-ray module [93].
LI-COR: Pearl® Trilogy	Planar BLI [94]	Single view	N/A	No	No multi-spectral data collection [94, 95]	11.2×8.4 cm [94, 95]	Yes. There is a gas anaesthesia manifold and heated imaging stage [94, 95].	Yes. The system also has fluorescence imaging capabilities [94, 95].
BLDOT	Planar BLI, surface mapped BLI (using Free Space modelling [27]) and BLT (including filter bandwidth modelling [96]).	Multi-view using freely positioned right-angled mirrors [48, 49].	BLT can use either model as defined by the user. Subject-specific, heterogeneous, optical properties are determined using DOT.	Yes, using a fringe projection profilometry system [83, 97]. Resulting mesh used for Free Space Modelling, BLT and DOT reconstruction.	Filter wheel with 6 positions. Band pass filters ranging from 500-850 nm with bandwidths of 10 nm, 600 - 643 nm with bandwidths ranging from 22-34 nm.	Approximately 10×10 cm but varies as the height of the imaging platform changes. Only capable of imaging one animal at a time.	No. System requires development to include heated stage and anaesthesia.	Yes. DOT-BLT. Uses a spectral derivative reconstruction algorithm.

enabling a high imaging throughput which is advantageous in pre-clinical studies. It is also possible to perform BLT [40, 89, 98]. A laser galvanometer is used to produce a point cloud of coordinates of the surface of the animal to create a three-dimensional model for use in BLT reconstruction [84]. For animal imaging the optical properties used by the "DLIT 3D source reconstruction" (DLIT: Diffuse Luminescence Imaging Tomography) are defined as 'tissue' (exact properties unknown) and are assumed to be homogeneous [39, 89] which will introduce errors when performing animal BLT [52], where using heterogeneous optical properties for tomographic source recovery has been shown to improve the quantitative accuracy of BLT [29, 30, 32, 38]. Although the system is capable of multi-spectral imaging, during BLI data collection an open filter is used, collecting data across the entire emission spectrum of the bioluminescent source [1, 4, 21, 99].

The In-Vivo Xtreme II by Bruker is less commonly used than the IVIS, with only a small number of examples of use of the system in cancer research [100–102]. Additionally, it is only possible to perform planar BLI which limits the applicability and quantitative accuracy of the system. However, the additional capabilities of fluorescence, radioisotopic, cerenkov and X-ray imaging enable complementary information to be obtained during an experiment, but this complicates the work. The X-ray imaging system enables some anatomical context to be gained, with BLI data overlaid on to the X-ray image where possible [91]. Like the IVIS Spectrum the customisable FOV enables up to 5 animals to be imaged simultaneously [91, 92, 103] which is advantageous for throughput.

BioSpace produce the PhotonIMAGER^{TM}. The standard system is able to perform multi-spectral imaging, however the wavelength and bandwidth of the filters present is unknown, but in published studies in cancer research [31, 33, 104, 105] and stem cell studies [106, 107], broadband data collection is performed. As with the IVIS Spectrum and In-Vivo Xtreme II the FOV is customisable, enabling up to 10 animals to be imaged simultaneously [93]. The standard system is customisable and multiple 'modules' are available to add to the system

to extend the range of capabilities [93]. The ability to include the 'X-ray Module' enables anatomical context to the BLI data to be provided, and a '3D Module' enables multi-view data collection and surface rendering of BLI data to be performed [93]. However it is unclear whether this module enables full tomography or just three-dimensional surface rendering of data.

The final commercial system included here is the Pearl® Trilogy by LI-COR [94,95]. This system has only recently been developed from a purely fluorescence imaging system so is still in its infancy for use in bioluminescence imaging, and no publications using the system for BLI have been sourced. The system is less customisable than the systems presented above and is only capable of imaging a single animal at a time, with no multi-spectral data collection capabilities - broadband BLI data is collected across the range 450-640 nm [94, 95].

The BLDOT system (Fig. 1.5) takes inspiration from all of the above commercial systems and their capabilities. Previous work on the BLDOT system, detailing the development of the system and the capabilities in BLI, BLT, DOT and combined DOT-BLT applied to phantom data, can be found in references [27, 48, 49, 83, 97]. The free space modelling that produces surface mapped BLI images, accounts for inaccuracies in BLI measurements introduced by changes in the position of the animal (i.e. corrects BLI data) [27,28], which aren't accounted for by the commercial systems above. The modelling not only produces surface mapped (corrected) BLI but also provides accurate surface measurements to use in BLT. The first use of this model on murine data is presented in Chapter 3.

By using freely positioned mirrors to provide multi-view data, more information about the bioluminescent signal can be provided [48, 49], which is vital when performing BLT. Additionally, the mirrors enable the surface capture system to gain topographic information from a larger surface area of the imaging subject [83]. The surface capture system was custom-developed for the BLDOT imaging system, and has been shown to be accurate within 0.4 mm and have the ability to resolve features of the order of hundreds of μm [83, 97]. The

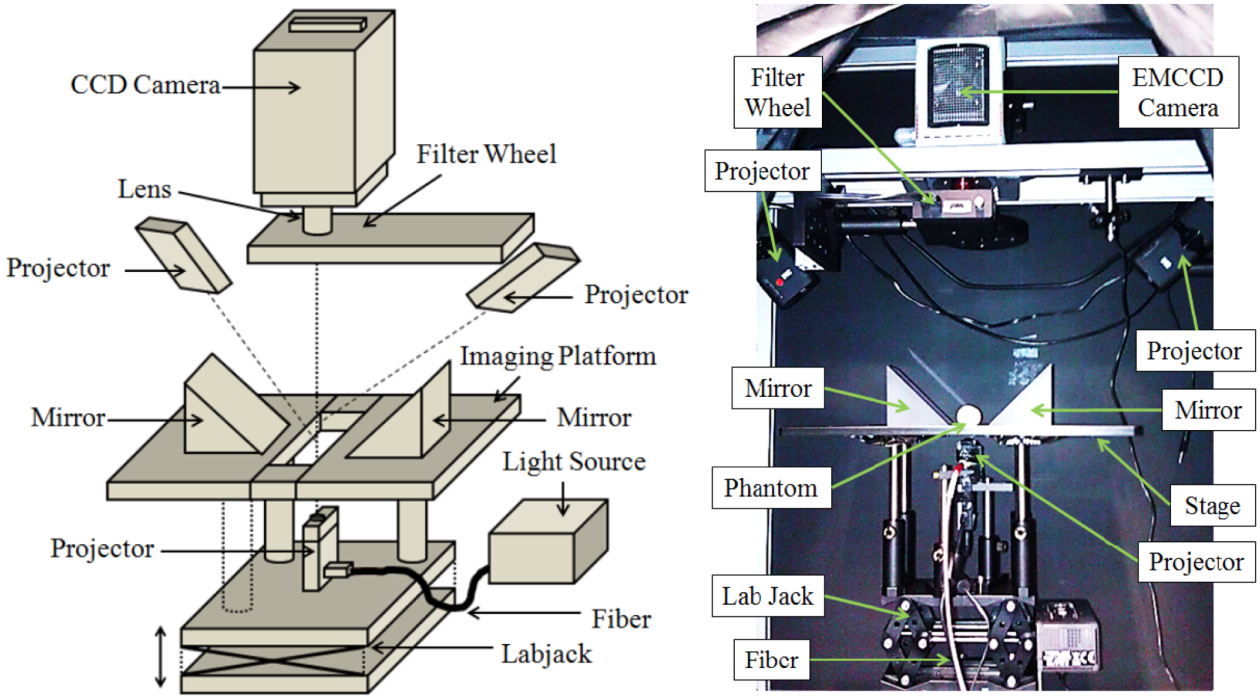

Figure 1.5: Schematic (left) and photograph (right) of the BLDOT imaging system. The two upper projectors facilitate surface capture, the lower projector diffuse imaging and the filter wheel enables multi-spectral imaging. The two right-angled mirrors on the imaging platform expand the field of view of the system. Reproduced from ref. [49].

surface capture system is used to produce three dimensional models of the imaging subject for use in free space modelling, BLT and DOT.

The optical properties used for BLT source recovery are typically defined by the user. It is possible to use homogeneous properties, heterogeneous properties from atlas models (this requires registration of an atlas model to the subject-specific surface topography data) and subject-specific heterogeneous properties from DOT imaging. This customisation of optical properties cannot be done using the commercial systems above. Use of DOT-determined optical properties as prior knowledge for the BLT reconstruction, DOT-BLT, is presented in ref.'s [48, 49] for phantom data, and in Chapter 6 applied to murine data using a SD DOT reconstruction method.

The filterwheel, which enables multi-spectral data collection, has only 6 filter positions.

However, these can be changed enabling imaging wavelengths to be customised depending on the particular application. Available filters range from 500 to 850 nm with bandwidths ranging from 10 to 34 nm, but additional filters can be purchased to suit the application. The work presented in Chapter 4 demonstrates that wider bandwidth filters can be used for multi-spectral data collection for BLT, provided the bandwidth of the filters are accounted for in the reconstruction using the filter bandwidth modelling method [96] which is also introduced in Chapter 4. This filter bandwidth modelling is not applied by the IVIS Spectrum, during BLT source recovery.

The additional capabilities of the BLDOT system compared to the commercial systems, i.e. free space modelling, filter bandwidth modelling and DOT (including SD DOT), are advantageous in enhancing the quantitative accuracy of BLI and BLT achievable with the system.

The following sections provide an overview of pre-clinical imaging modalities, including comparison to BLI and BLT.

1.2 Common Pre-Clinical Imaging Modalities

Additionally to BLI and BLT a wide range of different imaging modalities are used in pre-clinical studies, ranging from MRI and CT to positron emission tomography (PET) and optical techniques. This section will give an overview of imaging techniques which are used in pre-clinical research.

1.2.1 Fluorescence Imaging and Tomography (FLI and FLT)

Fluorescence imaging (FLI) is a functional technique with many similarities to BLI. A cell or antibody of interest within an animal is labelled with a fluorescent molecule which is excited by an external light source, usually a laser, and the subsequent fluorescence emission

is captured by a CCD [108–110]. As with BLI only the light which reaches the surface of the animal can be detected, meaning that reconstruction algorithms are required to extend FLI into FLT. FLI is used in cancer research to image tumours [111,112], adhesion molecules [113], in evaluation of therapies [114] and has been used to image plaque present in the brain associated with Alzheimer's disease [115] and vascular plaque present in atherosclerosis [116]. It is also possible to perform dual-marker imaging to study binding kinetics [117, 118].

FLI is a well-establised imaging technique and a large number of fluorophores have been developed for use in a wide range of applications. Fluorophores can be synthesised to selectively target particular cell surface receptors or antibodies and can be developed for the requirements of a particular experiment. Due to particular cell surface receptors or antibodies being labelled, the number and location of the specific molecules are tracked in FLI. In contrast, the whole cell is labelled in BLI, enabling only the location and proliferation of entire cells to be monitored. Thus, currently FLI is more versatile than BLI but both techniques have their own advantages and disadvantages, and can be applied to slightly different applications.

Quantitative FLI is limited by the diffuse propagation of light through tissue, as with BLI. However, with FLI both excitation and emission light propagate diffusely through tissue, adding additional complications in the imaging and FLT reconstruction process when compared to BLI, where only emission light is subject to tissue attenuation (as no excitation light source is required). FLT, like BLT, requires a model of the propagation of light through tissue in order to reconstruct the internal light source [109]. In FLT the emission can be normalised based on the excitation by calculating the Born ratio: $U_B = \frac{U_{fl}}{U_{ex}}$; where U_{fl} and U_{ex} are measurements at fluorescence and excitation wavelengths respectively [109]. This makes the assumption that the excitation and emission light have the same tissue interactions, which is not the case due to spectral attenuation of tissue (see Fig. 1.3 a) but when the tissue optical properties are unknown has been shown to be an effective simplification to

make in the FLT reconstruction [109, 111, 119].

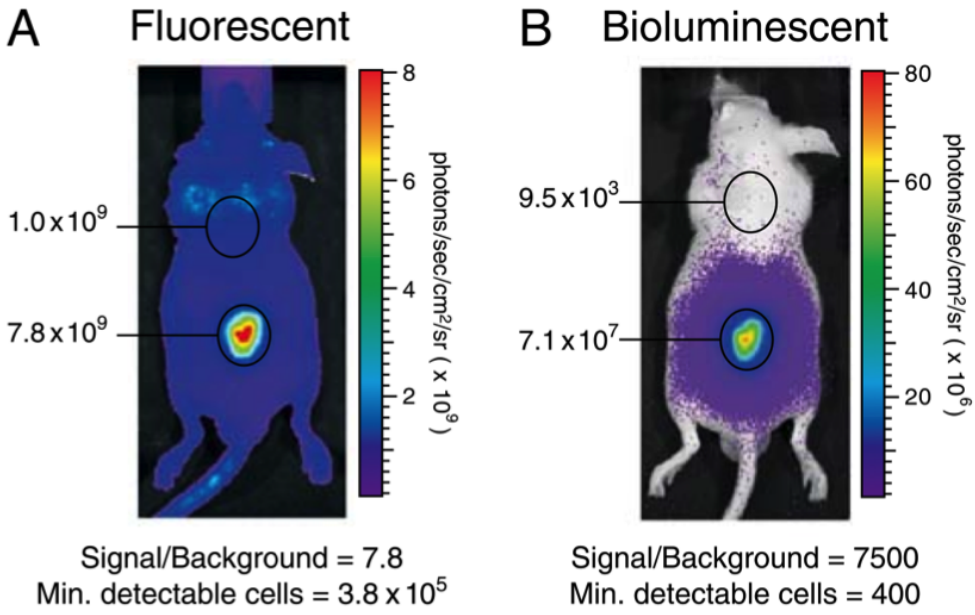

Figure 1.6: *In vivo* (A) Fluorescence and (B) bioluminescence images of cells dual labelled with a fluorophore and a bioluminescent reporter (DsRed/PC-3M-luc) subcutaneously injected into a nude mouse. The enhanced SNR for BLI images can be seen. Reproduced from ref. [112].

In addition to the diffuse optical signal there are other similarities between BLI and FLI: a complementary imaging modality is required in order to provide anatomical information [108, 111, 119, 120]; the wavelength of the emission and, additionally in FLI, the excitation light must be long, ideally into the red and near-infrared, to maximise excitation of the fluorophore and maximise the emission which reaches the surface of the imaging subject, due to tissue attenuation being low at these wavelengths (Fig. 1.3 a) [111, 119]. Although there are many similarities between FLI and BLI, an advantage of BLI over FLI is the absence of excitation light which can contaminate the fluorescence measurements. The excitation light present during FLI data collection can be reduced by using optical filters, fluorophores with large Stokes' shifts and calculating the Born ratio of data, but will still affect the measured fluorescent signal.

A further advantage to BLI is the high signal-to-noise ratio (SNR): all signal detected during BLI is due to bioluminescence, there is no autoluminescence of tissue, analogous to the autofluorescence present during FLI [119]. Fig. 1.6 demonstrates the enhanced SNR of BLI images compared to FLI images. The animal in the images shown was injected subcutaneously with human prostate cancer cells which had been labelled with firefly luciferase (PC-3M-luc) and DsRed, a fluorescent protein, both of which had comparable peak emission wavelengths [112]. As shown in the figure, although the maximum fluorescent signal measured was $\sim\times 10^2$ larger than the bioluminescent signal, the signal to background ratio was substantially larger for the BLI images [112]. However, with FLI it is possible to selectively excite regions of interest, decreasing the contribution of autofluorescence from tissue at a distance from the fluorophore localisation, and fluorescence emission from fluorophores located in tissue far from the region of interest. This is not possible with bioluminescence, where all bioluminescently labelled cells emit light following administration of the substrate to the animal.

1.2.2 Magnetic Resonance Imaging (MRI)

MRI is a non-invasive technique based on nuclear magnetic resonance, able to provide anatomical information about an imaging subject through application of a number of magnetic fields and radiofrequency (RF) pulses. The subject is placed in the bore of an electromagnet, which produces a strong magnetic field ($>$0.5T for clinical scanners [121]). An odd number of protons and/or neutrons within nuclei will give rise to a net spin and magnetic moment which aligns with the magnetic field. Protons (^{1}H atoms), which are present in high abundance in living tissue, for example in water, proteins and lipids, have an inherent magnetic moment and therefore are ideal nuclei to image in MRI. Application of an RF pulse changes the alignment of the proton magnetic moment. When the RF signal is removed the protons relax back to align with the magnetic field, emitting an RF signal as they do so which

is detected by a receiver coil. The rate at which the protons relax is the 'relaxation time' and this depends on the environment of the protons, including: the surrounding atoms; the size of the molecule the protons are associated with and the atoms which the protons are bound to within the molecule. So the relaxation time and therefore the RF pulse that is received as the protons relax is dependent on tissue type and gives rise to the contrast observed within the high resolution images of the internal anatomy of a patient or animal [121].

The image contrast can be altered through the use of different pulse sequence designs in order to highlight specific features, based on the different relaxation properties of various tissue types. This versatility enables MRI to image a wide range of different anatomical features and is customisable by the user, dependent on the desired anatomical information. For example, tissues with high water or fat content can be highlighted using different pulse sequences [121]. The versatility of MRI is demonstrated by its use in a wide range of pre-clinical studies, including: monitoring tumour growth and response to treatment [122]; angiogenesis [123]; cell tracking [124, 125]; and neurological activation and diseases [126, 127].

In pre-clinical research into cancerous tumour growth BLI is able to detect a smaller number of cells than MRI, for example it is possible to detect a cluster of cancer cells with BLI before a tumour is visible using MRI [128]. Due to the process through which bioluminescence emission occurs, only metabolically active cells emit bioluminescent light, so BLI is able to provide information about the portion of a tumour occupied by metabolically active cells, i.e. cells which are actively proliferating, through monitoring of surface intensity data, whereas MRI will provide structural information about the size of the whole tumour including necrosed cells. However, the high resolution structural information which can be gained from MRI is advantageous and, when used in conjunction with BLI, provides anatomical context for the bioluminescent signal. Moreover, the techniques used in MRI can be translated into human imaging, which is not possible during BLI due to the signal penetration depth limitations of the bioluminescent signal posed by tissue attenuation.

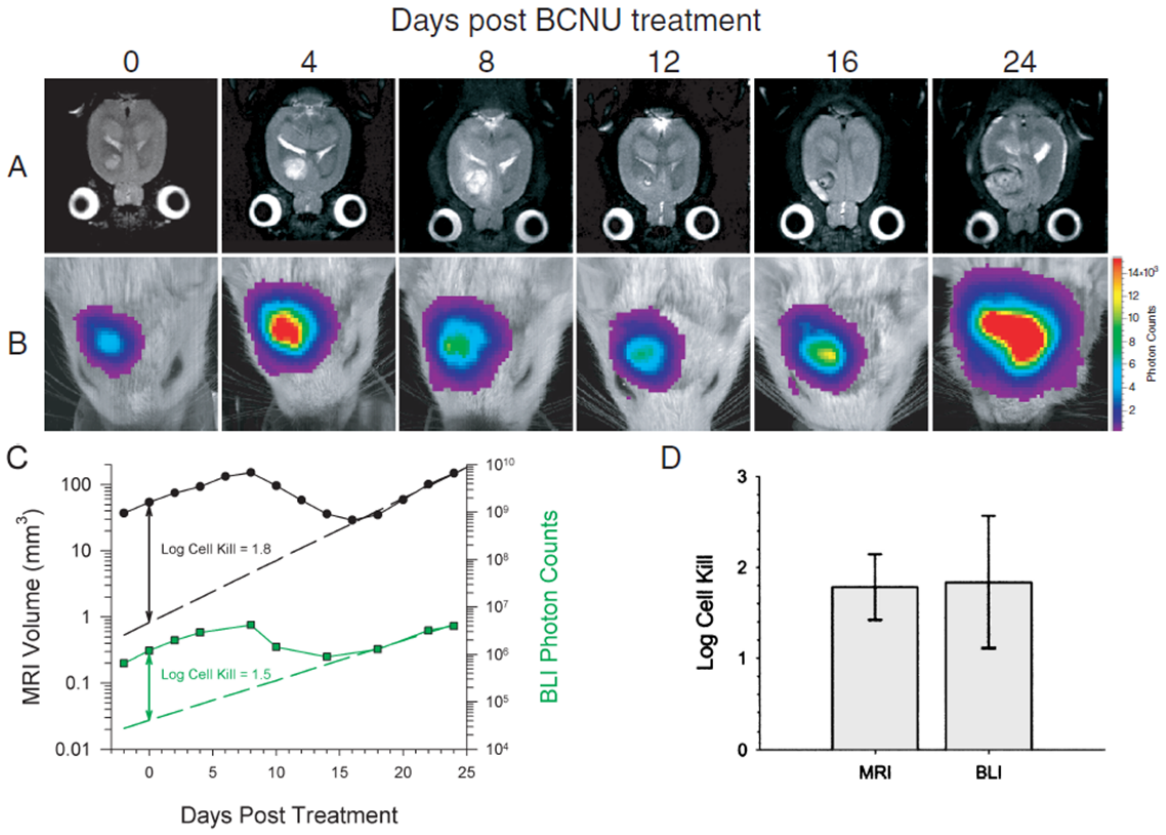

Figure 1.7: (A) MRI and (B) BLI images of a rat brain tumour from 0-24 days after treatment with a chemotherapeutic agent. (C) Tumour volume (MRI, mm^3) and photon counts (BLI) as a function of number of days after treatment. (D) Cell kill values quantified from MRI volume and BLI photon count plots. There is a strong agreement between the two modalities. Reproduced from [128].

Due to the functional information about the tumour which can be obtained using BLI, it would be beneficial to develop BLT further to enable quantitative three-dimensional information to be obtained *in vivo*. The spatial resolution achievable by BLT is limited by the diffuse propagation of light through tissue, so it is possible to use MRI and BLT/DOT as complementary techniques, using the structural information achievable from MRI imaging as prior knowledge for the BLT or DOT reconstruction [80, 129] or drawing comparisons between the size of a tumour on MRI images and the bioluminescence emission intensity [128, 130]. The equipment required for BLI is cheaper and more compact than MRI, and is often simpler to

use without the requirement for specialist training. Imaging is much faster (of the order of minutes for BLI but can range from tens of minutes to over an hour for MRI depending on the size of the imaged volume) and multiple animals may be imaged simultaneously in some commercial imaging systems, such as the IVIS [131], enabling a high imaging throughput which is advantageous in pre-clinical studies.

A study in 2000 by Rehemtulla *et al.* compared BLI and MRI during monitoring of the growth of a rat brain tumour and response to a chemotherapeutic agent [128] (MRI and BLI images are shown in Fig. 1.7 A and B respectively). A correlation of 91% between the volume (mm^3) of the tumour measured from MRI data (Fig. 1.7 C black line) and the bioluminescence emission intensity (photon counts, Fig. 1.7 C green line) over the course of the experiment was observed. Both modalities show increasing tumour volume until the treatment takes effect around day 8, decreasing as cells are killed, and increasing again as remaining cells begin to proliferate. There was also a strong agreement between cell kill values (Fig. 1.7 D) [128]. This agreement between the two modalities has been found by other groups [132] and demonstrates how the two techniques can be used in a complementary fashion.

1.2.3 X-Ray Computed Tomography (CT)

CT, like MRI, provides anatomical information about an imaging subject. The imaging subject is moved through the CT gantry, which is a circular bore with an X-ray tube and detector array mounted on opposite sides. The X-ray tube and detector rotate around the gantry, and therefore the imaging subject, the detector measuring transmitted X-rays. Multiple projections are recorded during one complete 360° rotation of the X-ray tube and detector. As the imaging subject is moved through the gantry, transmission data is recorded from different longitudinal locations throughout the subject. Images of the internal attenuation can then be reconstructed from the recorded transmission data, which will build up a tomographic

image of the inside of the imaging subject [133,134]. The intensity of the image is dependent on the attenuation of X-rays by tissue, for example bone is highly attenuating and appears white on images, air has a low attenuation and appears black in images [133, 134]. Due to the high attenuation of bone compared to soft tissue, CT lends itself to imaging bones and is widely used in arthritis studies [133, 134]. Contrast agents extend the capabilities of CT to soft tissue imaging, for example intravenous agents enable imaging of the circulatory system, oral fluid agents produce contrast within the gastrointestinal tract and gaseous agents can be used to provide information about the colon [133, 135].

Pre-clinically, microCT is used, due to the size difference between small animals and humans and the higher resolution required to image these small animals [135]. The technique is used in a variety of applications, including: cancer research [135, 136]; vascular imaging [137–141]; lung disease [142, 143]; and investigating bone diseases [138, 144, 145]. In cancer research, structural infomation about tumours is achievable both with and without contrast. For example contrast is not required in the lungs where the contrast in CT intensity between air and soft tissue is such that the tumour can be directly visualised [135]. However, due to the similarity in intensity between different soft tissue types, contrast agents are required to visualise soft tissue tumours.

Due to the ability of CT to provide anatomical information, it is often used in conjunction with a functional imaging technique, such as PET [146, 147], BLT [46, 47] and FLT, [108, 111, 115], which are unable to produce structural images such as those achievable with CT, making CT a valuable complementary technique which can provide anatomical context to the data achievable with the functional techniques. This multi-modality imaging involves either post-imaging registration of images from the two modalities or the use of a dual-modality imaging system [108,111]. There are also multi-modality imaging systems available which combine nuclear, CT and optical imaging [81, 148]. CT data can also be used as prior structural knowledge for BLT reconstructions [30, 38, 80, 81, 148], similarly to MRI.

Like with MRI and nuclear techniques (discussed in the following section), pre-clinical CT imaging and multi-modal CT-nuclear imaging can be translated into human imaging as the signal is only mildly attenuated by tissue. This is advantageous as, when a pre-clinical study is ready to be translated to humans, the imaging methodology can be kept constant. As mentioned in previous sections, imaging in humans is not possible using optical techniques. Disadvantages of CT in comparison to BLI and BLT are the use of ionising radiation, which is not required to image bioluminescent signal, and the complex and expensive equipment required, which requires specialist training for use. CT has been used to produce a mouse atlas: Digimouse [42], which has been used in fluorescence [149] and bioluminescence [96] studies and is used in simulation work presented in Chapter's 4 and 5.

1.2.4 Positron Emission Tomography (PET) and Single Photon Emission Computed Tomography (SPECT)

PET and SPECT are functional techniques which involve labelling cells of interest with a radionuclide tracer, and are able to produce three dimensional tomographic images of the tracer distribution *in vivo*. In PET, each tracer molecule emits a positron as it undergoes β^+ decay. The positrons annihilate with electrons in the surrounding tissue producing two gamma rays of energy 511 keV for each annihilation event. SPECT tracers directly emit one gamma ray per molecule during electron capture decay, these photons are of a lower energy than those emitted in PET [150, 151]. The emitted photons are detected by scintillation detectors which are placed around the patient, this projection data can then be reconstructed into a tomographic image of tracer distribution [150–152].

Due to the method of photon production, the reconstruction process differs for PET and SPECT. In PET, the two photons which result from electron-positron annihilation events are emitted at approximately 180^o from each other. Therefore by using detectors on either side of the imaging subject the position of the radiotracer can be estimated by drawing a line

between the positions of photons detected within a small time window on each detector [150]. In SPECT only a single photon is emitted so the directional information achievable in PET is not possible. In order to gain directional information, collimators can be placed in front of the detector to enable detection of photons from a small range of angles, however this decreases the sensitivity of SPECT in comparison to PET [150, 151, 153].

These nuclear imaging techniques are used in stem cell tracking studies [154–156], cancer studies [152, 157, 158], to monitor perfusion [153], image plaques associated with Alzheimer's disease [159, 160] and in pharmacokinetic studies [161]. An advantage of nuclear imaging over BLI and BLT is the ability to directly translate pre-clinical animal studies into human imaging, which is not possible using BLI due to the signal penetration depth limitations of the bioluminescent signal as explained earlier. Also, the high energy photons emitted during nuclear imaging are not subject to tissue attenuation, particularly scatter, to the same degree as bioluminescent photons and therefore the tomographic reconstruction problem doesn't require modelling of diffuse propagation of light through tissue. However the photons are still affected by tissue attenuation and therefore model-based reconstruction algorithms are required [162–164], and there remains some uncertainty about the exact location of the tracer within the imaging subject, as with BLI. There is also a concern that radionuclide tracers affect the viability, function and differentiation of cells [124], and during cancer studies it is possible that the radiation may provide some anticancer therapy or produce further cancerous cells [150].

Like BLI and BLT, nuclear imaging techniques provide functional information and have uncertainty associated with the recovered tomographic source location, so in order to pinpoint anatomically where the tracer is located, complementary structural imaging techniques must be used. Commercial dual modality CT/PET and MRI/PET systems are available [146,165], however the incorporation of an extra imaging system introduces significant spatial and monetary costs and additional specialist training is required for use. Dual modality optical-

PET/SPECT systems have been reported [82, 166] which can be used to compare the data produced using both modalities. Probes have been developed which are dual radionuclide and optical probes [148, 166, 167] so that the signals detected using both modalities are from the same position within the animal. As the resolution of nuclear techniques is higher than that of optical techniques it would be possible to use the reconstructed nuclear source as prior information for the BLT reconstruction, enabling a more accurate bioluminescent source reconstruction.

1.2.5 Ultrasound Imaging (US)

Ultrasound imaging is a structural imaging technique based on the reflection of acoustic waves from a change in density such as the boundary between two tissue types. Traditionally used in the imaging of foetuses in the womb, this technique is also used in pre-clinical research. In cancer research [168–172] the technique can be used to monitor tumour growth, and is able to produce tumour measurements comparable to histologically measured volumes [170, 171]. US has also been used in studies which investigate vasculature, blood flow or drug delivery [168, 173, 174]. Some studies make use of microbubble contrast agents which enhance contrast by increasing the intensity of the backscattered ultrasound signal [168, 171–175].

A major advantage of US is that it is a real-time imaging technique. It is relatively inexpensive, although some training is required both to use the instrument and to interpret the images. Some functional information can be obtained, for example doppler-US is able to provide information about blood flow [168, 171, 173]. US could be used in conjunction with optical imaging to determine the origin of a bioluminescent signal, rather than using CT or MRI which are significantly more expensive and much slower. For this purpose it would be possile to incorporate the US probe into the optical system.

A drawback to the technique is the low spatial resolution when compared to CT and MRI but the low cost, ability to do real-time imaging quickly and high throughput makes US an

attractive structural imaging technique for use in pre-clinical studies.

1.2.6 Photoacoustic Tomography (PAT)

Photoacoustic tomography is a rapidly developing technique which is able to image biological features of a range of sizes from organelles to organs [176, 177]. Molecules in the sample of interest absorb an optical excitation, a nanosecond laser pulse, the wavelength of which is chosen depending on the optical absorption of the molecules of interest. Through the photoacoustic effect, absorption of the laser light causes a localised thermal expansion which in turn induces a mechanical wave which propagates through the sample [176, 178]. This mechanical wave is detected in the same way as in US imaging, with a piezoelectric transducer, and the signal processed using reconstruction algorithms to reconstruct an image of the absorbed energy density [176, 179]. The large size range of features which can be resolved using PAT is accessed by modifying the focus of the excitation light and detection geometry [176].

Due to the spectral absorption of light by chromophores, multispectral imaging can be performed, making it possible to calculate chromophore concentrations and, in an *in vivo* setting, tissue oxygen saturation throughout the field of view [176, 178, 180]. As the contrast in this modality is based on the absorption of excitation light [176, 178], and in tissue, the strongest absorption of light at optical and near-infrared wavelengths is haemoglobin (Fig. 1.3 a), PAT lends itself to imaging vasculature *in vivo*. As such there have been studies using PAT to image tumour vasculature and response to therapy [176, 179, 181, 182]. By tuning the wavelength of the laser excitation, a range of chromophores other than haemoglobin can be imaged: DNA/RNA, melanin, water and lipid for example [176, 183]. It is also possible to make use of contrast agents such as nanoparticles, organic dyes and reporter genes, which can be functionalised to target a cell type of interest [176]. Examples of a range of applications

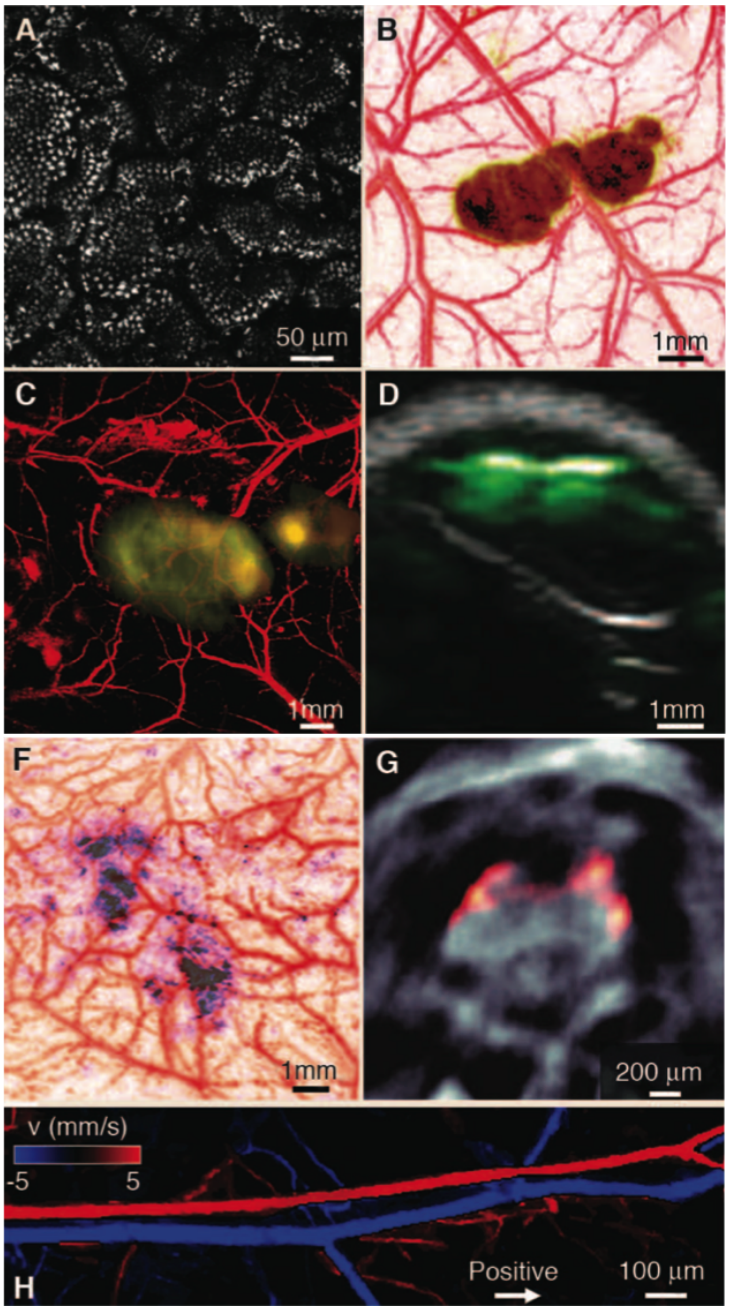

Figure 1.8: Examples of the application of PAT in biological imaging. A Nuclei of *ex vivo* murine intestinal villi epithelial cells, contrast achieved by exciting DNA/RNA. B *in vivo* murine melanoma (cells injected subcutaneously) and surrounding vasculature. C As B but with additional gold nanocage contrast. D Overlay of US (grey) and photoacoustic (green) images of an *in vivo* murine tumour with carbon nanotube contrast. F *In vivo* gliosarcoma and surrounding vasculature in a rat brain. G Brain of a transgenic zebrafish expressing the fluorophore mCherry. H Images of blood flow (including velocity) in the *in vivo* murine ear. Reproduced from ref. [176].

and size scales of PAT are shown in Fig. 1.8. The technique has also been shown to be effective in imaging functional connectivity in the brain [184] and has been extended to acquire temporal information [185].

The technique has advantages over optical imaging in that ultrasound waves are less scattered in tissue than light at typical bioluminescent wavelengths, so PAT images are of a higher resolution than optical images (demonstrated by the ability of the technique to image subcellular structures). However, the pulsed laser required for excitation significantly increases the cost of PAT systems above that of BLI systems, but the versatility of PAT is clear from the breadth of imaging size scales and applications that are achievable.

1.3 Conclusions

This chapter outlines the wide range of pre-clinical imaging techniques which are available, each with their own advantages and disadvantages. CT and MRI are able to provide high-resolution structural information about an imaging subject, but functional information is either not possible (CT) or extremely complicated (MRI). These techniques could be complementary to optical and nuclear techniques which rely on complicated reconstruction algorithms to reconstruct the internal distribution of the source (in bioluminescence, fluorescence and nuclear techniques) or tissue chromophores (in DOT). The reconstruction problem can be simplified by providing structural information from CT or MRI for example. However, this increases both the cost and time required to collect all necessary data, and the structural and functional images from the multiple modalities must be accurately registered together. To decrease the imaging time it would be possible to use US to obtain the structural information for the optical reconstruction but this technique is unable to produce structural images of a resolution comparable to MRI and CT, and would require incorporation of an US probe to the existing imaging system. PAT is an extremely versatile imaging technique, which requires

a subset of differing imaging set-ups depending on the application. Although the technique is still emerging, the range of size scales which can be imaged with the technique make PAT an attractive imaging technique for use in a range of pre-clinical studies.

Bioluminescence imaging and tomography are the focus of this work. The technique requires relatively simple, user friendly equipment without the need for any ionising radiation (nuclear imaging, CT) or excitation light source (FLI). This work focuses on use and modification of hardware and software applied to the BLDOT system, but can be applied to other systems with an aim to enhance the quantitative accuracy of BLT in all non-contact optical imaging systems.

1.4 Thesis Outline

The work presented in this thesis aims to tackle a number of limitations to the quantitative accuracy of BLI and BLT with a view to advancing BLT towards routine use in pre-clinical studies. Firstly, the dependence of BLI measurements on the position of the imaging subject is addressed. Then possible limitations to the quantitative accuracy of BLT introduced by not including filter bandwidth modelling in the reconstruction algorithm are investigated. Finally the necessity of accurate knowledge of underlying attenuation of the imaging subject is addressed by using DOT as prior knowledge for BLT.

Chapter 2 introduces the theory and models used during BLI, BLT and DOT analysis in later chapters. Included in the chapter is a description of the propagation of light through diffuse media (i.e. tissue), with a particular focus on the forward model, which models the propagation of light from a light source within an imaging subject to the surface. Next, the free space model, which models the propagation of light through the free space between the surface of the imaging subject and the CCD, and back to the surface, is outlined. Finally, recovery of the internal source distribution (BLT) or the internal attenuation (DOT) from

free space-mapped surface measurements, using the inverse model, is described.

Chapter 3 applies the Free Space Model to *post mortem* murine BLI data for the first time, accounting for the dependence of measured data on the position of the animal. Thus far the model has only been applied to phantom data, but the results presented here show the model to be promising for future application *in vivo*.

Chapter 4 describes the addition of a novel filter bandwidth model to the BLT reconstruction algorithm. Currently the bandwidth of filters used in multi-spectral data collection for BLT is not accounted for. The effect of ignoring these bandwidths is investigated and the importance of including filter bandwidth modelling is highlighted through simulation and phantom studies. These studies are done using multi-spectral data at only three measurement wavelengths rather than the conventional five (or six) wavelengths which are used in the BLDOT system. Further data presented in this chapter assesses the effect of using fewer wavelengths for data collection on the quantitative accuracy of the recovered bioluminescent source.

Chapters 5 and 6 describe the application of a spectral derivative DOT reconstruction method to non-contact data for the first time. The DOT-determined, subject-specific, optical properties are then used as prior knowledge for BLT reconstructions, in combined DOT-BLT. This work aims to tackle the limitation to the quantitative accuracy of BLT posed by the difficulty in acquiring accurate knowledge of underlying tissue attenuation. The SD DOT method is first validated via simulation using a heterogeneous mouse model in Chapter 5, and then applied to a *post mortem* murine model using data acquired using the BLDOT system in Chapter 6. Modifications to the BLDOT system in preparation for this data collection are described and characterisation of the system is also presented.

Chapter 7 provides a summary of the work presented in this thesis, with ideas for future work required to develop BLT further.

Chapter 2

Theory

Optical tomographic imaging relies on accurate mathematical models of light propagation through tissue. These models enable surface measurements to be predicted based on a known light source distribution, or estimates of internal source distribution (BLT) or internal optical property distribution (DOT) to be calculated, based on surface measurements which are acquired using imaging systems such as the BLDOT system.

There are multiple steps involved in BLT and DOT data processing. Using the BLDOT system as an example, the light (either from an internal bioluminescent source or transillumination diffuse light source) propagates through the imaging subject to the surface. This process is described by the Forward Model (Section 2.2). The light then travels from the surface of the imaging subject to the CCD, where measurements are made. In order to perform tomographic reconstruction, the CCD data is mapped back on to the surface of the imaging subject to gain measurements of the distribution of light at the surface. The passage of light through the free space between the surface of the imaging subject and the CCD is described by the Free Space Model (Section 2.3). The surface data is then used in tomographic reconstruction for either bioluminescent source distribution in BLT, or optical property distribution in DOT, which requires knowledge of the propagation of light through

the imaging subject back to the source. This process is described by the Inverse Model (Section 2.4).

This chapter will describe the mathematical models implemented in this work, starting with an introduction to the propagation of light through tissue, diffuse optics.

2.1 Introduction to Diffuse Optics in Tissue

The passage of light through tissue is governed by absorption and scattering. Absorption is determined by chromophores present in tissue, the main ones at visible and near-infrared wavelengths (relevant to BLT and DOT) being oxy- and deoxy-haemoglobin (HbO and deoxyHb respectively) and water [3]. The absorption spectra of these chromophores is shown in Fig. 1.3 a. During an absorption event, an incident photon is absorbed by a molecule, causing an electron to be excited to a higher energy level. This process requires the energy of the photon (which is inversely proportional to wavelength) to equal the difference in energy between the two energy levels in the molecule. As such, absorption is energy dependent, and is therefore a spectral quantity.

The reduction in intensity of light as it passes through tissue due to absorption by chromophores can be described by the Beer-Lambert Law [186]:

$$I\left(d\right) = I_0 e^{-\varepsilon C d} \tag{2.1}$$

where $I\left(d\right)$ and I_0 are the intensity at distance d through the medium and initial intensity respectively, ε is the molar extinction coefficient (units: $\mu M^{-1} cm^{-1}$) and C is chromophore concentration (units: μM for HbO and Hb, and % for water concentration). The absorption coefficient, μ_a, provides information about the number of expected absorption events per unit length, and varies depending on the concentration of each of the n chromophores present in tissue [3, 187, 188]. Equation 2.2, derived from Beer's law, can be used to determine μ_a [35].

$$\mu_a(\lambda) = \sum_{i=1}^{n} \varepsilon_i(\lambda) C_i \tag{2.2}$$

Scattering is caused by structural components of tissue, for example: cells, subcellular species such as cell nuclei and other organelles, and the refractive index mismatch at the boundaries between structural components and different tissue types [3,187,188]. At red and near-infrared wavelengths, the total attenuation of tissue is at its lowest (Fig. 1.3 a) and therefore the transmitted light intensity is high, so long-wavelength bioluminescent reporters are desirable to maximise the signal that can be measured. The absorption of light at these wavelengths by tissue chromophores is low and therefore scatter dominates, making the passage of light through tissue diffuse [3, 187, 188].

The scattering coefficient, μ_s, describes the distance travelled by photons before they are scattered [187]:

$$\mu_s = \frac{1}{scattering\,length} \tag{2.3}$$

A second scatter parameter, the reduced scattering coefficient, μ_s' describes the distance travelled by a photon in a medium before initial directional information is lost [187]:

$$\mu_s' = \frac{1}{transport\,mean\,free\,path} \tag{2.4}$$

μ_s' is related to μ_s by the equation [187]:

$$\mu_s' \equiv (1-g)\,\mu_s \tag{2.5}$$

where g is the anisotropy factor which is the average of the cosine of the scattering angles in a particular medium. An anisotropy factor of close to 1 indicates that forward scattering is predominant [187]. For tissue, g ranges from 0.8-0.98 depending on the tissue [187], and so

light is likely to be forward scattered. These parameters are all wavelength dependent.

An expression for the reduced scattering coefficient can be derived from Mie Scattering Theory [35, 189]:

$$\mu_s'(\lambda) = sa\lambda^{-sp} \tag{2.6}$$

where sa and sp are the scatter amplitude and scatter power respectively, and λ is the wavelength in μm.

The diffuse propagation of light through tissue is described by the diffusion approximation to the radiative transport equation. This will be outlined in the following section.

2.2 Forward Model

The Forward Model describes the propagation of light from the light source (bioluminescent source in BLT or diffuse light source in DOT) to the surface of the imaging subject, calculating boundary data at pre-defined measurement locations (detectors) across the surface. The forward model is based on the diffusion approximation to the radiative transport equation, which is widely used to describe the diffuse propagation of light through tissue. For a continuous wave system (i.e. a system with a continuous light source) the diffusion approximation is given by the equation [34, 35]:

$$x(r) = -\nabla \cdot \kappa(r) \nabla \Phi(r) + \mu_a(r) \Phi(r) \tag{2.7}$$

where $x(r)$ is the light source (bioluminescent or diffuse) at position r, $\kappa = \frac{1}{3(\mu_a + \mu_s')}$ is the diffusion coefficient and $\Phi(r)$ is the fluence rate at position r.

A surface boundary condition is applied to the model, which enables fluence to be calculated at the boundary but prevents light from re-entering the imaging subject:

$$\Phi(\xi) + 2A\hat{\mathbf{n}} \cdot \kappa(\xi) \nabla\Phi(\xi) = 0 \tag{2.8}$$

where ξ is a point on the boundary, $\hat{n}$ is the surface normal directed out of the imaging subject, and A is derived from Fresnel's law:

$$A = \frac{2/(1-R_0)-1+|cos(\theta_c)|^3}{1-\mid cos(\theta_c) \mid^2} \tag{2.9}$$

where $R_0 = \frac{(n_1/n_{AIR}-1)^2}{(n_1/n_{AIR}+1)^2}$, for a medium with refractive index n_1 (n_{AIR} is the refractive index of air, $n_{AIR} = 1$). Total internal reflection occurs for photons passing from the medium to the free space outside the imaging subject at angle $\theta_c = \arcsin\left(\frac{n_{AIR}}{n_1}\right)$.

Equations 2.7 and 2.8 are implemented in this work by NIRFAST [35], a numerical modelling software which uses a finite element method (FEM) framework. The FEM method breaks the problem into finite elements, i.e. if the problem involved a murine model, a volume mesh of the animal would be produced containing elements (small volumes) and nodes (at the intersection of elements). For data taken using the BLDOT system the FEM mesh is created from three-dimensional surface capture data.

2.3 Free Space Model

Free Space modelling has been developed to account for the dependence of BLI measurements on the position of the imaging subject when using a non-contact imaging system for data collection. A change in position of the animal causes the perspective of the animal visible to the camera to change, causing the source to appear to be at a different position within the animal, producing a different surface flux and therefore different BLI measurements. This is demonstrated using a cylindrical phantom in Fig. 2.1. The position of a light source within the cylindrical phantom is shown in Fig. 2.1 a, and bioluminescence images of the phantom

at 0° and 60° shown in Fig. 2.1 b and c demonstrate the change in appearance of surface fluence visible by the CCD. Although the fluence at the surface is identical in both cases, the light which is measured at the CCD is different due to the change in the relative position of the source due to rotation of the phantom. The colourbars show a corresponding change in intensity measured at the CCD. The change in position of the cylinder is analogous to the change in position of an animal between imaging sessions or due to repositioning of an animal during an imaging session.

The variation in measurement intensity introduced by a change in position of the imaging subject may cause inaccurate conclusions to be drawn from a pre-clinical study. For example the growth of a tumour may appear less significant than it truly is, or a novel treatment less effective. Therefore, this dependence must be accounted for. Free space models have been developed to do this. These models model the propagation of light through the free space between the surface of the imaging subject and the CCD, and back again, mapping the CCD measurements back on to the surface of the imaging subject. The resulting surface measurements are independent of the position of the imaging subject. These models can, and should, be used for any optical imaging modality which uses non-contact imaging, including bioluminescence, diffuse transmission imaging for DOT and fluorescence imaging.

Ripoll *et al.* first developed a model of light propagation through free space which introduced the concept of approximating the focal plane of the system as a discretised array of virtual detectors [190]. Chen *et al.* built on this model by approximating the system such that the light propagation can be approximated as a simple thin lens problem [191] and included the ability to model multiple apertures present in the system, such as filter wheels [192]. The incorporation of the thin lens approximation was accompanied by the inclusion of visibility criteria, which enabled the visibility of points on the surface of the imaging subject by the CCD to be determined. Guggenheim *et al.* [27] extended the model further still to enable the focal plane to be placed arbitrarily relative to the imaging subject. The inversion method

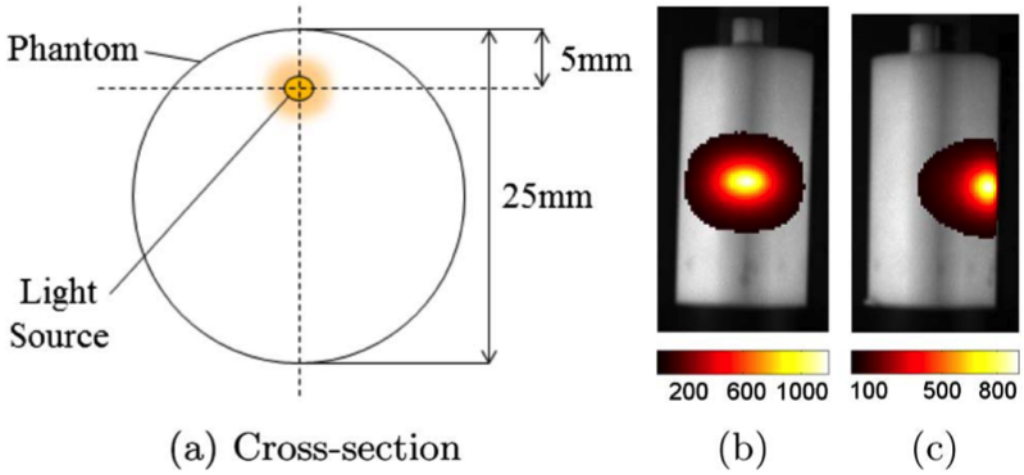

Figure 2.1: (a) Cross section through a plastic cylindrical phantom with an internal light source in the position shown. (b) and (c) are images of the phantom taken using the BLDOT system showing the change in appearance of the surface fluence visible at the CCD, and the change in measured intensity indicated by the colourbar scales. Colourbar units: counts s^{-1}. Reproduced from [27].

which maps CCD data back on to the surface of the imaging subject was also modified from a backprojection method [191, 192] to a non-negative least squares method which was found to improve the quantitative accuracy of the model [27].

The free space model developed by Guggenheim *et al.* was developed for use with the BLDOT system but can be applied universally provided the dimensions of the system are known. The model has been previously shown to be effective in accounting for the position of a cylindrical phantom [27, 28], but thus far work has not been done to validate the model using murine data. This validation is performed in Chapter 3 where the model is referred to as the 'free space model.'

2.4 Inverse Model

The inverse model uses boundary measurements to reconstruct either the source (in BLT) or the underlying optical properties of the imaging subject (in DOT). This section will give an

overview of the theory behind the reconstruction algorithms used for BLT and DOT in this work.

2.4.1 Inverse Model: BLT

Assuming the spectral optical properties (μ_a, μ_s') of the imaging subject are known, boundary measurements of the bioluminescent source (following free space modelling), b, are used to calculate the three dimensional internal bioluminescent source distribution, x. Due to the linearity of the solution to Eq. 2.7 with respect to the bioluminescent source $x(r)$, the BLT reconstruction problem is a linear problem. The problem aims to minimise the difference between the measured bioluminescence data, b, and simulated data, $F(x)$, which is calculated from Eq. 2.7 assuming knowledge of the underlying attenuation of the imaging subject (F is a model of light propagation that accounts for the underlying optical properties and geometry of the imaging subject). This minimisation can be solved as a Least-squares minimisation:

$$x = \min_x \parallel b - F(x) \parallel \tag{2.10}$$

The relationship between the internal source distribution, x, and the boundary measurements, b, is described by a sensitivity matrix, the Jacobian, J which has dimensions $N_m \times N_n$ (N_m is the number of boundary measurements, N_n is the number of nodes in the mesh). The boundary measurements can therefore be calculated using Eq. 2.11:

$$b = Jx \tag{2.11}$$

and the solution for x is given by the expression:

$$x = J^{-1}b \tag{2.12}$$

However, J is not square and is not directly inverted as $N_n \gg N_m$. The problem is also non-unique due to the possibility of multiple different bioluminescent sources producing identical surface measurements as shown in Fig. 1.4. The non-uniqueness can be reduced by using multi-spectral data such that J and b are defined:

$$J = \left[J_{\lambda_1^*};\ J_{\lambda_2^*};\ ...J_{\lambda_k^*}\right] \tag{2.13}$$

$$b = \left[b_{\lambda_1^*};\ b_{\lambda_2^*};\ ...b_{\lambda_k^*}\right] \tag{2.14}$$

where $J_{\lambda_i^*}$ and $b_{\lambda_i^*}$ are the Jacobian matrix and measurement vector at wavelength λ_i^* respectively (λ_i^* is defined as the central filter wavelength of the band pass filters used for data collection). Using spectral measurement data reduces non-uniqueness by exploiting the fact that tissue attenuation (and source emission) is spectral and therefore the recovered source distribution must satisfy the measurements at each wavelength. Utilising heterogeneous optical property distributions reduces the possible pathways of light through the imaging subject, thus further reducing non-uniqueness. The permissible source region can also be used an additional constraint [51, 193].

This work uses a Compressive Sensing Conjugate Gradient (CSCG) based algorithm to solve Eq. 2.12 [50] which reduces the ill-posed and non-unique nature of BLT reconstructions by assuming a sparse source distribution and using techniques inspired by compressive sensing, enabling more biologically plausible source distributions to be calculated. In the case of pre-clinical cancer research where the bioluminescent source is located within a tumour, the assumption of a sparse source distribution is appropriate. Work has shown the algorithm to outperform a number of more commonly used algorithms, including a non-negative least squares algorithm, in both simulation and experiment using a mouse-shaped phantom (XPM2) [50, 97].

2.4.2 Inverse Model: DOT

The inverse model for DOT aims to recover the internal optical property distribution of the imaging subject given knowledge of the external illumination source, x, and boundary measurements, b. Due to the non-linearity of Eq. 2.7 with respect to the optical properties μ (μ_a and μ_s') the DOT reconstruction problem is an iterative process.

A three-dimensional model of the imaging subject is created and the positions of the DOT light sources are placed on the lower surface of the mesh. In order to calculate the optical properties the following iterative process is implemented:

- Start with an estimate of μ and use this to calculate an estimated Jacobian, $J(\mu)$ and modelled boundary data.
- Compare the modelled data to the actual measurement data to calculate an update to μ, $\delta\mu$.
- Iterate the above steps, modifying μ, until the difference between the simulated and actual measurement data is minimised (according to pre-defined stopping criteria, a difference of $<2\%$ is used in this work).

This process is followed for both the single-wavelength (standard) and spectral case which recover μ_a and μ_s' and chromophore concentrations respectively. The methods for these will be outlined in the following sections and can be found in more detail in ref. [35].

2.4.2.1 Standard Reconstruction

Mathematically, using a Tikhonov minimisation procedure, the reconstruction can be represented as [35]:

$$\chi^2 =_{\mu}^{min} \left\{ \sum_{i=1}^{N_m} \left(\Phi_i^M - \Phi_i^C \right)^2 + \zeta \sum_{j=1}^{N_n} \left(\mu_j - \mu_0 \right)^2 \right\} \tag{2.15}$$

where Φ_i^M and Φ_i^C are measured and calculated fluence respectively, μ_0 is an initial optical property estimate which can be obtained via a data calibration procedure (see Chapter 6 of ref. [194] and Chapter 8 of ref. [48] for details) or from prior knowledge, e.g. incorporating structural information from CT or MRI as described in Chapter 1, with literature values for tissue optical properties, or using atlas models, such as the Digimouse atlas [42]. ζ is the Tikhonov regularisation parameter: $\zeta = \frac{\sigma^2_{\Phi^M}}{\sigma^2_\mu}$, the ratio of variances of the measurement data and optical properties [35]. The data calibration procedure also accounts for the offset in Φ^M and Φ^C due to differences in the initial external source strength for the two data sets [194].

In order to calculate the solution to Eq. 2.15, the solution to Eq. 2.16 must be calculated iteratively, decreasing ζ with each iteration, to determine the update to the optical properties, $\delta\mu$.

$$\left(J^T J + \tilde{\zeta} I\right)^{-1} J^T \delta\Phi = \delta\mu \tag{2.16}$$

$\delta\Phi$ is the data-model mismatch (recalculated at each iteration), $\tilde{\zeta} = 2\zeta$ and the Jacobian, J is defined as the rate of change of calculated data with small modifications to optical properties [35]:

$$J = \frac{\partial \Phi^C}{\partial \mu} \tag{2.17}$$

The solution to Eq. 2.16 for $\delta\mu$ is calculated until the data-model mismatch is reduced to a pre-defined tolerance, typically 2%. This is done at each required wavelength. Chromophore concentrations and scattering parameters (scatter amplitude, *sa*, and scatter power, *sp*) can then be calculated using Eq.'s 2.2 and 2.6, [35, 189]. Alternatively, the chromophore concentrations, c, can be reconstructed directly from spectral data using the spectral reconstruction process.

2.4.2.2 Spectral Reconstruction

This is the approach taken in the work presented in Chapters 5 and 6, where HbO, deoxyHb and water concentrations are considered. Similarly to Eq. 2.17 the spectral Jacobian is defined for each parameter as:

$$J_{c,\lambda} = \frac{\partial \Phi}{\partial c} \mid_{\lambda} \tag{2.18}$$

i.e. the rate of change of amplitude of measured data with chromophore concentration (phase information is also included, but when considering the BLDOT system which is a continuous wave system, only amplitude data is acquired). Similar Jacobians are calculated for *sa* and *sp*:

$$J_{sa,\lambda} = \frac{\partial \Phi}{\partial sa} \mid_{\lambda} \tag{2.19}$$

$$J_{sp,\lambda} = \frac{\partial \Phi}{\partial sp} \mid_{\lambda} \tag{2.20}$$

The Jacobian for each parameter (Eq.'s 2.18, 2.19 and 2.20) has dimensions of $\{N_m \times N_n\}$ for N_m measurements and can be combined into a single linear problem for k measurement wavelengths (Eq. 2.21, assuming three chromophores but can be extended to include more) to solve the spectral case for chromophore concentrations c_i and scattering parameters *sa* and *sp*.

$$\begin{pmatrix} \partial\Phi_{\lambda 1} \\ \partial\Phi_{\lambda 2} \\ \vdots \\ \partial\Phi_{\lambda k} \end{pmatrix} = \begin{bmatrix} J_{c1,\lambda 1} & J_{c2,\lambda 1} & J_{c3,\lambda 1} & J_{sa,\lambda 1} & J_{sp,\lambda 1} \\ J_{c1,\lambda 2} & J_{c2,\lambda 2} & J_{c3,\lambda 2} & J_{sa,\lambda 2} & J_{sp,\lambda 2} \\ \vdots & \vdots & \vdots & \vdots & \vdots \\ J_{c1,\lambda k} & J_{c2,\lambda k} & J_{c3,\lambda k} & J_{sa,\lambda k} & J_{sp,\lambda k} \end{bmatrix} \begin{pmatrix} \partial c_1 \\ \partial c_2 \\ \partial c_3 \\ \partial sa \\ \partial sp \end{pmatrix} \tag{2.21}$$

The dimensions of the combined Jacobian matrix are {number of wavelengths $\times$ N_m} $\times$ {N_n $\times$ number of parameters} the simplified structure of the Jacobian is shown in Fig. 2.2 (assuming three measurement wavelengths and three chromophores and ignoring scattering parameters). Update Eq. 2.16 is solved for $\delta\mu$, as with the standard case, but $\delta\mu$ now relates to the chromophore concentrations and scatter parameters. A number of physiological constraints are applied to the reconstruction: maximum water content limited to 100%, scatter parameters and concentrations of HbO and deoxyHb constrained to non-negative values [35].

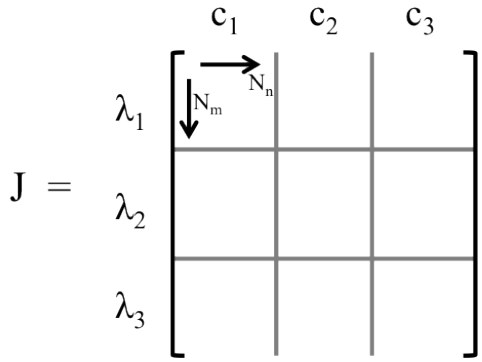

Figure 2.2: Structure of the spectral Jacobian for data at three wavelengths, λ_i, and assuming three chromophores, c_i. N_m is the number of measurements and N_n is number of nodes.

2.5 Summary

This chapter has given an overview of the methods used to model the propagation of light through tissue and factors which affect the path taken by the light. This work uses the diffusion approximation to the radiative transport equation to model the light propagation through the imaging subject (either phantom or murine models) implemented through the forward and inverse models. In a non-contact imaging system such as the BLDOT system it is important to additionally model the light propagation through the free space between the surface of the imaging subject and the detector (CCD) using the free space model.

Thus far, the free space model implemented in this work has only been validated in phantom studies. The work presented in Chapter 3 applies the model to murine data for the first time. This is important work which aims to determine the applicability of the model to *in vivo* pre-clinical studies. As explained above, the inverse model for BLT currently ignores the bandwidth of the band pass filters used for multi-spectral data collection. Chapter 4 includes work which investigates the effect this has on the quantitative accuracy of the recovered source. A new filter bandwidth model for BLT is presented and applied to simulated and phantom data with a view of improving the quantitative accuracy achievable by BLT. The model is then validated in a murine environment in Chapter 6. Chapter 5 outlines a spectral derivative method for DOT. The applicability of the model in non-contact imaging is investigated for the first time, through simulation, evaluating the ability of the model to remove the need for free space modelling and DOT data calibration prior to full tomographic reconstruction. The model is then applied to data acquired using the BLDOT system in Chapter 6, determining the efficacy of the model when applied to murine data.

Chapter 3

Validation of a Free Space Model Applied to Murine Bioluminescence Data

The application of free space modelling to phantom BLI data has demonstrated substantial improvements to the quantitative accuracy of measured fluence [27, 48]. Thus far the model has not been validated in small animal imaging, and this is vital in order to determine whether the model will be effective when applied in pre-clinical studies. This chapter builds on the previous phantom work, applying the model to murine BLI data acquired using the BLDOT system for the first time, validating the model for use in small animal imaging.

3.1 Introduction

Bioluminescence imaging has numerous applications in pre-clinical studies (see Section 1.1.1), including in assessing the efficacy of novel cancer treatments by monitoring tumour growth [1, 6, 195], and studies into the localisation of stem cells within a murine model [13, 14]. However, the quantitative accuracy is limited. For instance, an animal with an internal bioluminescent source may be imaged on two different occasions on the same day, and produce

two different BLI measurements as the perspective of the animal visible at the CCD may be different. This measurement variation may be due to a slight change in position of the animal or a change in the underlying optical properties.

The underlying optical properties of the animal are determined by the concentrations of different tissue chromophores (Fig. 1.3 a). If, for example, the oxygen saturation of the tissue were to decrease (hypoxia), the ratio of HbO to deoxyHb will change, and the total attenuation of the tissue will change, resulting in a different surface fluence arising from an internal bioluminescent source. These factors make it difficult to accurately quantify the bioluminescent source intensity and may cause inaccurate conclusions to be drawn during pre-clinical studies about how effective a treatment is or how quickly a tumour is growing for example.

The change in position of the animal can be accounted for by modelling the propagation of light from the surface of the animal to the CCD using a free space model [27]. This models the propagation of light from the surface of the imaging subject to the CCD calculating a transfer matrix which describes the contribution of each point on the surface of the imaging subject to each pixel in the CCD. Inverting the relationship enables CCD data to be mapped back on to the surface of the imaging subject, determining true surface fluence values which are independent of the position of the imaging subject (see ref. [27] for more detail).

The efficacy of this free space model in accounting for the change in position of a cylindrical phantom in the BLDOT system has been previously demonstrated [27, 28, 48]. However, the efficacy of the model when applied to animal data has not yet been demonstrated. In this chapter, the free space model is applied to murine BLI data taken using the BLDOT system, demonstrating that the ability of the model in accounting for a change in position is effective in a murine model. This data was presented at the World Molecular Imaging Congress 2015 and European Conferences on Biomedical Optics 2015.

3.2 Methods

The BLDOT system was used to image three mice *post mortem*[1] with an artificial light source (tritium-based, Trigalight Orange III; mb-microtec, Switzerland) inserted in positions shown in Table 3.1. This particular light source was chosen due to the similarity in emission to that of firefly luciferase (fluc), as shown in Fig. 3.1, the peak emission intensity of the artificial light source occurs at 607 nm, while that of firefly luciferase (fluc) is at 612 nm. However, there are some disadvantages to using the trigalight source as a model of fluc: it is possible that the emission from the artificial source is of a higher intensity than that from an equivalent volume of fluc-labelled cells, and will therefore produce BLI images with a higher SNR. Additionally, the trigalight source is a well-defined volume, however *in vivo* fluc-labelled cancer cells will not produce a well-defined volume. *In vivo* the cells will be actively proliferating and infiltrating the surrounding tissue and it is possible for cells to dissociate from the tumour. The trigalight source is unable to model this tumour growth. Despite these differences between the artificial source and BLI *in vivo*, the trigalight source is considered a good model to use in this work, testing the validity of the Free Space model in a *post mortem* murine model due to the similarity of the emission spectra (Fig. 3.1). The trigalight source acts as an ideal tumour, well defined and with a high emission intensity, which is a reasonable intermediate experiment to perform between phantom experiments and *in vivo* work. Note that it is not possible to use fluc-labelled cells in a *post mortem* model as bioluminescent emission is a metabolic process (as explained in Section 1.1.1) and therefore requires an *in vivo* model.

In order to insert the source (Fig. 3.2), a hypodermic needle (Henke-Sass, Wolf GmbH, Tuttlingen, Germany; 18 gauge with an outer diameter of 1.2 mm) was inserted to the required depth within the animal. The source was introduced through the bore of the needle,

[1]The animals used in this work were donated by the Biomedical Services Unit, Birmingham as they were not suitable for use in the pre-clinical studies they were intended for. This was due to the genetically altered genotype being incorrect and unsuitable for use elsewhere.

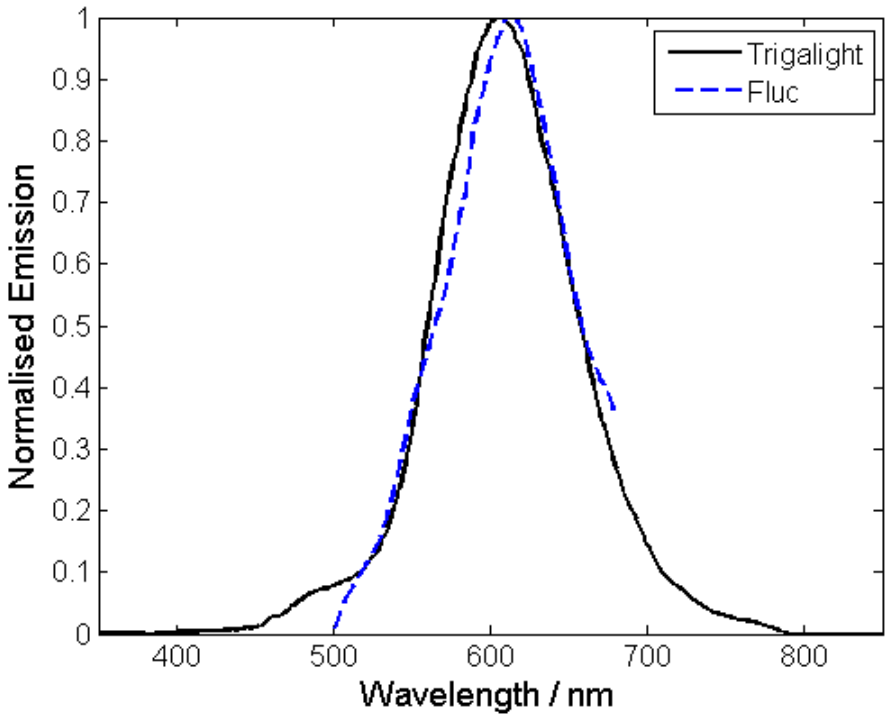

Figure 3.1: Emission spectrum of the artificial light source, 'Trigalight', (tritium-based, Trigalight Orange III; mb-microtec, Switzerland) used in these experiments, obtained from manufacturer data (presented in Appendix A.1 of ref. [48]). The spectrum is similar to that of firefly luciferase ('Fluc', dotted lines; data supplied by Dehghani et al. [26]).

followed by wire which was used to force the source out of the needle and into the animal, enabling the needle to be removed, leaving the source in position.

To insert the source subcutaneously, the needle was inserted through the skin by 'pinching' the skin using tweezers. Insertion of the source at any greater depth is approximate. It is possible that the source could move to a more superficial location as the needle is withdrawn. Additionally, source insertion was performed away from the imaging system and the animal subsequently moved and placed onto the imaging platform. The internal organs of the animal may have moved in this process, causing the position of the source to change, or the skin and shape of the animal may have changed resulting in the source moving to a different depth. Care was taken to minimise these factors however they will be present to some extent

whenever this method of source insertion is used.

It would be possible to determine the true source location within the animal using a second imaging modality, such as ultrasound, but in this experiment the true source location is not considered to be important. This work aims to determine the efficacy of the Free Space Model in accounting for the dependence of measured bioluminescence on a change in position of the animal. Therefore, as long as the position of the source within the animal is consistent between the two positions the animal is imaged in (positions detailed below) the efficacy of the Free Space Model can be determined. The assumption has been made that the source position is constant between the two positions. Once the needle used for source insertion is removed from the animal it is possible that the source could move slightly within the animal. This movement is believed to be negligible due to the care that was taken when moving the animal to the imaging platform after source insertion and when changing the position of the animal to the second position. Additionally, by the time imaging of the second of the animal was performed, rigor mortis was beginning to set in, reducing the possible movement of the source within the animal.

Table 3.1: Source depth and position, and rotation angle of the animal, for the three animals used in this study.

Mouse	Approximate Source Depth	Source Position	Approximate Rotation
1	Subcutaneous	Right dorsally	6^o
2	5 mm	Right laterally in abdomen	23^o
3	Subcutaneous	Right laterally in abdomen	44^o

BLI images of each animal were taken at 600 nm (band pass filter with bandwidth 22 nm, Semrock Inc.) with 4× binning and exposure times limited to 60 s, along with a three-dimensional surface capture, with the animal in two different positions: (1) the source position pointing towards the CCD (mouse 1 placed prone, mice 2 and 3 on the left side) and (2) animal rotated by an angle, ϑ, as indicated in Table 3.1.

The method of calculation of ϑ is shown in Fig. 3.3: After free space modelling the

BLI data is viewed on the mesh surface via the x-z axis. This enables the location of the maximum bioluminescence intensity to be determined (indicated by crosses in Fig. 3.3) and, as the mesh coordinates of the maximum BLI intensity and the base of the mesh are known,

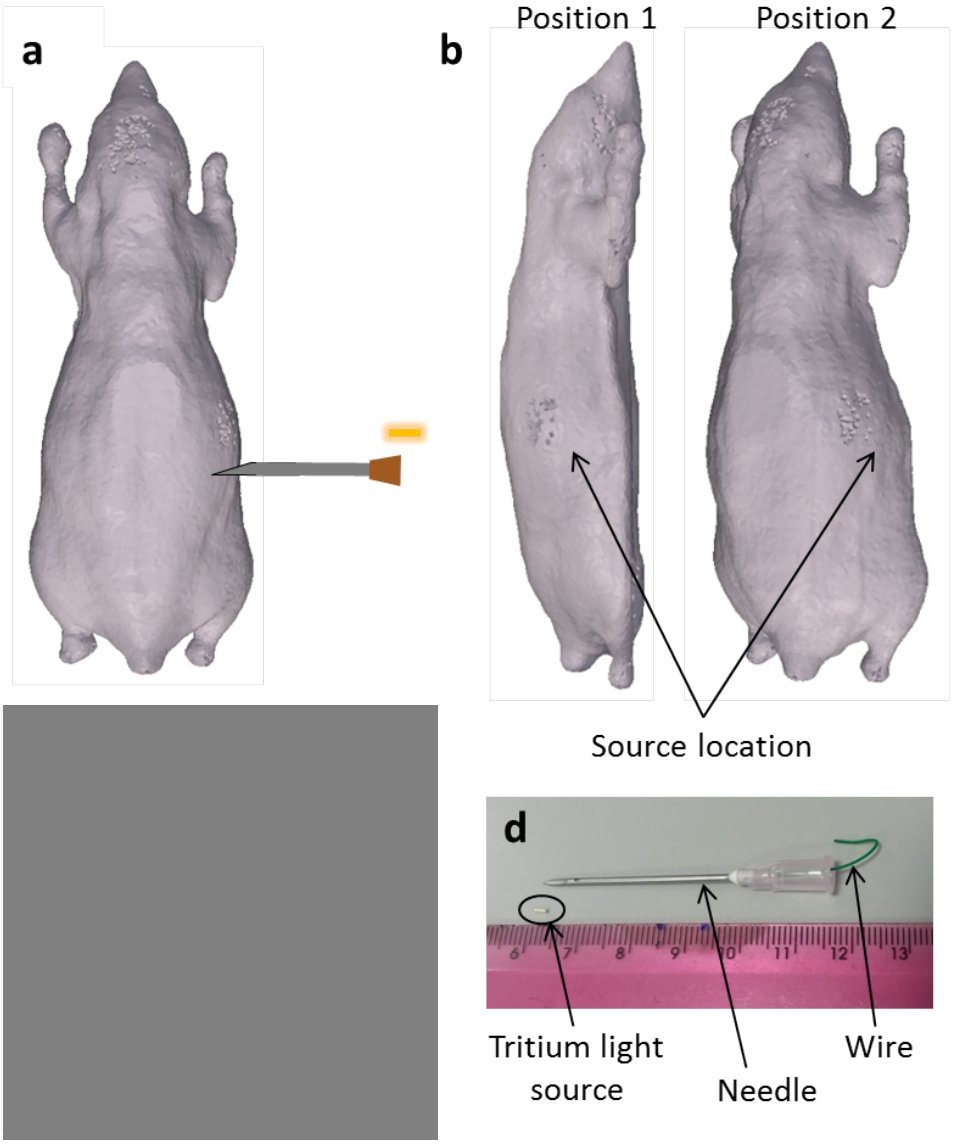

Figure 3.2: Insertion of a tritium light source into a mouse. (a) Schematic of the source insertion, with the light source and hypodermic needle shown. (b) Schematic of the two positions at which data was collected in the BLDOT system. (c) Source insertion into a mouse cadaver, the needle is in position. (d) Equipment used during source insertion, the source is inserted into the bore of the needle and the wire is used to force the source out when the needle is in position in the animal.

the angle from vertical of the location of the maximum bioluminescence intensity is calculated for each position (φ_1 and φ_2). The angle of rotation between the two positions, ϑ, can then be calculated using the equation: $\vartheta = \mid \varphi_2 - \varphi_1 \mid$.

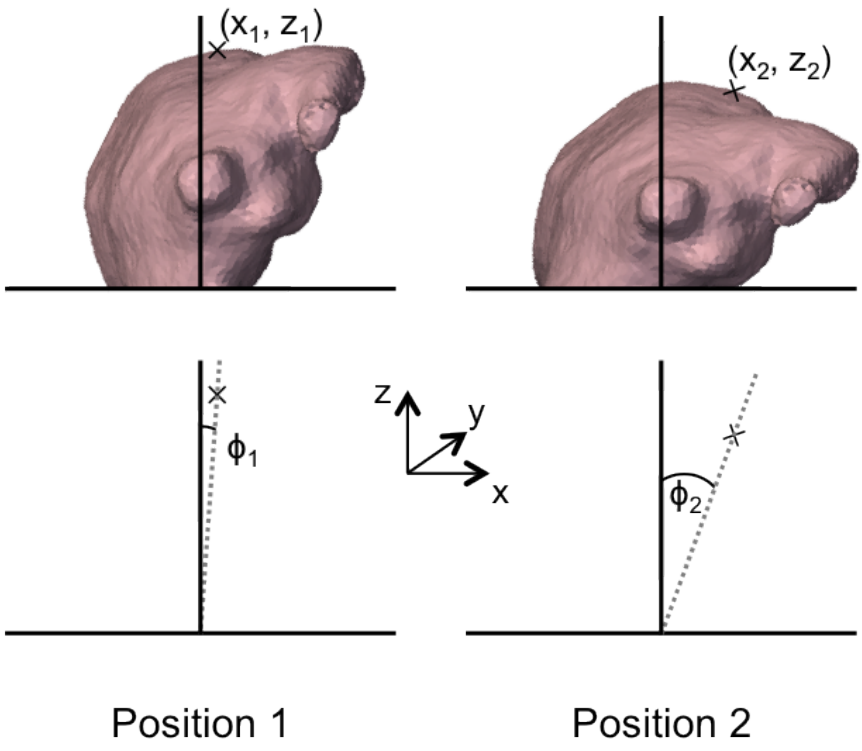

Figure 3.3: Determination of the angle of rotation between position 1 and position 2. The diagrams here show the animal from the tail end. The cross in each of the diagrams indicates the location in the x-z plane of the maximum bioluminescence intensity. The angle from vertical of each of the maximum intensity locations, φ, is calculated enabling the angle of rotation of the animal to be determined by calculating the difference between φ_1 and φ_2.

The angles of rotation used in this animal study are $\leq 45°$ and therefore the region of the animal surface containing the maximum intensity is visible by the CCD in all cases. Due to this, the method of calculating the angle of rotation described above is considered suitable for this application. If the angle of rotation was much greater, the maximum intensity location would not be visible by the camera and so a more suitable method should be implemented, such as registration of the three-dimensional meshes of the animal created from the surface

capture data from both positions.

The aim of this work is to determine the effect of changing the position of the animal on the measured bioluminescence. The free space model was applied to the BLI data obtained with a view of demonstrating that any effect of position on quantitative bioluminescence data can be accounted for. This work represents the first application of the free space model to murine data and is an important step towards widespread implementation of the model in pre-clinical studies.

3.3 Results and Discussion

Raw bioluminescence images of mice 1-3 in two positions, overlaid onto a bright image are shown in Fig. 3.4 (top row). The difference in position of each animal after rotation is demonstrated in these images, and the change in appearance of the surface fluence can be seen. There is a variation in intensity measured for each animal in the two positions, as shown in Fig. 3.5 a (graphs of total intensity normalised to the maximum for each animal, and considered only above a threshold of 50% of the maximum intensity), supporting the findings of the previous phantom work [27,28]. The percentage variation in intensity between the two positions is shown in Table 3.2, with all animals showing a variation of >30%, demonstrating that even a small rotation of $\sim 6^{o}$ can introduce large errors into the measured bioluminescence intensity.

Table 3.2: Variation in intensity between position 1 and position 2 for the three animals for raw bioluminescence data, $\triangle$I, and corrected bioluminescence data, $\triangle$I$'$. The decrease in variation between the two positions is more than 25% in all cases.

Animal	Approximate Rotation	$\triangle$I / %	$\triangle$I$'$ / %
Mouse 1	6^{o}	33	5.7
Mouse 2	23^{o}	53	22
Mouse 3	44^{o}	42	17

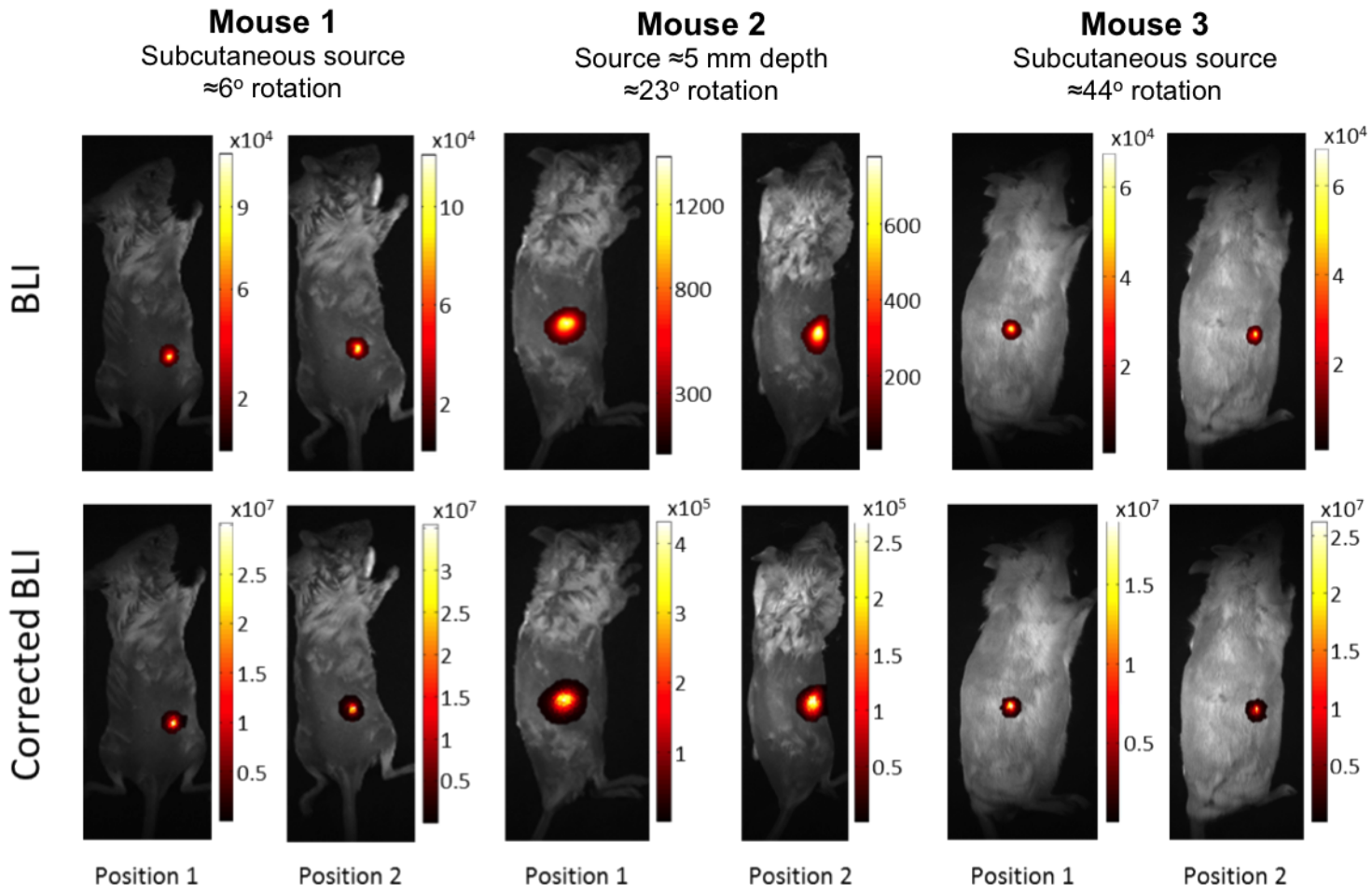

Figure 3.4: Raw and corrected BLI of mice 1-3 in two different positions. The approximate angle of rotation between the two positions is indicated. The corrected BLI images qualitatively correspond to the raw BLI images. Colourbar units: BLI - Intensity / counts s^{-1}, Corrected BLI - Arbitrary Intensity Units.

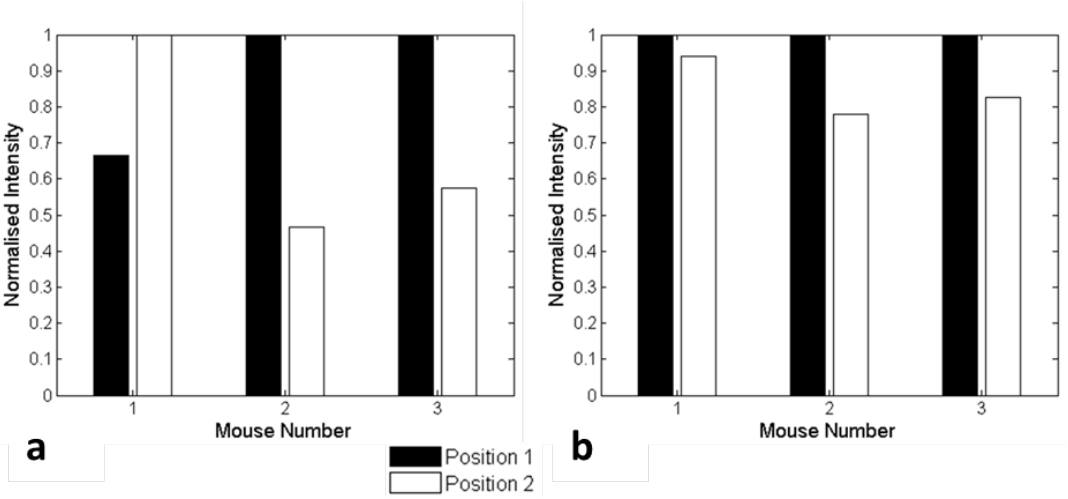

Figure 3.5: Total intensity (above 50% of the maximum intensity) of (a) raw and (b) corrected BLI data for mice 1-3, normalised to the maximum for each animal. The large difference in intensity between the two positions is demonstrated in (a), while the considerably smaller intensity variation after free space modelling is shown in (b).

Images of the data following free space analysis, 'Corrected BLI', overlaid onto a bright image of each animal are shown in Fig. 3.4 (bottom row), this data qualitatively resembles the raw BLI data. The total intensity of this data (considered above a threshold of 50% of the maximum value) is plotted in Fig. 3.5 b showing a reduction in the intensity variation of up to 31% (Table 3.2). Therefore, the effect of changing the position of the animal on the measured bioluminescence has been reduced.

Mouse 2 has the largest variation in intensity between the two positions in both raw and corrected bioluminescence images. It is possible that this is due to the increased depth of the source within the animal (≈ 5 mm) as compared to mice 1 and 3 (subcutaneous). The animals used in this work are *post mortem*, and as such the tissue oxygenation decreases as the time after animal sacrifice increases (data demonstrating this effect, which caused a reduction in measured intensity of up to 10%, and a 5% change in the first five minutes, is presented in Chapter 5, Fig. 5.3). This is a highly heterogeneous variation as the underlying anatomy of the animal is heterogeneous and the blood ceases to circulate when the heart stops beating,

so it is possible that blood collects in different regions of the anatomy. The exact time between animal sacrifice and imaging is unknown for mice 1 and 2, but imaging in this work commenced between 15 and 30 minutes following animal sacrifice. There was approximately 30 minutes between the commencement of imaging in the two different positions for mouse 2. This is due to changing the position of the animal, taking a three-dimensional surface capture (usually this takes approximately 4 minutes, however due to imaging system problems the surface capture of position 2 for this animal took 10 minutes) and imaging took approximately 16 minutes. Over this period of time the tissue oxygenation, and therefore the ratio between HbO and deoxyHb, would have decreased causing a change in the tissue attenuation of mouse 2 between the two positions. Therefore, it is likely that the surface fluence had changed. Free space modelling may have accounted for the change in position of the animal more effectively than is apparent, but because the surface fluence had truly varied between the two positions it was impossible to recover the same BLI measurement in both cases. This is also true to some extent for mouse 1, which had a period of 25 minutes between imaging in the two positions (there was a shorter imaging time of approximately 8 minutes 35 s due to the more superficial position of the source). However, due to the superficial position of the source, the attenuation variation affected the surface fluence to a lesser extent.

The imaging for mouse 3 started approximately 50 minutes after sacrifice of the animal with only 15 minutes between the commencement of imaging in the two positions. The variation in corrected bioluminescence intensity between the two positions still present after Free Space modelling could again be due to the change in tissue attenuation, but it is thought that the change in tissue attenuation will have stabilised due to the long delay between animal sacrifice and imaging. So it is possible that the Free Space model has struggled to effectively account for the large change in position for this animal ($\approx 44^{o}$). The variation in intensity between the two positions has, however, been reduced by the Free Space model showing some improvement through use of this method. More controlled experiments (detailed below) will

better enable the true efficacy of the model to be determined.

The reduction in intensity variation between the two positions is most pronounced for the smallest rotation (mouse 1, $\sim 6^{o}$) which is considered to be most relevant to pre-clinical imaging. A change in position such as this could arise during live animal imaging from repositioning an animal to ensure the nose cone which sustains anaesthesia is positioned appropriately, or due to placing the animal in the imaging system for different imaging sessions. However, the reduction in intensity variation for the larger rotations (mouse 2, $\sim 23^{o}$; mouse 3, $\sim 44^{o}$) proves the model is capable of accounting for larger positional changes should they arise.

The remaining discrepancy in intensity between the two positions is not believed to be due to the irregular shape of the animals as the Free Space Model is applied individually to images taken in the two positions. Three dimensional surface capture images of the animals are taken at each position to enable a subject-specific mesh to be created for each animal in each position, and the Free Space Model applied to each mesh individually. Therefore, deformation of the animal between the two positions should not affect the calculation of the corrected intensity, as the current shape of the animal is known via surface capture data.

The variation in intensity still present is thought to be due in part to the nature of this experiment, using mouse cadavers, which results in the underlying tissue attenuation varying throughout the course of data collection. To determine whether the change in tissue oxygenation is the true cause of the remaining variation between the two positions following Free Space Modelling it is important to repeat this experiment in a more controlled manner. To remove the inter-animal uncertainty present in this work, multiple animals should be imaged with the same source depth, determined using a secondary imaging modality such as ultrasound. Additionally, it would be valuable to control the degree of rotation more strictly. Rotations should be kept consistent between animals, with multiple rotations performed for each animal to determine the efficacy of the Free Space Model in accounting for multiple

rotations, rather than the single rotation in the data in this chapter. The animals should also be imaged at a consistent time after death to remove any effect of variation of tissue oxygenation between animals.

In the future it is important to determine the true efficacy of the free space model in accounting for positional changes of animals, by performing live animal imaging. Additionally this will be more appropriate for demonstrating the efficacy of the model for use in pre-clinical imaging.

3.4 Conclusions

The quantitative accuracy of BLI is dependent on the position and underlying optical properties of the imaging subject. A free space model has previously been shown to effectively account for the positional changes when applied to phantom data and this work demonstrates the efficacy of the model when applied to murine data for the first time. It was important to validate the model in a murine environment to determine whether the model will be effective when applied in pre-clinical studies. The data presented here showed the model to be able to reduce the error in bioluminescence measurements introduced by positional changes in the animal. However, as the animals were *post mortem* it is thought that the efficacy of the model was limited by changing attenuation over the timescale of data collection. To accurately determine the limitations to the efficacy of the model this work should be repeated in a more controlled manner, with consistent source depth, rotation angles and time after death, as detailed in Section 3.3. The work should also be repeated *in vivo*, but these first results on the application of the free space model to murine data are encouraging. The data presented here shows the free space model to be effective in reducing positional variation when applied to BLI data, however the method can be applied to any modalities which produce non-contact surface fluence measurements, such as DOT and FLI. Moreover, it is possible to

apply the model to data from any non-contact imaging system provided the dimensions of the system are known.

The efficacy of the free space model, in improving the quantitative accuracy of BLI surface data for use in further analysis (BLT and DOT reconstructions for example), has been demonstrated in this chapter. Additionally, other methods of accounting for the errors in the measurements which accompany a change in position of the imaging subject are under investigation, in order to reduce the reconstruction time for both BLT and DOT. For example spectral derivative methods (see Chapter 5 and 6).

Chapter 4

Effect of Filter Bandwidth on the Quantitative Accuracy of Bioluminescence Tomography

In Chapter 3 the efficacy of the free space model in reducing the dependence of surface measurements on the position of the animal was demonstrated. These surface measurements provide a starting point for performing further analysis, such as BLT and DOT. However, there are additional factors which limit the quantitative accuracy of BLT.

This chapter investigates the effect of ignoring the bandwidth of band pass filters (which are used for multi-spectral data collection) on the quantitative accuracy of BLT. A method of accounting for the filter bandwidth in the BLT reconstruction algorithm is presented and the efficacy of the model in producing quantitatively accurate BLT reconstructions is determined (this data was presented at SPIE Photonics West 2015). The data presented to validate the model uses multi-spectral data acquired at only three wavelengths. Usually, when acquiring multi-spectral BLI data for BLT with the BLDOT system, five or six wavelengths are used [48, 49]. The second section of this chapter investigates whether using three wavelengths for

data collection has any detrimental effect on the quantitative accuracy of BLT.

This chapter is based on work published in ref.'s [96] and [196] and sections of the text have been reproduced from these references.

4.1 Introduction

As discussed previously, BLI has a number of limitations. The work presented in Chapter 3 showed that the dependence on the position of the animal can be accounted for. A further limitation to BLI is that the images are planar, so it is impossible to determine the true location of the bioluminescent source within the animal. For instance, a deep but small and intense source may produce very similar surface fluence to a weaker but larger and more superficial source (as demonstrated in Fig. 1.4) [26]. BLT makes steps towards overcoming this limitation by reconstructing a three-dimensional estimate of the distribution of the bioluminescent source within the animal from multi-spectral BLI data.

When performing BLT, multi-spectral data collection is facilitated by using band pass filters. However, the bandwidth of the filters used for data acquisition is currently not considered in the reconstruction algorithm, with the data assumed to be collected at the central filter wavelength [26, 34, 35, 50–52]. This is an incorrect assumption to make. For a given filter, data are collected over the range of wavelengths which are transmitted through that filter. For example, for a filter with a central wavelength of 600 nm and a bandwidth of 20 nm, the data collected consists of data from all wavelengths in the range 590-610 nm. Ignoring this and assuming all data comes from the central filter wavelength will introduce a model-data mismatch during model-based image recovery. This is because the range of wavelengths which are transmitted through the filter, and therefore the spectral properties of both tissue attenuation and bioluminescent source emission within the bandwidth of the filter are not considered, resulting in a loss of accuracy in the reconstruction.

The work presented in this chapter examines the effect of ignoring filter bandwidth in BLT source recovery through both simulation, using a complex mouse model (Digimouse atlas), and experiment, imaging a mouse phantom (XPM2, Perkin Elmer) in the BLDOT imaging system. A filter bandwidth model, which is incorporated into the BLT reconstruction algorithm, is presented and the effect of the model on the quantitative accuracy of the simulation and phantom data is determined. This work is done using three wavelengths in the multi-spectral data collection, which is fewer than the five or six which are currently used in the BLDOT system [48, 49] and others [34, 36, 52], so the second section of this chapter investigates whether using selected wavelengths has an effect on the quantitative accuracy of BLT. A secondary result from this work, if quantitative accuracy can be preserved when using wide bandwidth filters and fewer wavelengths, is a reduction in data acquisition time for BLT. This will enable imaging to be done during the window of time over which the maximum emission intensity of the bioluminescent reporter occurs ($\sim$10-20 minutes for Firefly luciferase, fluc [75]), whilst minimising the time for which an animal is under anaesthetic and increasing the imaging throughput.

First the filter bandwidth modelling will be outlined, followed by results on the effect of filter bandwidth on the quantitative accuracy of BLT, with and without including filter bandwidth modelling in the reconstruction. Finally results on the effect of using fewer filters for multi-spectral data collection will be presented.

4.2 Incorporating Filter Bandwidth Modelling into the BLT Reconstruction Algorithm

This section details modifications to the existing BLT reconstruction algorithm to incorporate filter bandwidth modelling. This modified algorithm will be validated in Section 4.4 through both simulation, using the Digimouse model and experiment, using the XPM2 mouse shaped

phantom.

When performing bioluminescence tomographic reconstructions, surface-weighted measurements are used along with reconstruction algorithms to recover the internal bioluminescent source [26]. Given a known source distribution, x, and a model of light propagation, J, the boundary measurements, b, are given by a linear relationship ($Jx = b$, Eq. 2.11). As explained in Chapter 2, the Jacobian, J, and measurement matrix, b, are created from a combination of Jacobians/measurements (Eq.'s 2.13 and 2.14) for each of the measurement wavelengths, λ_i^* (the central filter wavelength of the band pass filters used for data collection).

Since the measurements, $b_{\lambda_i^*}$, are assumed to be from a single wavelength, λ_i^*, the corresponding Jacobians are calculated according to this assumption; these Jacobians will be referred to as the narrow bandwidth (NBW) Jacobians. However, as explained earlier, when using band pass filters for data collection, measurements are comprised of signal from all wavelengths which are transmitted through the filter, governed by its bandwidth, w. Therefore, assuming a band pass filter with a top-hat transmission profile with 100% transmission, the boundary measurements are more accurately given by:

$$\tilde{b}_{\lambda_i^*} = \int_{\lambda_j=\lambda_i^*-\frac{w}{2}}^{\lambda_i^*+\frac{w}{2}} b_{\lambda_j} d\lambda_j \tag{4.1}$$

where $\tilde{b}_{\lambda_i^*}$ is the measurement accounting for the bandwidth of the filter and b_{λ_j} is the measurement contribution from each wavelength λ_j transmitted through the filter. (Note that any filter transmission profile [such as a Gaussian model], not just top hat transmission, can be used by convolving the profile with the measurement data.) Approximating this expression as a sum, assuming discrete wavelengths yields Eq. 4.2.

$$\tilde{b}_{\lambda_i^*} = \sum_{\lambda_j=\lambda_i^*-\frac{w}{2}}^{\lambda_i^*+\frac{w}{2}} b_{\lambda_j} \tag{4.2}$$

By the same definition, the Jacobian to be considered for each measurement wavelength is defined as:

$$\tilde{J}_{\lambda_i^*} = \int_{\lambda_j=\lambda_i^*-\frac{w}{2}}^{\lambda_i^*+\frac{w}{2}} J_{\lambda_j} d\lambda_j \tag{4.3}$$

and assuming discrete wavelengths:

$$\tilde{J}_{\lambda_i^*} = \sum_{\lambda_j=\lambda_i^*-\frac{w}{2}}^{\lambda_i^*+\frac{w}{2}} J_{\lambda_j} \tag{4.4}$$

where $\tilde{J}_{\lambda_i^*}$ is the Jacobian for measurement wavelength λ_i^* including the bandwidth of the filter, and J_{λ_j} is the Jacobian matrix calculated for each wavelength transmitted through the filter. Using the definitions above, Eq. 2.11 becomes:

$$\tilde{J}x = \tilde{b} \tag{4.5}$$

where $\tilde{J}$ is the modified Jacobian accounting for the bandwidth of the filters used for data collection, and will be referred to as the wide bandwidth (WBW) Jacobian.

In order to evaluate the effects of including filter bandwidth in source recovery, both the NBW and WBW Jacobians are used for image reconstruction.

4.3 Methods

4.3.1 Simulation using a Heterogeneous Mouse Model

A three-dimensional heterogeneous mouse model (the Digimouse atlas [42]) with a bioluminescent pancreas (Firefly Luciferase, fluc) was used for simulation studies (Fig. 4.1). Tissue properties of the eight regions of the model are shown in Table 4.1 and the optical properties for each wavelength were calculated using appropriate extinction coefficients

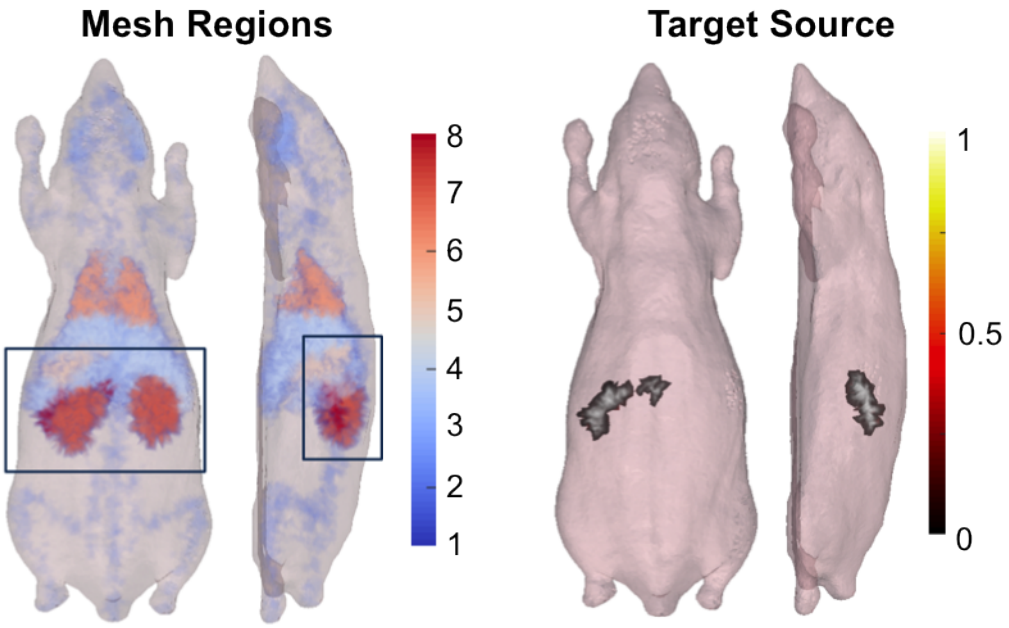

Figure 4.1: Digimouse model used in the simulations. The left image indicates the regions of the mesh, with the colourbar representing region number, as detailed in Table 4.1. Region 8 is the pancreas, which was made bioluminescent (fluc). 451 detectors were positioned uniformly across the surface of the mesh in the boxed areas. The bioluminescent pancreas alone is shown in the right image, colourbar units: modelled bioluminescence intensity. Adapted from [96].

(http://omlc.org/spectra/). A total of 451 detectors were modelled over the surface of the mesh above the pancreas, and simulated boundary data were calculated using NIRFAST, as explained in Section 2.2 [35].

Effect of Filter Bandwidth To determine the effect of filter bandwidth on the data quality, data were calculated at three measurement wavelengths, $\lambda^* = 600$, 620 and 640 nm, and eight different bandwidths (1, 2, 4, 6, 8, 10, 16 and 20 nm). The source emission spectrum over the range of wavelengths considered in this part of the study is shown in Fig. 4.2 b, along with the spectral coverage of the 1, 10 and 20 nm bandwidth filters (1 nm bandwidth spectral coverage covers the measurement wavelength only) assuming filters with top hat transmission profile and 100% transmission. BLT reconstructions on this noise-free data were performed using the CSCG reconstruction algorithm [50] using both NBW and WBW

Table 4.1: Tissue properties of the mouse mesh. [HbT] - total haemoglobin concentration, [StO_2] - oxygen saturation, [H_2O] - water concentration, sa - scatter amplitude, sp - scatter power. Reproduced from ref. [149].

Region	Tissue	[HbT] / mM	[StO_2] / %	[H_2O] / %	sa	sp
1	Adipose	0.0033	70	50	0.98	0.53
2	Bone	0.0049	80	15	1.4	1.47
3	Muscle	0.07	80	50	0.14	2.82
4	Stomach	0.01	70	80	0.97	0.97
5	Lungs	0.15	85	85	1.7	0.53
6	Kidneys	0.0056	75	80	1.23	1.51
7	Liver	0.3	75	70	0.45	1.05
8	Pancreas	0.3	75	70	0.45	1.05

Jacobians. In each case the WBW Jacobians are calculated for the bandwidth corresponding to the bandwidth used in data calculation. Noise-free data enabled evaluation of the filter bandwidth modelling in this best case scenario.

To determine whether there is any correlation between the filter bandwidth and the recovered source intensity, position (error in centre-of-mass compared to the true source location) and size (equivalent radius - the radius of a sphere of the same volume as the recovered source), the Pearson's correlation coefficient was calculated. In order to ascertain whether there was any significant difference between the sources recovered using the NBW and WBW models, a Wilcoxon signed rank test was performed on intensity, centre-of-mass and equivalent radius data from reconstructions using both models, assuming that the data are paired and non-parametric. The null hypothesis for this test was 'WBW reconstructions are the same as NBW reconstructions'.

Effect of Filter Selection To determine whether data can be acquired at fewer selected measurement wavelengths without compromising data quality, boundary data were calculated at five measurement wavelengths, $\lambda^* = 560$, 580, 600, 620 and 640 nm, which span the emission spectrum of fluc (Fig. 4.2 a), assuming a bandwidth of 10 nm. These measurements are

representative of the filters used in the BLDOT system.

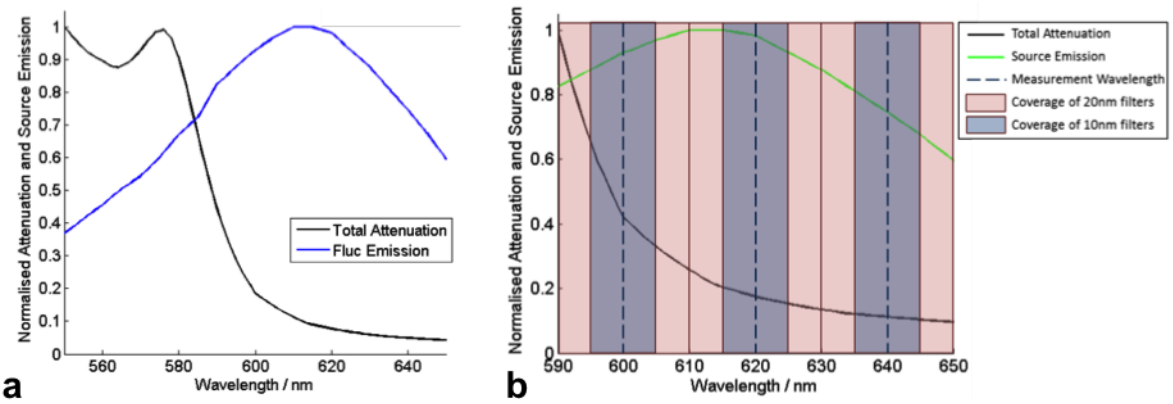

Figure 4.2: (a) Normalised total attenuation of tissue and emission spectrum of firefly luciferase (fluc). Measurement wavelengths are indicated on the x axis. The high attenuation of tissue and lower emission of fluc at 560 and 580 nm can be seen. (b) Normalised total attenuation of tissue and emission spectrum of fluc in the spectral region considered in the filter bandwidth study. Measurement wavelengths and the spectral coverage of 1, 10 and 20 nm filters indicated. Adapted from [96].

Tomographic source recovery was performed on the noise-free multi-spectral data, using the CSCG reconstruction algorithm [50] with the WBW Jacobian model (calculated according to the 10 nm bandwidth assumed during calculation of the data). Three different wavelength combinations were used for source recovery:

1. 5wv - All five wavelengths
2. 3wv_1 - 560, 580, 600 nm
3. 3wv_2 - 600, 620, 640 nm

These combinations of wavelengths used were chosen after considering the spectral attenuation of tissue and the source emission (Fig. 4.2 a) as follows: of the measurement wavelengths simulated, the tissue attenuation is highest at 560 and 580 nm, while the source emission is lowest at these wavelengths, so the measured bioluminescence intensity at these wavelengths is expected to be low. Therefore, when performing BLT using data from all five wavelengths

(5wv) the majority of the signal used for reconstruction is from the three higher wavelengths (600, 620 and 640 nm). Additionally the three higher wavelengths span the peak emission of fluc, which occurs at 612 nm [25] (Fig. 4.2). In order to determine whether the two lower wavelengths have any effect on the recovered source, it was decided that reconstructions would be performed using data at all five wavelengths (5wv), as is conventional when performing BLT data collection in the BLDOT system, the three lower wavelengths (3wv_1) and the three higher wavelengths (3wv_2) which are expected to produce recovered sources similar to the 5wv reconstruction due to the high signal at these wavelengths.

It is important to note that 3wv_1 and 3wv_2 combinations of wavelengths also span a narrower region of the emission spectrum than the coventionally used 5wv. This simulation is concerned with the effect of using fewer wavelengths, and in this specific case (which should apply to all *in vivo* murine experiments which use fluc as the bioluminescent reporter in BLT) the logical selection of fewer wavelengths for data collection, as described above, results in wavelengths for data collection which span a narrower range of the spectrum. In the future it is important to determine the effect of using wavelengths for data collection which span a narrower range. For example the experiment presented here could be repeated using 5wv and then using five wavelengths which span a narrower range of the spectrum (e.g. 600, 610, 620, 630, 640 nm) to determine the effect of using a narrower spectral range of data on BLT source recovery, so that only one variable is changed, rather than the two which are changed here (range and number of wavelengths).

4.3.2 Phantom Data Collection

A plastic mouse phantom (XPM2, Perkin Elmer, Fig. 4.3), with two internal light sources, was imaged using the BLDOT system.

Effect of Filter Bandwidth For the filter bandwidth study, data were collected at $\lambda^* =$ 600, 620 and 640 nm with 10 nm bandwidth filters (Thorlabs Inc.) and at $\lambda^* = 600$, 623 and 643 nm, where each filter had a different bandwidth: 22, 32 and 34 nm respectively (Semrock Inc.), the bandwidth of these filters is referred to as $\sim$20 nm. Tomographic reconstruction of this data was performed using the CSCG algorithm and both NBW and WBW Jacobians.

Three-dimensional surface capture data was taken of the phantom to enable mesh creation for use in free space modelling which was used to calibrate data, and tomographic reconstruction. The emission characteristics of the light sources within the XPM2 phantom have been previously characterised (Fig. 4.3) and the spectral optical properties experimentally determined [48, 197] and are accounted for in all BLT reconstructions.

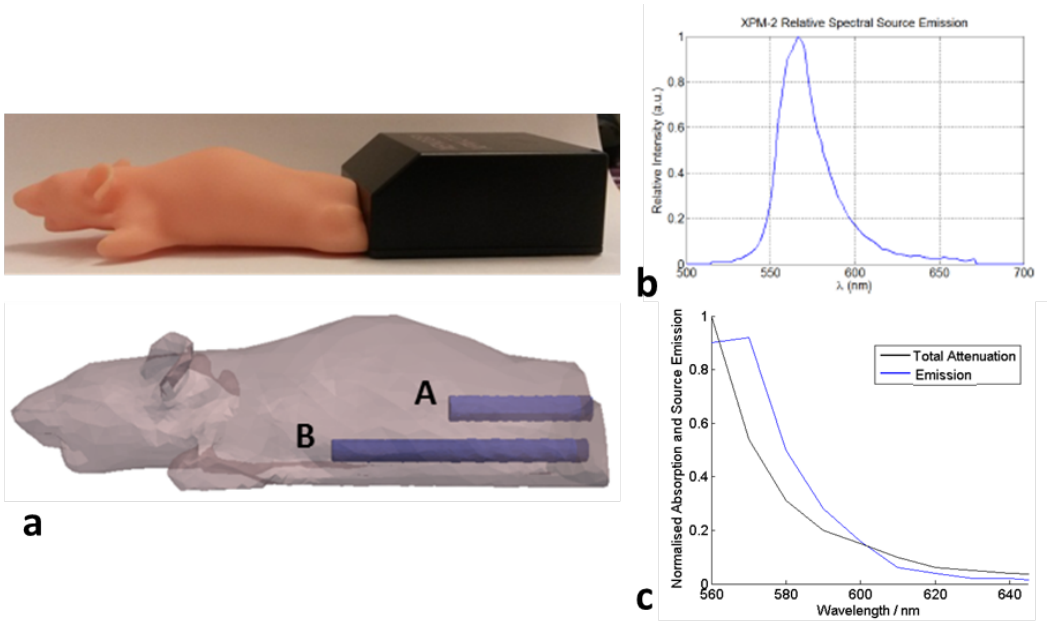

Figure 4.3: (a) XPM2 mouse shaped phantom. Position of the two sources (at the end of the internal rods) are indicated in the lower image, obtained from microCT data. Reproduced from ref. [96]. (b) Emission spectrum of the internal light sources of the XPM2 phantom. Reproduced from ref. [48]. (c) Emission spectrum and total attenuation of the phantom at discrete wavelengths.

Effect of Filter Selection In order to determine whether data can be collected at fewer wavelengths without compromising data quality, data were collected at $\lambda^* = 560$, 580, 590, 600, 620 and 640 nm with 10 nm bandwidth filters (Thorlabs Inc.). Tomographic reconstruction of this data was performed using the CSCG algorithm and the NBW Jacobian, using data at all six wavelengths (6wv) and three wavelengths only, $\lambda^* = 600$, 620 and 640 nm (3wv).

On consultation of the spectral attenuation and source emission of the phantom it is unclear which three measurement wavelengths are optimal to use for reconstruction (Fig. 4.3 c). With the simulation model, the peak source emission occurred when the attenuation was low (Fig. 4.2 a), so it was sensible to choose measurement wavelengths in this region of the spectrum. Considering the XPM2 attenuation and emission spectrum in the region 560 to 650 nm, the source emission is high when the attenuation is high and vice versa. So 600, 620 and 640 nm were chosen as the three wavelengths to use in BLT reconstruction since the attenuation is low at these wavelengths and also to be consistent with the simulation study.

4.4 Results: Effect of Filter Bandwidth on the Quantitative Accuracy of BLT

This section aims to determine whether increasing the bandwidth, and additionally including filter bandwidth modelling in the tomographic reconstruction algorithm, has an effect on the quantitative accuracy of the recovered source.

4.4.1 Simulation

Raw measurement data at a range of bandwidths (1, 10 and 20 nm) are shown in Fig. 4.4 a. The simulated surface intensity is greater for data simulated at larger bandwidths for a given exposure time, as expected due to the increase in total light transmitted through the

filter, arising from the larger number of transmitted wavelengths. The percentage variation (P) in maximum measured intensity at 10 and 20 nm bandwidths (I_{10nm} and I_{20nm}) relative to 1 nm bandwidth (I_{1nm}): $\mathrm{P} = 100 \times \frac{(\mathrm{I_{10nm}} - \mathrm{I_{1nm}})}{\mathrm{I_{1nm}}}$ (for 10 nm), shows the extent to which the signal varies (Table 4.2 *). The maximum variation is for 620 nm data in all cases, as the source emission is close to the peak intensity of fluc (612 nm, [25]) and the tissue attenuation is low (Fig. 4.2 a). Therefore, the intensity of all wavelengths transmitted through the filter is high, introducing a larger error when only the central filter wavelength is considered. The increase in measured intensity when using 10 and 20 nm filters suggests that a reduction in exposure time of the order of 17× and 58× for 10 and 20 nm filters respectively can be applied to obtain the same signal as when using a filter with 1 nm bandwidth.

Table 4.2: Percentage difference of total intensity (thresholded at 50% of maximum value) of boundary data between bandwidths of 10 and 20 nm and 1 nm to two significant figures. Shown for raw data (*) and data normalised by bandwidth (†).

Wavelength / nm	10 nm*	20 nm*	10 nm†	20 nm†
600	980	1800	7.8	-3.5
620	1700	5800	82	200
640	960	1900	5.6	-2.1

In the case of BLT, the target source and recovered sources for simulated data at bandwidths of 10 and 20 nm are shown in Fig. 4.5. Considering only the NBW model, which is currently used in BLT reconstructions, the reconstructed source distributions for the two bandwidths are qualitatively similar. The error in centre-of-mass (Fig. 4.6 a, black bars) of the reconstructed sources using the NBW model remained constant to within 0.2 mm over the range of bandwidths simulated. This small variation, and a low correlation (Table 4.3, '$\mathrm{r_{NBW}}$'), demonstrates a negligible dependence of centre-of-mass error on bandwidth. Some variation in the equivalent radius is observed (maximum variation, 0.77 mm, Fig. 4.6 b, black line). However this variation does not appear to have a strong dependence on bandwidth, supported by a Pearson's correlation coefficient of -0.47 (Table 4.3, '$\mathrm{r_{NBW}}$').

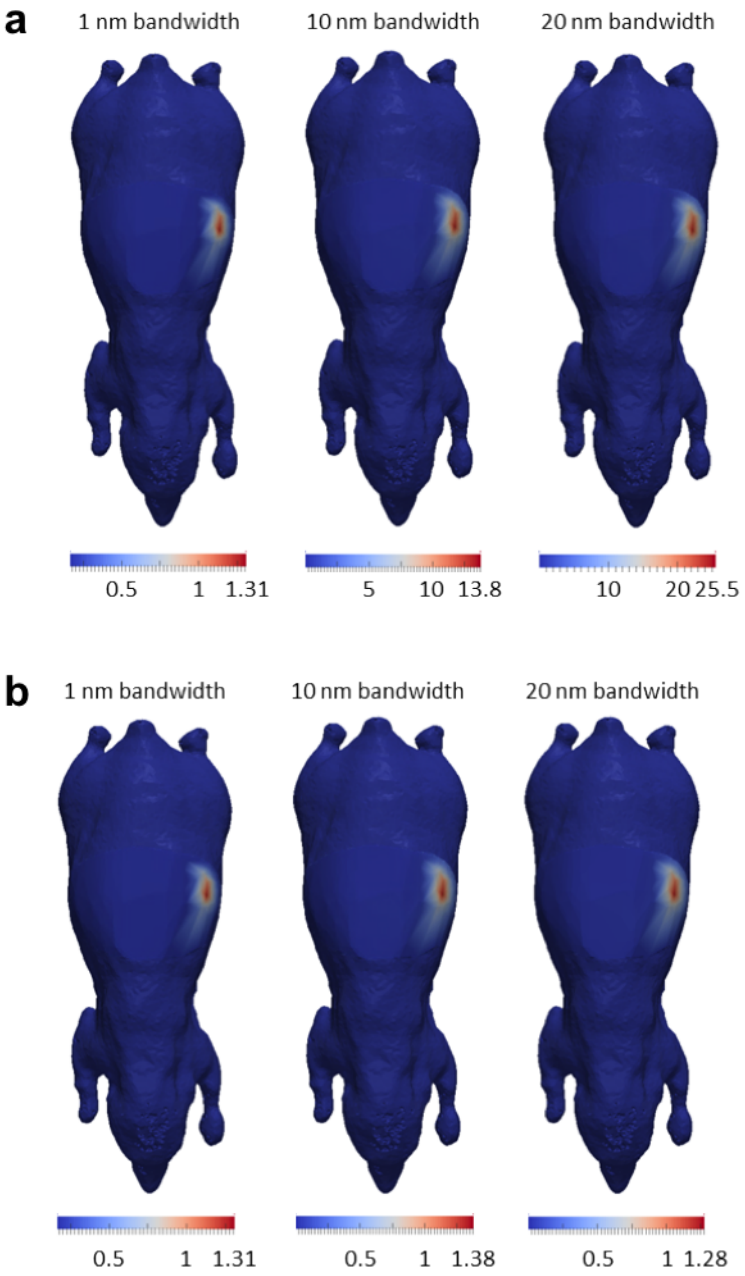

Figure 4.4: (a) Measurement data calculated at 600 nm at three bandwidths, thresholded at 12.5% for visualisation. The same distribution is seen but the intensity varies with bandwidth. (b) As (a) with data normalised by bandwidth. Colourbar units: arbitrary intensity units. Adapted from ref. [96].

These results suggest that bandwidth has qualitatively little effect on the recovered source size and position, for the range of bandwidths considered. The equivalent radius further demonstrates the observed similarity between the recovered sources at 10 and 20 nm bandwidths (Fig. 4.5), which have an 0.34 mm variation in equivalent radii.

Table 4.3: Pearson's correlation coefficient, r, to determine correlation between bandwidth and centre-of-mass, equivalent radius and total intensity of recovered sources using both NBW and WBW methods, and 'p' value from Wilcoxon signed rank test between NBW and WBW data.

	r_{NBW}	r_{WBW}	p
Centre-of-mass	0.39	0.30	0.47
Equivalent radius	-0.49	-0.87	0.47
Total intensity	0.99	-0.27	0.02

When considering the total recovered source intensity of NBW reconstructions at all bandwidths, a strong linear dependence on bandwidth is observed (Fig. 4.6 c, black line), and a strong positive correlation calculated (Table 4.3, 'r_{NBW}'). As bandwidth increases, the discrepancy between the total intensity of the target and reconstructed sources increases dramatically, resulting in the intensity of the source recovered using 20 nm bandwidth data being approximately 20× higher than that using 1 nm data. This is due to an increase in the model-data mismatch which occurs in the model-based image reconstruction algorithm when using the NBW model: at higher bandwidths it becomes less appropriate to approximate the data as being collected at the single, central wavelength of the filter. A strong dependence of the quantitative accuracy of the recovered source on filter bandwidth has been demonstrated and must be accounted for in the reconstruction.

A possible method to remove the intensity dependence is normalisation of the BLI measurement data by the bandwidth of the filters used for data collection, i.e. data taken using a filter with a bandwidth of 10 nm is divided by 10 etc.. This results in intensity distributions with similar maximum intensities at each bandwidth (Fig. 4.4 b). However, there is still some variation present which is believed to be due to this method not accounting for the spectral

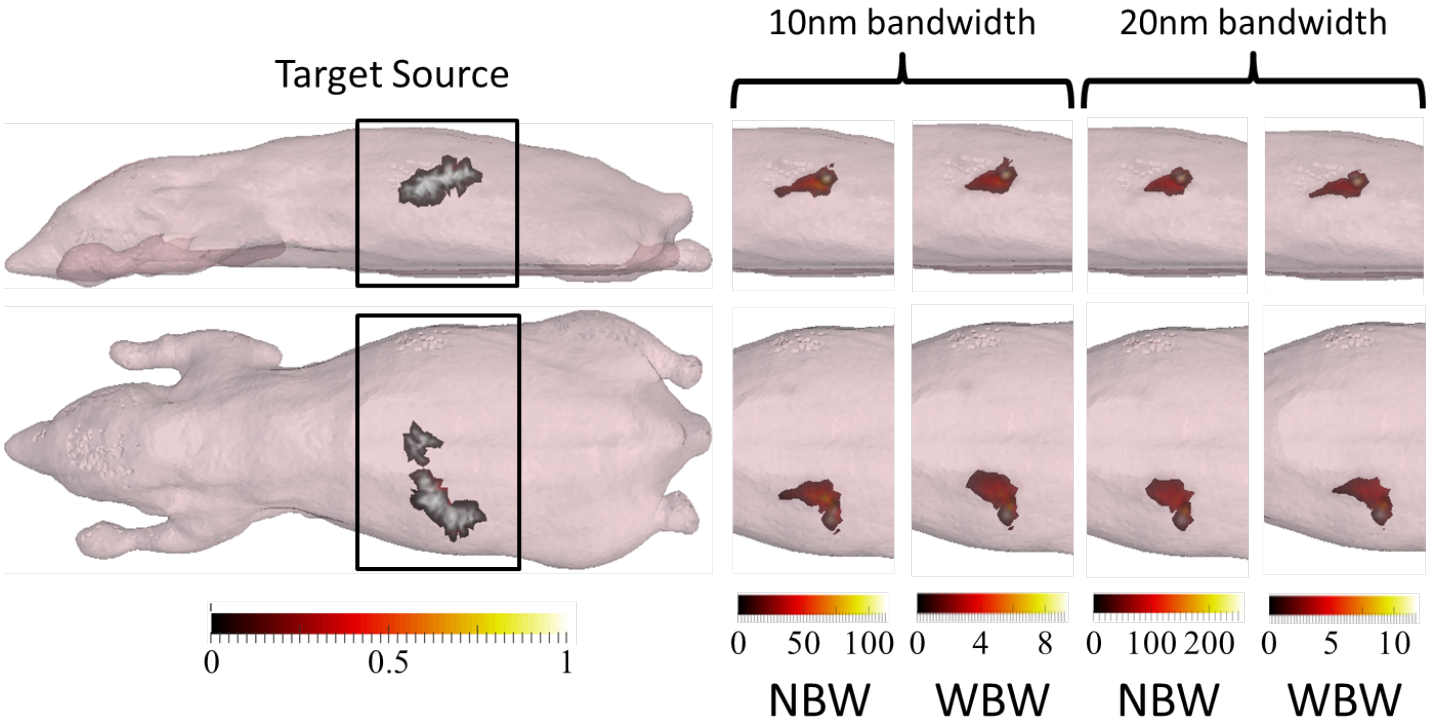

Figure 4.5: Side and top view of target and reconstructed bioluminescent sources. Reconstructions shown here were performed on data simulated with 10 and 20 nm bandwidth filters and using NBW and WBW Jacobians. The reconstructions are qualitatively similar for both Jacobian types and there is no effect of bandwidth on the appearance of the reconstructed source. Colourbar units: arbitrary intensity units. Reproduced from ref. [96].

tissue attenuation and source emission within the bandwidth of the filter. This variation is different for filters of different bandwidths due to differing spectral coverage of different filters (demonstrated in Fig. 4.2 b). If the measured intensity for different bandwidths is identical, $P = 0\%$ and the variation in measured bioluminescence intensity with bandwidth has been accounted for. However, following normalisation of this data by bandwidth, there still exists a variation in maximum intensity, P, of up to 82% for 10 nm data and 200% for 20 nm data (Table 4.2 †). Due to this large variation still present, normalisation is not considered to be an appropriate method of accounting for the bandwidth of the filters used. The WBW Jacobian method was devised as a method of accounting for filter bandwidth, and has been used to reconstruct the simulated data in this work.

4.4.1.1 Effect of Including Filter Bandwidth Modelling in the BLT Reconstruction

The sources recovered using both NBW and WBW Jacobians for bandwidths of 10 and 20 nm are shown in Fig. 4.5. The position and distribution of the sources recovered using both Jacobian types are qualitatively very similar, supported by the error in centre-of-mass, which varies by a maximum of 0.14 mm between the two Jacobian types (Fig. 4.6 a). There is a negligible correlation between centre-of-mass error and bandwidth (Table 4.3, 'r_{WBW}'), comparable to that for NBW reconstructions. The difference between the centre-of-mass errors for the two Jacobian types was not statistically significant (Table 4.3, 'p'), supporting qualitative observations and similar correlations with bandwidth.

The equivalent radius (Fig. 4.6 b) behaves similarly for both NBW and WBW reconstructions. There appears to be a moderate decrease with bandwidth for WBW reconstructions (Table 4.3, 'r_{WBW}') whereas the variation observed for NBW reconstructions is more random. However, the variation between equivalent radii for all bandwidths is submillimeter in both cases (0.77 and 0.51 mm for NBW and WBW reconstructions respectively) and there is no

significant difference between the two data sets (Table 4.3, 'p').

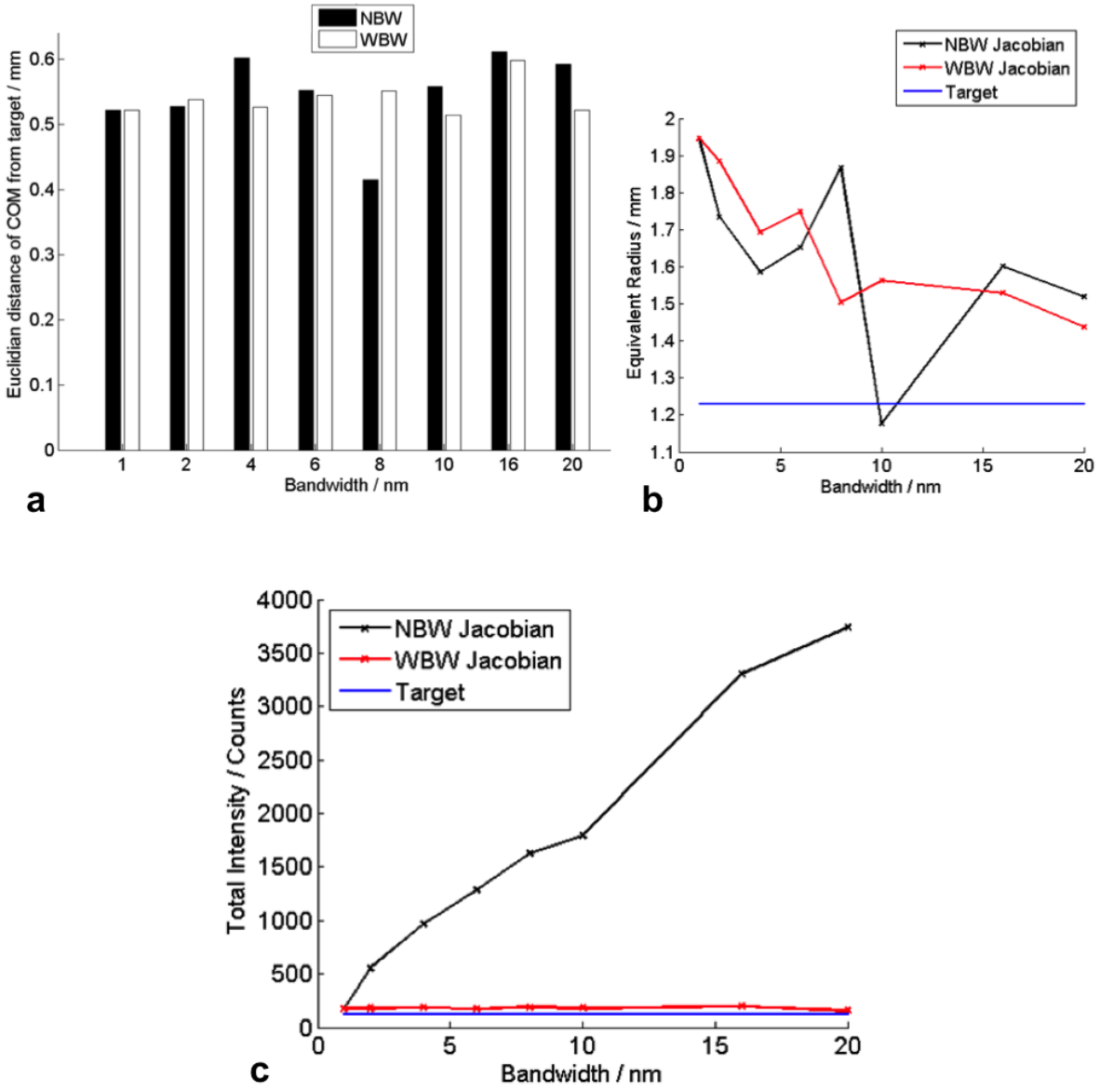

Figure 4.6: (a) Error in centre-of-mass (COM) of recovered sources as a function of bandwidth, for NBW (black bars) and WBW (white bars) reconstructions. There is negligible variation with both bandwidth and Jacobian type. (b) Equivalent radius of recovered sources for NBW (black line) and WBW (red line) reconstructions with the target value (1.23 mm) indicated. (c) Total intensity of recovered sources for NBW (black line) and WBW (red line) reconstructions, with the target value (124) shown. A linear dependence of intensity on bandwidth is observed for NBW reconstructions. This dependence is removed when using the WBW model, demonstrating the increased quantitative accuracy of WBW reconstructions. Adapted from ref. [96].

The similarity in appearance of the recovered sources using both Jacobian types (Fig. 4.5), combined with the lack of significant difference between NBW and WBW reconstructions in terms of size and position of the recovered source, suggests that there is no qualitative difference between sources recovered using the two Jacobian types.

The real advantage of using the WBW Jacobian model for image reconstruction is demonstrated when the total intensity of the recovered source is considered (Fig. 4.6 c). There is a significant difference between the recovered source intensity using the two Jacobian models (Table 4.3, 'p'). As described above, the total intensity of NBW reconstructions increases linearly as bandwidth is increased due to the model-data mismatch in the reconstruction algorithm becoming greater at larger bandwidths. This variation in intensity is removed by using the WBW model (Table 4.3, 'r_{WBW}'), demonstrating that the WBW model has improved the quantitative accuracy of BLT compared to that achievable using the traditional NBW model. The intensity of the source recovered from 20 nm bandwidth data is now 0.88× that of the 1 nm data (compared to approximately 20× for the NBW model), with the intensity of all reconstructions within 58% of the target value (as opposed to 2918% for the NBW model).

The time taken to perform the reconstruction using the WBW model increases with the bandwidth of the filter, as compared to the constant reconstruction time when using the NBW model. This increase in processing time is due to the nature of the WBW model, which calculates Jacobians at each wavelength transmitted through the band pass filter, governed by the bandwidth, and combines them, whereas the NBW model calculates one Jacobian only at the central filter wavelength regardless of the bandwidth of the filter. The computation time for NBW and WBW reconstructions at all bandwidths relative to the time taken to reconstruct data of a bandwidth of 1 nm is shown in Table 4.4. For reference, for a workstation running on 64-bit Windows (Windows 7 Enterprise) with 16 GB RAM, using an Intel® Core™ i7-3770 CPU at 3.40 GHz, using MATLAB R2013a, the NBW and WBW

reconstructions for 1 nm took around 2960 s. Although the processing time is increased, the increase in quantitative accuracy of the recovered sources demonstrated that using the WBW model has clear potential in enhancing the quantitative accuracy of BLT, advancing the technique towards implementation routinely in *in vivo* pre-clinical studies. The variation in reconstruction time for using the NBW model is unexpected, all reconstructions are calculating a single Jacobian matrix and therefore should all take equal time. The variation is thought to be due to variation in use of the computer that was used to run the reconstructions. It is possible that during some of the reconstructions, other processes were running in the background, limiting the processing power available and therefore increasing the time taken for source recovery.

Table 4.4: Reconstruction time for simulation data at all bandwidths relative to the time taken to reconstruct data of a bandwidth of 1 nm for both NBW and WBW Jacobian models. The increase in time to reconstruct wider bandwidth data using the WBW method is shown.

Bandwidth / nm	NBW	WBW
1	1	1
2	1.19	1.14
4	1.01	1.36
6	1.14	1.67
8	1.04	1.99
10	1.00	1.88
16	1.12	2.80
20	1.04	2.94

This simulation study has shown that the bandwidth of filters used for multi-spectral data collection for BLT must be accounted for in the reconstruction algorithm. The WBW model has been shown to effectively account for the bandwidth of the filters, increasing the quantitative accuracy of the recovered source compared to that achievable using the NBW model. The WBW model was also applied to phantom data taken with the BLDOT system using filters of two different bandwidths to determine the efficacy of the model when applied to experimental data.

4.4.2 Phantom Data

Sources recovered from experimental data of the XPM2 mouse-shaped phantom with two internal sources illuminated (Fig. 4.3), taken using 10 nm and wider (∼20 nm) bandwidth filters and using both NBW and WBW Jacobian models, are shown in Fig. 4.7. Little difference is observed in terms of position and appearance of the recovered source, when comparing both bandwidths and Jacobian models. This suggests qualitatively that the range of bandwidths used for data collection has no effect on the source reconstructions, as with simulation, and as the total imaging time is decreased from 10 minutes 45 seconds to 5 minutes 20 seconds (including 4 minutes for surface capture), it is experimentally advantageous to use wider bandwidth filters. This will enable the imaging throughput to be maximised whilst minimising distress to animals during *in vivo* imaging.

The error in centre-of-mass of the reconstructions (Table 4.5) is similar for both Jacobian models at both bandwidths. Note the larger error for source B, which is due to the greater depth of the source within the phantom as compared to source A (Fig. 4.3 a) and therefore the increased absorption and scatter of the signal from source B as it travels to the surface of the phantom, where it is detected. Additionally, as both source A and B are illuminated simultaneously and source A is more superficial than source B, the signal from source B at the surface is overwhelmed by that from source A. Therefore the measured signal from source B is lower than that from source A and more susceptible to measurement noise, so is more difficult to reconstruct to a high degree of quantitative accuracy.

The equivalent radius is also very similar for both NBW and WBW Jacobian models (Table 4.5). This, along with qualitative observations of the reconstructions, supports the findings of the simulations that in terms of the size and position of the recovered source, there are very few differences between reconstructions using data at different bandwidths when using either the NBW or WBW Jacobian model to reconstruct. However, as with the simulations, the real advantage of using the WBW Jacobian model is clear when the intensity

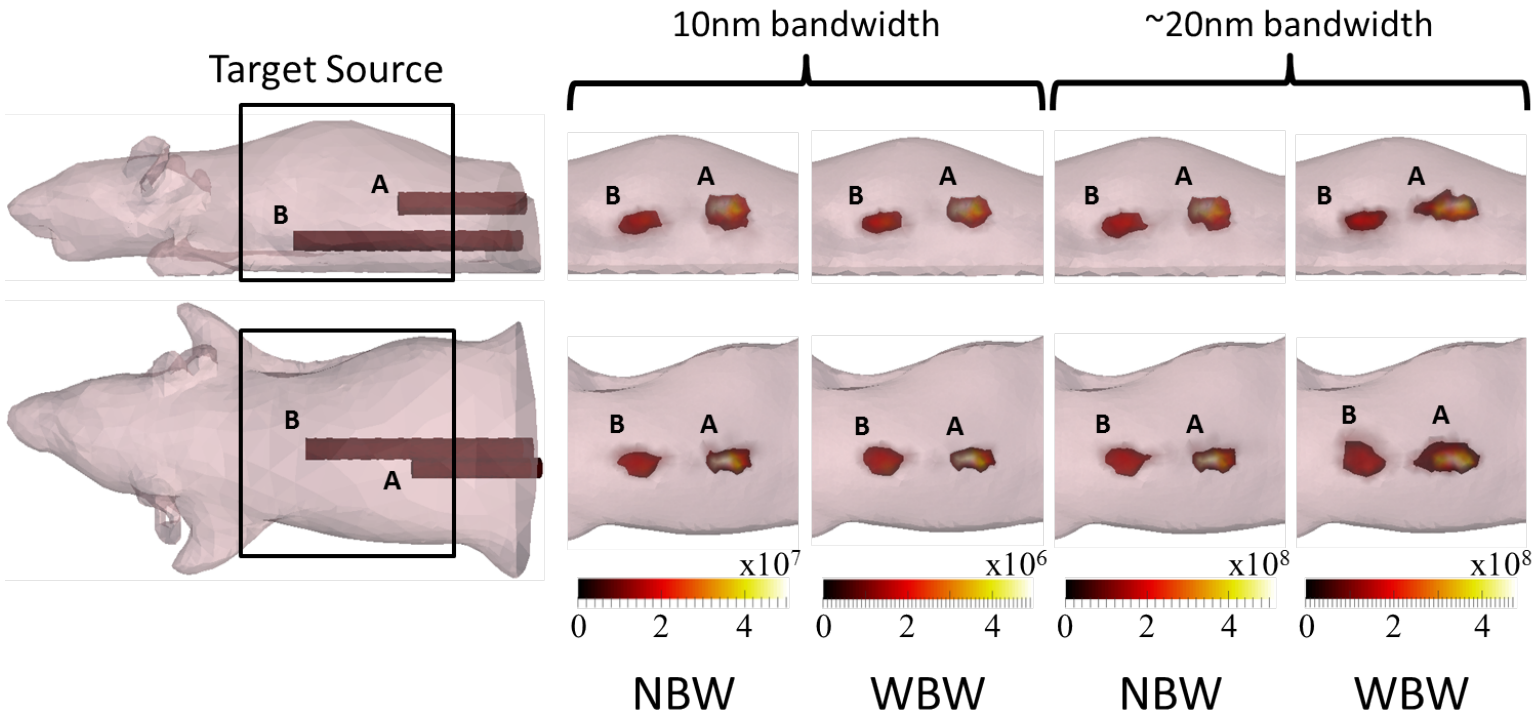

Figure 4.7: Target source locations for the XPM2 phantom (at the end of the rods shown in the images) and top and side views of XPM2 source reconstructions, thresholded at 20% of the maximum value, using the narrower (10 nm) and wider (∼20 nm) bandwidth filters and NBW and WBW Jacobians. Barely any difference is observed between the reconstructions with different bandwidth filters and the two Jacobian types. Colourbar units: arbitrary intensity units. Reproduced from ref. [96].

Table 4.5: Quantitative analysis of XPM2 source reconstructions of sources A and B. The larger bandwidth filters used for imaging are referred to as having a 20 nm bandwidth in this table, 'c-o-m error' is centre-of-mass error and 'ER' is equivalent radius.

Bandwidth / nm	Jacobian type	c-o-m error / mm		ER / mm		Total Intensity	
		A	B	A	B	A	B
10	NBW	1.62	3.58	0.65	1.60	4.89×10^8	2.88×10^8
20	NBW	1.71	3.63	0.65	1.53	2.33×10^9	1.44×10^9
10	WBW	1.59	3.84	0.42	1.47	4.25×10^7	2.50×10^7
20	WBW	2.03	4.28	1.13	1.89	6.20×10^7	3.79×10^7

of the recovered source is considered (Table 4.5).

Considering NBW reconstructions, the total recovered source intensity from data taken using ∼20 nm bandwidth filters is approximately 5× greater than that for 10 nm bandwidth data, for both sources A and B. As the same sources are being reconstructed in both cases, the recovered source intensity should be identical regardless of the bandwidth of the filters used for data collection. When the WBW model is used to reconstruct, the difference in intensity is decreased (Table 4.5). The total intensity of the recovered source from data taken using ∼20 nm bandwidth filters is just ∼1.5× that using 10 nm bandwidth data. Therefore the WBW model has accounted for the bandwidth of the filters to some extent, reducing the dependence of the intensity of the recovered sources on the bandwidth of the filters used for data collection. However, as with the simulation study, the increased number of Jacobians which are calculated in the WBW reconstruction (one for each wavelength which is transmitted through the filter, which are then added together to produce the full WBW Jacobian) results in an increase in the reconstruction time as compared to when using the NBW model, with data taken using wider bandwidth filters taking the longest to reconstruct.

The filter transmission profiles for the filters used for data collection in this section were assumed to be top hat profiles, as per manufacturer data. However, the profiles should be confirmed using a spectrometer rather than relying on the manufacturers data for use in WBW reconstruction, as any variation will affect the quantitative accuracy of the recovered

bioluminescent source distribution. Additionally, the transmission percentage was assumed to be equal between the different bandwidth filters, although this was not the case in practice. The transmission percentage for the 10 and ∼20 nm filters, from manufacturer data, are 50-60% and 90-100% respectively. It is possible that not accounting for these differences is the cause of the remaining variation in total recovered source intensity between the WBW reconstructions using data from the different bandwidth filters (intensity using ∼20 nm bandwidth data is ∼1.5× that using 10 nm bandwidth data). Although the true transmission profiles of the filters are not accounted for in this chapter, results from this first experiment are promising for the application of the WBW model *in vivo*.

Experimental results presented here support the simulation work: using the WBW Jacobian model to reconstruct increases the quantitative accuracy of the recovered sources in BLT. There is qualitatively little effect on the source reconstructions, in terms of centre-of-mass error and equivalent radius, but quantitatively, the difference between the total reconstructed intensity at different bandwidths is greatly reduced, albeit with an increase in reconstruction time. In future work the true transmission profile of the filters should be measured and accounted for in the WBW reconstruction.

4.5 Results: Effect of Filter Selection for Multi-Spectral Data Collection on the Quantitative Accuracy of BLT

This section aims to determine whether using fewer selected wavelengths for multi-spectral data collection for BLT (three, as used in Section 4.4, as opposed to five or six which are traditionally used in the BLDOT system) affects the quantitative accuracy of the recovered bioluminescent source.

4.5.1 Simulation

Figure 4.8 shows the recovered source after reconstruction with the CSCG algorithm using data at the three combinations of wavelengths: 5wv, 3wv_1 and 3wv_2. There is qualitatively negligible difference between the sources recovered using 5wv and 3wv_2, supporting the hypothesis that the lower wavelengths (560 and 580 nm) contribute negligibly to the reconstruction. The total measurement intensity of each of the measurement wavelengths is shown in Fig. 4.9 a, demonstrating the low intensity of the 560 and 580 nm data compared to the three higher wavelengths, supporting the hypothesis further. On comparison of the 5wv and 3wv_1 recovered sources, differences in appearance are observed. The 3wv_1 source appears more sparse and disjointed than the 5wv source, this is attributed to the lower intensity of the 3wv_1 data.

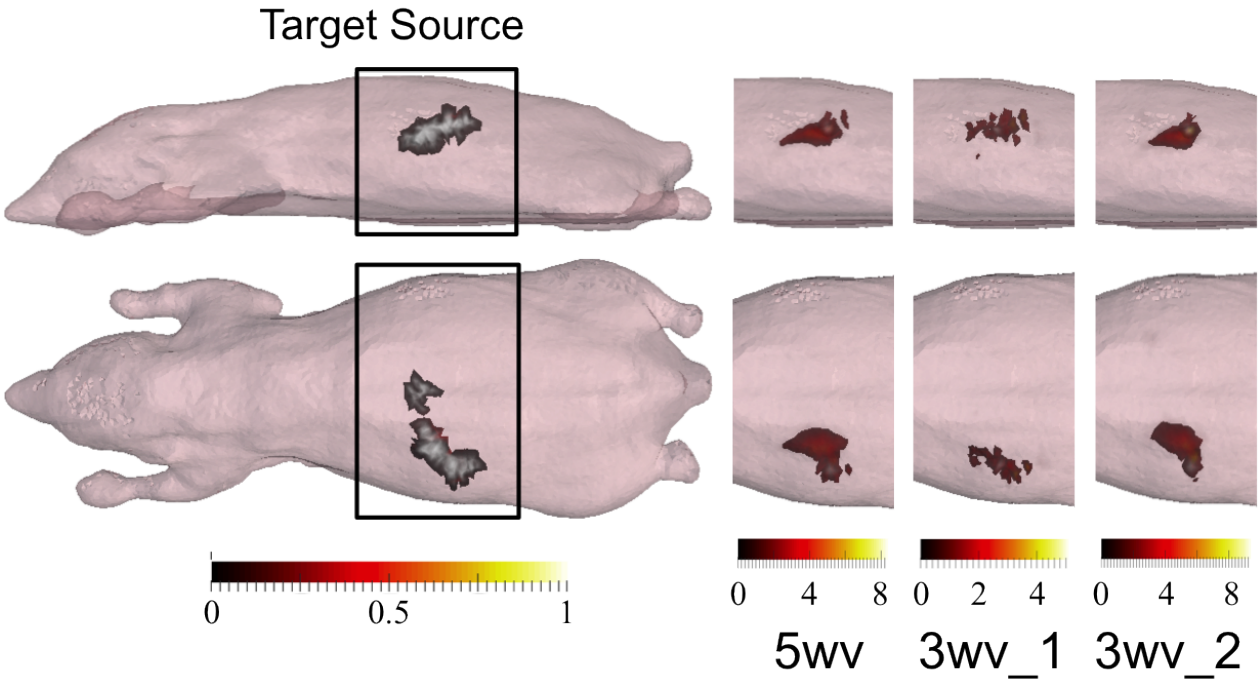

Figure 4.8: Target and recovered sources from data simulated at three different wavelength combinations: 5wv, 3wv_1 and 3wv_2 at a bandwidth of 10 nm. There is negligible qualitative difference between the sources recovered using 5wv and 3wv_2 and on consultation of the colourbar, the intensity of these reconstructions is quantitatively similar. Colourbar units: arbitrary intensity units.

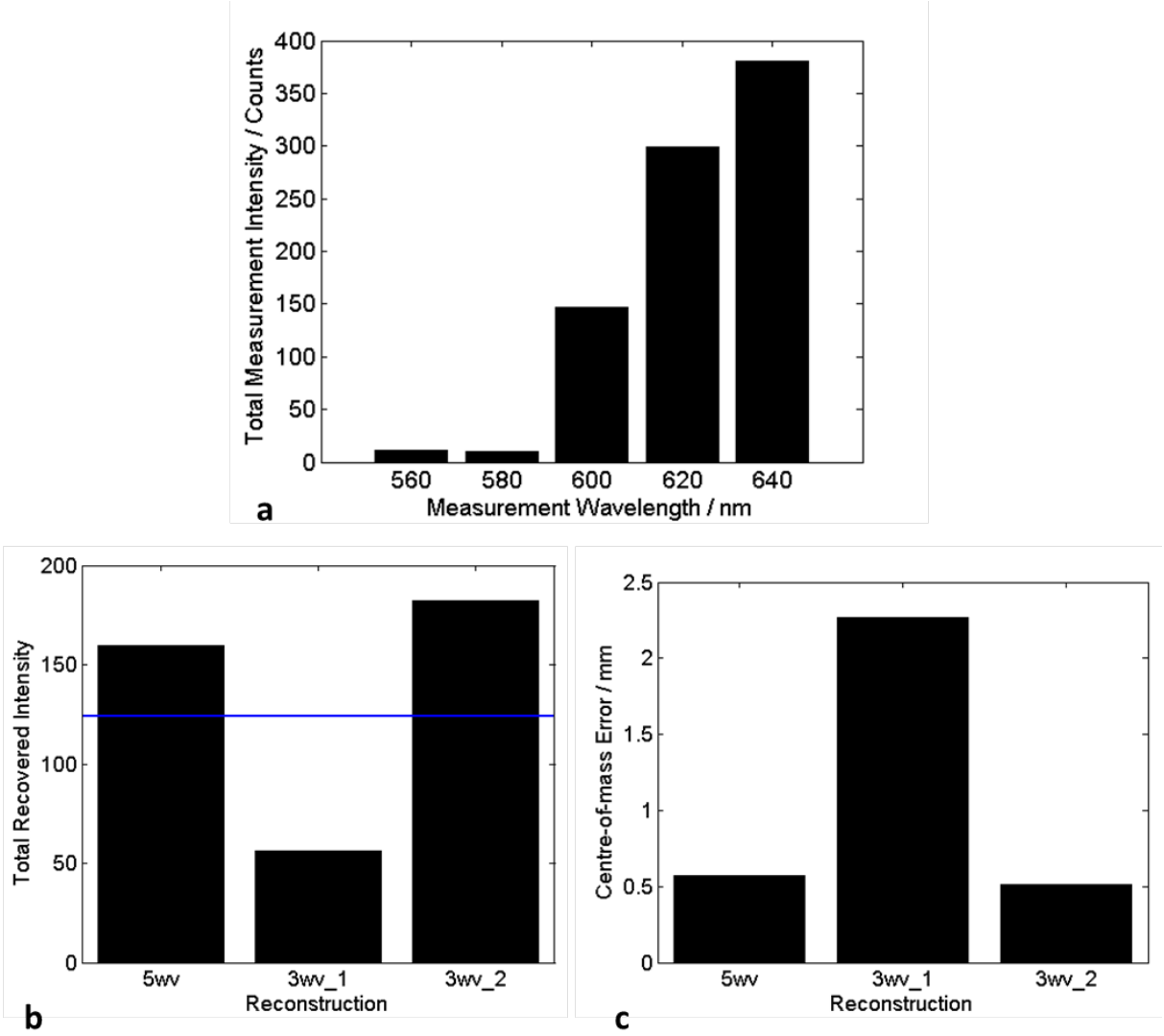

Figure 4.9: (a) Total intensity above a threshold of 50% of the maximum value of measurement data at a bandwidth of 10 nm; (b) Total recovered intensity, with target intensity indicated; (c) Error in centre-of-mass of recovered source, for reconstructions performed with 5wv, 3wv_1 and 3wv_2. In both (b) and (c) the 5wv and 3wv_2 recovered sources have comparable values.

Figure 4.9 b shows the total intensity of the recovered sources for each of the wavelength combinations. Note that only intensity above an empirically chosen threshold of 2% of the maximum was considered here. The recovered source intensity for 5wv and 3wv_2 data is very similar, with errors relative to the target value of 25% and 37% respectively. The 3wv_1

source has a much lower intensity, with an error of 57% relative to the target. The error in centre-of-mass of the recovered source (Euclidian distance between the centre-of-mass of the target and reconstructed sources) behaves in a similar way (Fig. 4.9 c), showing a much larger error for 3wv_1 compared to the other wavelength combinations which have positional errors of approximately 0.5 mm. The ability to recover sources with sub-millimetre accuracy using both 5wv and 3wv_2 shows that it is possible to recover an internal source to a high degree of quantitative accuracy using different wavelength combinations and, along with the similarity in intensity, demonstrates the similarity between 5wv and 3wv_2 reconstructions.

These simulation results show that it is possible to recover the internal bioluminescence distribution using fewer wavelengths without compromising quantitative accuracy, provided the wavelengths are sensibly chosen with consultation of the tissue attenuation and emission spectrum of the bioluminescent source. Although these results are promising, it is important to confirm these conclusions experimentally.

4.5.2 Phantom Data

Multi-spectral BLI data were taken using the XPM2 mouse-shaped phantom with two internal light sources illuminated, at six wavelengths using the BLDOT system. BLT reconstructions performed using the CSCG algorithm using data at all six wavelengths (6wv) and three wavelengths only (3wv: 600, 620, 640 nm) are shown in Fig. 4.10. Note that the NBW model was used for these reconstructions, this is due to the work being done prior to the development of the WBW model. It is thought that the conclusions drawn from this section using the NBW model are applicable to WBW source recovery, and due to the results presented in Section 4.4 which show the WBW model to improve the quantitative accuracy of BLT, the WBW model will be used in future experiments.

On visual inspection of the recovered sources, the 6wv sources appear more diffuse than the 3wv sources but they appear to be in a similar location. It is possible that the data

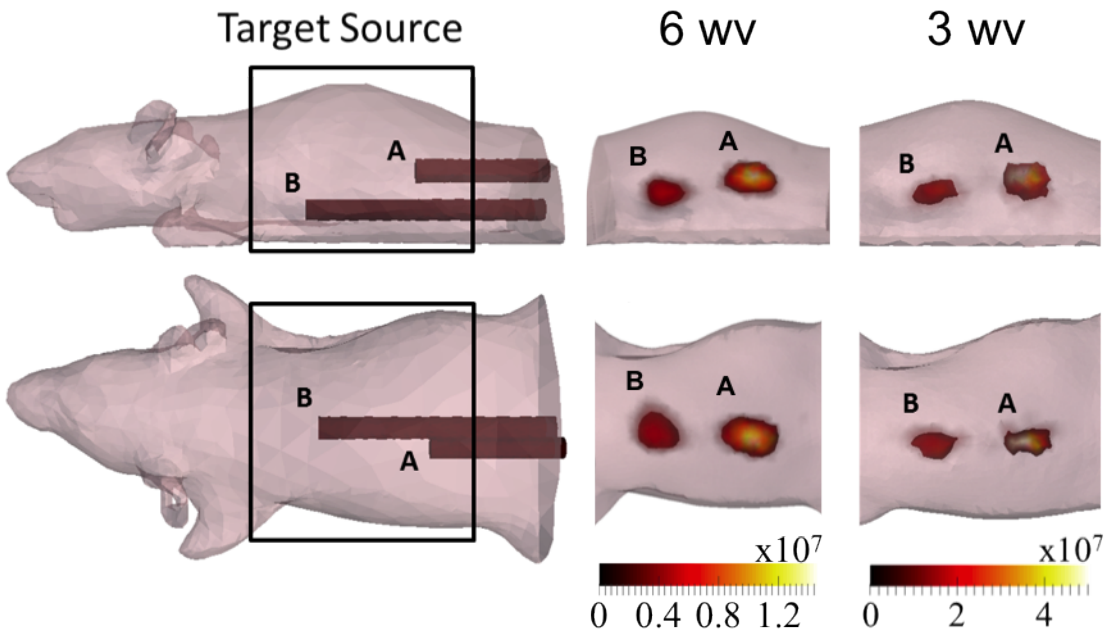

Figure 4.10: Target sources A and B (at the end of the rods pictured) and reconstructed sources for the XPM2 phantom, from data taken at 6 and 3 wavelengths (6 wv and 3 wv respectively). Qualitatively the sources recovered from data taken at three wavelengths appear smaller than those recovered from data at six wavelengths. The position of the sources from the two wavelength combinations appears similar. Colourbar units: arbitrary intensity units.

taken at 560, 580 and 590 nm, which is used in the 6wv reconstructions and not the 3wv reconstructions was noisy which introduced some error into the reconstructions, causing the source to be reconstructed more diffusely. This is speculation based on the high attenuation of the phantom at these wavelengths.

In order to perform quantitative comparisons between the 6wv and 3wv reconstructions the error in centre-of-mass, equivalent radius and intensity of source A relative to that of source B (above a threshold of 50 % of the maximum) were calculated for sources A and B. This data is shown in Table 4.6. The error in centre-of-mass of source A is less than that for source B for both wavelength combinations. This is due to the increased depth of the source within the phantom (Fig. 4.3 a) as explained in Section 4.4.2.

The error in centre-of-mass of source A recovered from 6wv is smaller than that for 3wv

Table 4.6: Quantitative analysis of XPM2 source reconstructions of sources A and B using data from 6 or 3 wavelengths to reconstruct. 'c-o-m error' is centre-of-mass error, 'ER' is equivalent radius and I_{AB} is the intensity of source A relative to B (from manufacturer data this is 96%).

#Wavelengths	c-o-m error / mm		ER / mm		I_{AB} / %
	A	B	A	B	
6	1.12	4.15	2.11	2.48	121
3	1.62	3.58	0.65	1.60	170

but the variation between the two is small (0.5 mm). The converse is found for source B, but the difference is submillimetre (0.57 mm). This is thought to be due to the balance between source emission and attenuation as explained before, it is possible that the data contribution from the three lower wavelengths is low as the attenuation is higher at these wavelengths. Therefore, these lower wavelengths will contribute low intensity, noisy data to the reconstruction which will decrease the quantitative accuracy compared to higher intensity data.

The equivalent radii of both sources A and B reconstructed with three wavelengths are smaller than the 6wv reconstructions (Table 4.6). Although the true size of the sources is unknown, the sources are LEDs located at the end of two tunnels within the phantom (Fig. 4.10) and so are expected to be small. This further supports that the data acquired from the three lower wavelengths is poor quality and is decreasing the quantitative accuracy of the reconstructions, suggesting that it is possible to use only three wavelengths to reconstruct without any loss of quantitative accuracy.

The intensity of source A relative to source B, from manufacturer data, should be 96%. However, in both cases source A has been recovered at a higher intensity than source B (Table 4.6). This is likely to be due to the higher position of source A in the phantom than source B, and so the signal from source B is affected as described earlier.

The reconstructions using 6wv and 3wv perform differently in each analysis metric chosen to evaluate the recovered source so it is difficult to conclude which reconstruction has per-

formed better. Data collection using all six wavelengths (10 nm bandwidth band pass filters) took a total of 29 minutes 20 seconds (including 4 minutes for surface capture), whereas the total data collection time for three wavelengths only was 11 minutes and 30 seconds. Due to these factors, the results presented here suggest that it is possible to use fewer wavelengths to reconstruct. In the future, if the wavelength choice is difficult, as it is here, it would be advisable to do initial controlled experiments (e.g. using a source with known size and intensity) at a number of different wavelength combinations to determine the appropriate wavelengths for data collection in the specific case. Additionally, as with the simulation study, both number of wavelengths and spectral range have been varied in this experiment. It is important to repeat this work to determine the effect of spectral range on the quantitative accuracy of BLT. For example comparing BLT source recovery using all six wavelengths (6wv) and six wavelengths which span a narrower spectral range (e.g. 600, 610, 620, 630, 635, 640 nm).

4.6 Conclusions

This chapter shows that the quantitative accuracy of BLT is affected by the bandwidth of the filters used in multi-spectral data collection. The WBW model was developed as a method of accounting for the bandwidth of the filters and has been shown to improve the quantitative accuracy of the recovered source intensity compared to the NBW model, which is traditionally used. The position and size of the recovered source was consistent between the two reconstruction types. In future work it is important to measure and account for the transmission profile of the filters when using the WBW model for bioluminescent source recovery, it is thought that this will improve the efficacy of the WBW model. Data has also been presented which shows that it is possible to take multi-spectral BLI data for use in BLT at fewer measurement wavelengths (three, as opposed to five or six) without a loss in quantitative accuracy. This is provided the wavelengths selected for data collection

are selected by consulting the spectral attenuation of tissue and the source emission, with optimum imaging wavelengths when the attenuation of tissue is low and the source emission is high.

Although the data presented here shows that it is possible to take data at fewer measurement wavelengths, both number of wavelengths and spectral range of measurement wavelengths were varied in this work. A further experiment should be performed to investigate the effect of spectral range of measurements on the quantitative accuracy of the recovered source in BLT, whilst keeping the number of measurement wavelengths constant. As mentioned in Section 4.3.1, data in the simulation study should be collected using 5 wavelengths in the range 600-640 nm and used in BLT source recovery. The recovered source can then be compared to that using the set of 5wv used in this c

hapter, which spanned 560-640 nm. It is thought that there will be minimal change in the recovered source due to the majority of the data collected at the wider spectral range coming from measurements taken at 600-640 nm. However, it is possible that using more measurement wavelengths in the range 600-640 nm will improve the quantitative accuracy of the recovered source. The quantitative accuracy can be tested, as it was in this Chapter, by comparing the recovered sources to the target source intensity and position. The effect of spectral range can also be tested using fewer measurement wavelengths, by using the 3wv_2 data presented in this chapter (which spanned 600-640 nm) and repeating the simulation using three measurement wavelengths in the range 560-640 nm. Further work should also include repetition of the experiment presented here such that statistical analysis can be performed on the resulting data, strengthening the work presented in this chapter. The data presented here is from a single experiment only and while there appears to be no loss in quantitative accuracy, it is important to determine this definitively.

If future experiments corroborate the data presented here, the ability to take data with wider bandwidth filters and at fewer wavelengths will decrease the data acquisition time.

Originally multi-spectral data collection in the BLDOT system was done at five or six wavelengths using band pass filters with a bandwidth of 10 nm. This resulted in an acquisition time of approximately 15 minutes when including surface capture ($\sim$4 minutes). By using three measurement wavelengths at a bandwidth of 10 nm the imaging time is reduced to $\sim$10 minutes. Increasing the bandwidth of the filters to $\sim$20 nm decreases the acquisition time further, to $\sim$5 minutes. So, with further confirmatory experiments, the work in this chapter suggests that the acquisition time for data collection in the BLDOT system can be reduced by a factor of 3 without any apparent loss in quantitative accuracy of BLT. During pre-clinical imaging this will enable imaging to be performed during the time window at which the maximum intensity of the bioluminescent reporter occurs (approximately 10-20 minutes for fluc [75]) whilst decreasing the total time the animal must be anaesthetised and maximising imaging throughput.

The BLT reconstructions performed in this chapter used models with ground truth optical properties in the simulation studies, and well characterised optical properties were available for the XPM2 phantom. However, in pre-clinical work the true underlying tissue attenuation of the animal will be unknown, and therefore quantitative BLT is a challenge. The following chapters aim to tackle this problem and work towards truly quantitative BLT. Additionally, the WBW Jacobian model is validated in a murine model in Chapter 6.

Chapter 5

Development and Validation of a Spectral Derivative DOT Method

The data presented in the previous chapters tackles some of the limitations to the quantitative accuracy of BLI, in overcoming the dependence of measured intensity on animal position (Chapter 3), and BLT, in accounting for the dependence of the recovered source intensity on filter bandwidth (Chapter 4). Thus far, the BLT reconstructions have been performed on simulation and phantom data which have well characterised optical properties. In pre-clinical imaging the tissue attenuation of the animal will be unknown. This chapter will begin by demonstrating the importance of using accurate optical properties in the BLT reconstruction. A spectral derivative (SD) DOT reconstruction method is then proposed as a way of obtaining accurate optical properties for animals imaged using the non-contact BLDOT system, and validated by applying the method to data simulated using the Digimouse atlas. Finally BLT is simulated using the Digimouse atlas, with a view to demonstrating that BLT using optical properties obtained from SD DOT has superior quantitative accuracy to other estimates of the optical properties. Some of the work presented here was presented at the OSA Biomedical Optics Congress 2016 and can be found in ref. [198].

5.1 The Importance of using Accurate Optical Properties in BLT Source Recovery

As an initial demonstration of the importance of the optical properties used in BLT reconstructions, BLT was performed on data taken from a *post mortem* mouse with an artificial light source (tritium-based, Trigalight Orange III; mb-microtec, Switzerland) inserted at a depth of approximately 2 mm using the method detailed in Section 3.2 (Fig. 3.2). Data were taken at 600, 623 and 643 nm using the BLDOT system and the CSCG algorithm was used to reconstruct the internal bioluminescent source distribution [50]. Four different sets of optical properties, all homogeneous, with varying total haemoglobin concentration, [HbT], were assumed in the reconstruction (Table 5.1).

Table 5.1: Tissue composition parameters (total haemoglobin concentration, [HbT] / mM, and tissue oxygen saturation, StO_2 / %) used in BLT reconstructions for an animal with an artificial light source inserted at a depth of approximately 2 mm, and the depth of the source recovered using these tissue properties. Properties 'a' are 'muscle' optical properties from the Digimouse atlas, properties b-d are calculated by reducing [HbT] for 'a' by 25%, 50% and 75% respectively.

	[HbT] / mM	StO_2/ %	Depth / mm
a	0.070	80	1.69
b	0.053	80	2.30
c	0.035	80	3.62
d	0.018	80	6.24

The appearance of the recovered source has a dependence on the assumed optical properties (Fig. 5.1), as does the position (Table 5.1, 'Depth'). The depth of the recovered source was calculated by determining the Euclidian distance of the centre-of-mass of the recovered source from the surface of the animal. A four-fold increase in the depth of the recovered source with a four-fold decrease in HbT concentration (which corresponds to a decrease in tissue attenuation) was found (Table 5.1). Reconstructions **a** and **b** achieve a source depth close to the target depth of 2 mm, suggesting these estimates of tissue attenuation are closest to the

true values, supported by the appearance of the recovered source which is more compact for **a** and **b** (Fig. 5.1). However, these are only estimates, the true attenuation of the animal is unknown. The variation in the recovered sources, in terms of appearance and position, demonstrates the importance of having accurate knowledge of underlying tissue attenuation in order to perform quantitative BLT. However, these reconstructions assume homogeneous tissue attenuation, which is incorrect, the heterogeneity of the underlying anatomy of animals must also be accounted for in order to perform quantitative BLT [29, 30].

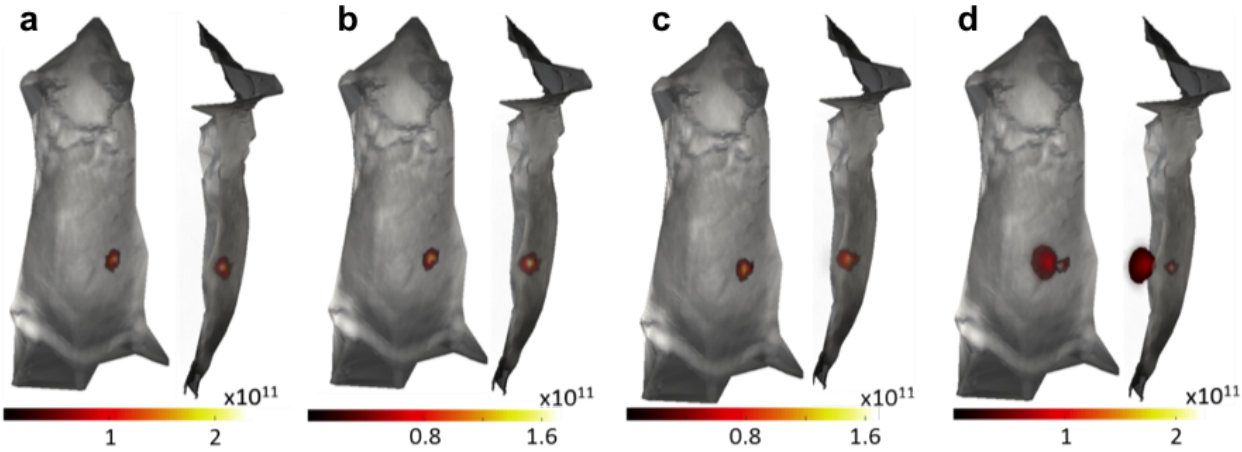

Figure 5.1: BLT data for a mouse with an artificial light source inserted at an approximate depth of 2 mm assuming different total haemoglobin concentrations, decreasing from (a)-(d) (see Table 5.1). Colourbar units: arbitrary intensity units. Reproduced from ref. [198].

The Digimouse atlas, used in previous chapters, incorporates the heterogeneity of the underlying anatomy of the mouse. The model of mouse anatomy was acquired from coregistered microCT and cryosection images of a male nude mouse [42], and is shown in Fig. 4.1. The model is split into different regions, encompassing the organs of the animal, in this case there are 8 regions which all have different optical properties. The optical properties of this model have been calculated using appropriate extinction coefficients (http://omlc.org/spectra/) [149, 199]. The variation between the optical properties in each region is up to 91× when considering HbT concentration and 6× when considering water content (see Table 4.1). It

is therefore important to consider this heterogeneity in anatomy and chromophore content when performing quantitative BLT. One method of doing this would be to use the heterogeneous optical properties of a mouse atlas to reconstruct murine BLT data [41]. This will produce more accurate reconstructions than assuming homogeneous tissue, but the chromophore concentrations in this model are fixed and in reality these will vary from animal-to-animal limiting the achievable quantitative accuracy.

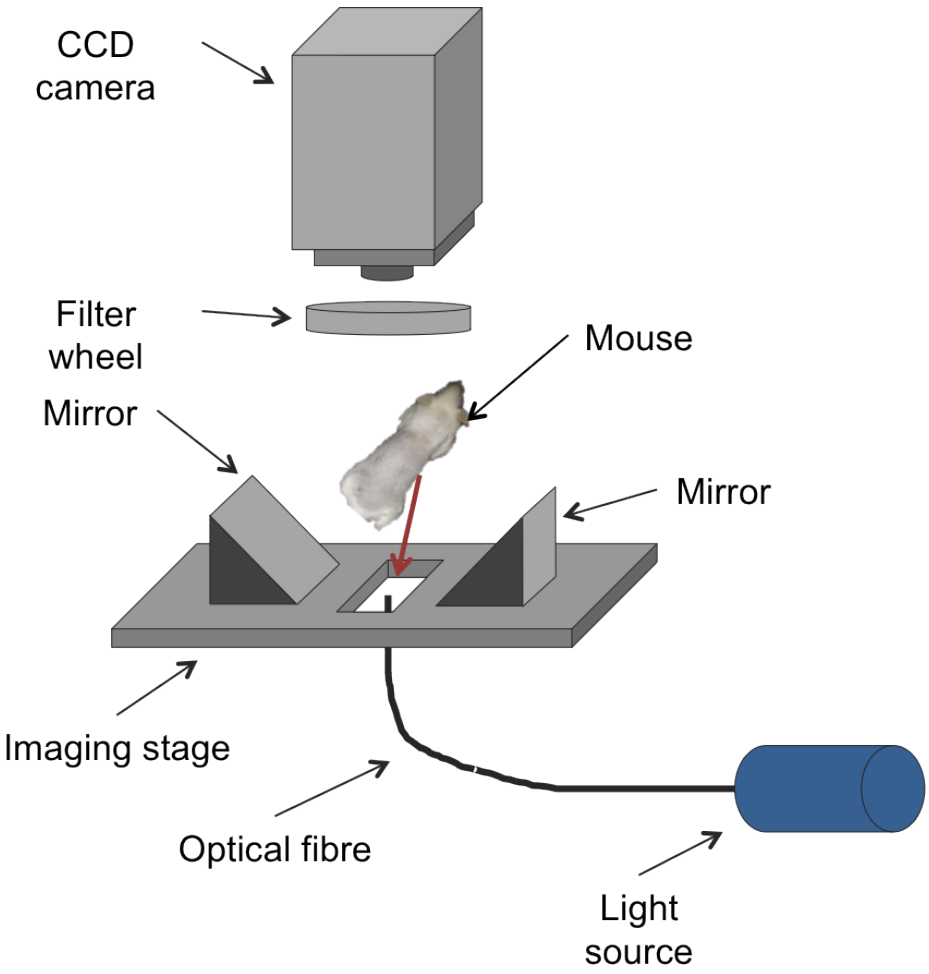

Figure 5.2: Schematic of the imaging set up for collection of trans-illumination images to monitor the change in attenuation with time after death of an animal, which is being used to represent the change in oxygenation of tissue. The animal is placed on the imaging platform in the BLDOT system with the optical fibre positioned below the abdomen and data collected at 643 nm.

To demonstrate the heterogeneity of underlying tissue attenuation, and variation with oxygen saturation and between animals, images of light transmitted through two mice (*post mortem*) from a single point trans-illumination source were taken using the BLDOT system, over 35 minutes at 643 nm (a schematic of the imaging set up is shown in Fig. 5.2). Resulting transillumination images of the two animals are shown in Fig. 5.3. The sources were placed in different locations for the two animals, one placed under the lower abdomen (Fig. 5.3 a) and one under the upper abdomen (Fig. 5.3 b). Imaging commenced between 5 and 10 minutes after sacrifice, following shaving of the animal. In the data analysis here the assumption has been made that the time after death is inversely proportional to the tissue oxygen saturation of the animals.

The intensity in four different 2 mm^2 regions of interest (ROIs) across each animal was plotted (Fig. 5.3 b and d). The ROIs were chosen by taking the highest intensity region on each side of the spine (ROI1 and ROI2) and then choosing an arbitrary location within the transmitted signal on each side of the animal for ROIs 3 and 4. The intensity varies with both time, and therefore oxygen saturation, and position, with all eight ROIs for the two animals varying differently. The maximum variation in intensity over time is 7% and 35% for the animals with the light source under the upper and lower abdomen respectively. Although the variation for most of the ROIs is $<$10% (with a particularly small variation of $<$7% for the animal with light source under the upper abdomen, Fig. 5.3 d) this data demonstrates that there is a variation present which is different for different regions of the animal. At 643 nm the attenuation of deoxyHb is greater than that of HbO (Fig. 1.3 a) so as tissue oxygenation decreases the total attenuation will increase and the transmitted intensity will decrease. This is true for constant blood volume. However, prior to death the blood is circulating around the animal and so when the heart stops beating the blood will likely collect in different organs within the body. So a decrease in intensity could also correspond to an increase in blood volume within the ROI, and an increase in intensity suggests that the

volume of blood in that region is decreasing. The intensity of all ROIs for the animal with the light source underneath the lower abdomen (Fig. 5.3 a) and ROIs 2 and 4 for the animal with the light source under the upper abdomen (Fig. 5.3 c) are decreasing. However, ROIs 1 and 3 in the upper abdomen have increasing intensity (maximum variation of 6% and 4% respectively). These regions correspond with the position of the liver [42] and may suggest

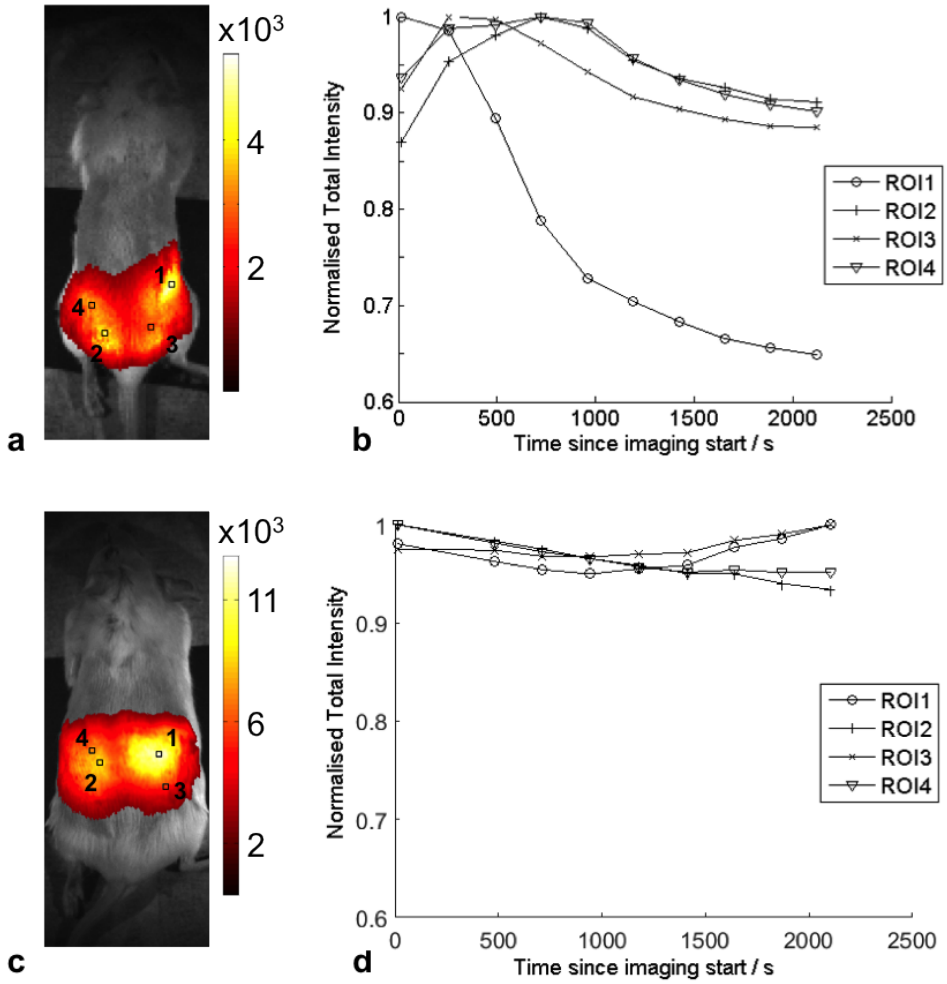

Figure 5.3: (a) and (c) transillumination images from a single point source of two different mice, measured at 643 nm. Four regions of interest (area 2 mm^2) are indicated. Colourbar units: counts s^{-1} on CCD. (b) and (d) variation of the total measured intensity in the four ROIs over the time course of the experiment, demonstrating the heterogeneity of the underlying tissue attenuation. Adapted from [198].

that the blood volume within the liver is decreasing with time after death. These results show how it is difficult to produce an accurate estimate of tissue attenuation as the chromophore distribution is highly heterogeneous with each region of the animal varying differently.

As shown in Fig. 5.1 it is important to have accurate optical properties for use in BLT reconstructions, so the aim of this work is to use DOT to obtain subject-specific optical properties for use in BLT reconstructions. The following sections introduce a SD DOT reconstruction algorithm for application to the non-contact BLDOT imaging system (and all non-contact DOT imaging systems) and validation of this algorithm through simulation using the Digimouse atlas.

5.2 Spectral Derivative DOT

Previous work has shown a SD approach to DOT reconstruction to improve the quantitative accuracy of the recovered chromophore distribution and remove uncertainty ('noise') based on fibre-surface coupling efficiency and boundary variations when using a contact DOT system for data collection [200, 201]. A SD approach in application to data taken using the non-contact BLDOT system is described in this chapter. Simulations are performed on the Digimouse atlas to assess the efficacy of the SD method in removing the angular dependence of the signal measured at the CCD, a dependence accounted for currently using the free space model, with an aim of negating the need to perform free space modelling on DOT data which will decrease the data processing and reconstruction time.

Additionally, the traditional spectral DOT reconstruction (Section 2.4.2), referred to here as 'normal spectral' or NS, requires data calibration as detailed in Chapter 6 of ref. [194]. This is a complicated process to calibrate data, account for system offsets and obtain an initial estimate of the optical properties of the imaging subject to use in the reconstruction. The SD method is proposed as a method which does not require the initial data calibration

step to produce accurate attenuation maps of the imaging subject. If the data calibration step is not performed, a method of producing an initial optical property estimate for use in the full reconstruction is required. A SD region based (SDR) reconstruction method is proposed to provide this data, which performs chromophore recovery using experimental data assuming a homogeneous volume.

5.2.1 Theory

The SD approach uses spectral difference data rather than absolute calibrated measurements at each wavelength. For simplicity, only deoxyHb, HbO and water concentrations are reconstructed for, scatter parameters are not considered in the reconstructions presented here but should be included in future work. This will limit the quantitative accuracy of the recovered chromophore distribution, but to validate the method using the Digimouse atlas it is assumed that the scatter parameters are that of 'adipose' tissue which is known to occupy the bulk of the model (Fig. 4.1) and is therefore considered to be a good approximation. The imaging process and collected data are identical to when using the NS method, however differences are present in the Jacobian calculation and measured data preparation processes.

To construct the SD reconstruction the terms in the NS update equation (Eq. 2.16 $\left(J^T J + \tilde{\zeta} I\right)^{-1} J^T \delta\Phi = \delta\mu$) must be modified, J is now the spectral difference Jacobian and Φ is the spectral difference data. Assuming three measurement wavelengths, the spectral difference data can be calculated from measured data (Φ_{λ_1}, Φ_{λ_2}, Φ_{λ_3}) using the equation:

$$\Phi_{SD} = [\Phi_{\lambda_1} - \Phi_{\lambda_2},\ \Phi_{\lambda_2} - \Phi_{\lambda_3}] \tag{5.1}$$

Similarly the SD Jacobian can be calculated from the traditional NS Jacobian by calculating the difference between equivalent entries for two adjacent wavelengths, i.e. for equivalent node and detector combinations. The structure of the NS and SD Jacobians are shown in

Fig. 5.4 a and b respectively.

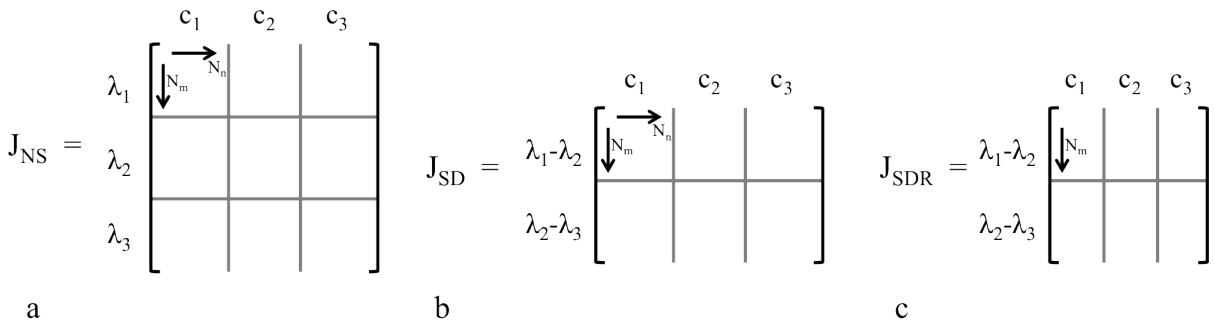

Figure 5.4: Structure of the (a) normal spectral, NS, (b) spectral derivative, SD, and (c) spectral derivative region reconstruction, SDR, Jacobians for data at three wavelengths, λ_i, and assuming three chromophores, c_i. N_m is the number of measurements and N_n is number of nodes. The SDR Jacobian has one chromophore concentration per wavelength combination as the volume is considered to be homogeneous.

As was shown in previous work on the SD method, the noise in the data can be accounted for using this method [200, 201]. The noise in data in previous work based on a contact imaging system was due to the fibre-surface coupling and boundary variations of the imaging subject. These effects were assumed to be constant for adjacent wavelengths when considering wavelengths 2 nm apart, with the efficacy of the SD method showing the assumption to be accurate [200]. Further simulation studies also showed the SD method to be effective when using data with 20 nm spacing between measurement wavelengths [201]. This work aims to show that the SD method can be applied to non-contact data from the BLDOT system. Similar assumptions will be made, that the noise in the data measured at the CCD is constant at adjacent measurement wavelengths. The noise considered here is the angular dependence of the measured data and the effect of apertures and lenses that the light passes through before being incident on the CCD, both of which are geometric (wavelength-independent) errors accounted for by the free space model [27], and any noise in the detection system which is also wavelength-independent [48]. It is assumed that the noise contributions will remain constant between measurements conducted under the same experimental conditions.

In contrast to the large number of wavelengths, with small spectral spacing, used for data collection in previous experimental work with the SD method [200], DOT data collected using the BLDOT system will be collected at only three wavelengths: 643, 720 and 850 nm. However, the SD method has been shown to be effective for a 20 nm spacing through simulation [201], suggesting that the efficacy of the model can translate to larger spectral spacings.

5.2.1.1 Mathematical Basis of the Spectral Derivative Method

The Jacobian at each wavelength is defined as the change in log amplitude (ignoring phase information which is not present in this continuous wave system, $\Phi = \ln(I')$, where I' is the amplitude [intensity] of the data) of each measurement at wavelength λ_i, $ln\left(I'_{\lambda_i}\right)$, due to a small change in the chromophore concentration, c [35]:

$$J_{\lambda_i} = \frac{\partial ln\left(I'_{\lambda_i}\right)}{\partial c} \tag{5.2}$$

But as described above, the measured data at each wavelength is subject to noise, n_{λ_i}, and therefore $I'_{\lambda_i} = n_{\lambda_i} I_{\lambda_i}$. Incorporating this into Eq. 5.2:

$$J_{\lambda_i} = \frac{\partial ln\left(n_{\lambda_i} I_{\lambda_i}\right)}{\partial c} \tag{5.3}$$

and using this relationship to calculate the spectral difference Jacobian gives:

$$J_{\lambda_i} - J_{\lambda_{i+1}} = \frac{\partial ln\left(n_{\lambda_i} I_{\lambda_i}\right)}{\partial c} - \frac{\partial ln\left(n_{\lambda_{i+1}} I_{\lambda_{i+1}}\right)}{\partial c} \tag{5.4}$$

simplifying:

$$J_{\lambda_i} - J_{\lambda_{i+1}} = \frac{\partial}{\partial c}\left[ln\left(n_{\lambda_i} I_{\lambda_i}\right) - ln\left(n_{\lambda_{i+1}} I_{\lambda_{i+1}}\right)\right] \tag{5.5}$$

$$J_{\lambda_i} - J_{\lambda_{i+1}} = \frac{\partial}{\partial c} ln \left(\frac{n_{\lambda_i} I_{\lambda_i}}{n_{\lambda_{i+1}} I_{\lambda_{i+1}}} \right) \tag{5.6}$$

Using the assumption that the noise in the data is constant at adjacent wavelengths ($n_{\lambda_i} = n_{\lambda_{i+1}}$):

$$J_{\lambda_i} - J_{\lambda_{i+1}} = \frac{\partial}{\partial c} ln \left(\frac{I_{\lambda_i}}{I_{\lambda_{i+1}}} \right) \tag{5.7}$$

Theoretically, now the data used for DOT reconstruction is noise-free under the assumptions stated above. The difference Jacobians are then concatenated together to produce the SD Jacobian, J_{SD} (Fig. 5.4 b). Which is used to solve Eq. 2.16.

As mentioned above, the data calibration method required for the NS reconstruction produces an initial estimate of the optical properties of the imaging subject for the full DOT reconstruction, as well as accounting for system offsets in the data. Due to the hypothesis that when using the SD method the data calibration step will not be required, a method of acquiring an initial estimate of optical properties is required. The method proposed is a region based reconstruction method, detailed below.

5.2.1.2 Region-Based Reconstruction for Initial Global Estimates of Chromophore Concentration

The region reconstruction method treats the whole imaged volume as homogeneous and follows the DOT reconstruction process detailed in Section 2.4.2. This process does still require an initial estimate of the optical properties so is not an ideal process to replace the data calibration procedure. However, the data calibration procedure is unable to deal with spectral data and currently only provides estimates of μ_a and μ_s' [194]. For the purposes of producing an initial estimate of chromophore concentrations when given initial values which are of the order of those present in tissue (chosen by consulting Digimouse values Table 4.1),

the region based method is considered to be adequate in determining the capability of the SD method in this initial study. The initial estimate of the optical properties used in this work is 0.1 mM, 0.1 mM and 50% for HbO, deoxyHb and water respectively.

Both NS and SD region-based reconstruction methods (NSR and SDR respectively) are applied to the data presented here. The SDR Jacobian, J_{SDR}, is calculated by calculating the difference between the NSR Jacobian entries at sequential wavelengths, in the same way as the full Jacobian. The structure of the SDR Jacobian is shown in Fig. 5.4 c. As can be seen, the dimensions of the Jacobian are $N_m \times 1$ (for each wavelength combination and chromophore). All the sensitivity values calculated for each node in the whole mesh, which is considered as a single region, are summed to determine a single sensitivity value. This value is then applied to the whole mesh for each wavelength and each chromophore [202]. This gives a global, homogeneous starting point for the full SD reconstruction calculated from true measurement data.

To validate the efficacy of the SD method in enabling data calibration (required during NS reconstruction) and free space modelling to be removed from the data analysis process of DOT, the reconstruction technique was applied to data simulated using a three-dimensional heterogeneous mouse model (the Digimouse atlas [42]).

5.2.2 Methods

5.2.2.1 Forward Data Calculation

Data were simulated using the Digimouse atlas with 15 sources positioned on the underside of the model underneath the abdomen in a 3×5 grid with 4 mm spacing, and 63 detectors placed evenly across the surface of the mesh, the areas occupied by the sources and detectors are shown in Fig. 5.5 b. The source positions chosen were true source positions from the BLDOT system (these will be detailed in Chapter 6). Three versions of Digimouse were used:

1. Simple_2, which had homogeneous 'adipose' bulk optical properties with a spherical anomaly of radius 4 mm in the abdomen with 2× HbT concentration of the bulk properties (Table 5.2);

2. Simple_200 - as simple_2 but with 200× HbT concentration in the anomaly (Fig. 5.5 a, Table 5.2);

3. True heterogeneous Digimouse atlas (Fig. 4.1, Table 5.3).

Boundary data were simulated at 643, 720 and 850 nm using the NIRFAST forward model (Section 2.2). These wavelengths are the same as the wavelengths which will be used for data collection in the BLDOT system, however the bandwidth of the filters has not been considered here.

Table 5.2: Tissue composition of the simple Digimouse models. The bulk properties of both the simple_2 and simple_200 models are the same but the spherical anomalies (anom) have different compositions, as indicated here.

Model	Tissue	[HbT] / mM	[StO_2] / %	[H_2O] / %	sa	sp
Simple	bulk	0.0033	70	50	0.98	0.53
Simple_2	anom	0.0066	70	50	0.98	0.53
Simple_200	anom	6.6	70	50	0.98	0.53

Table 5.3: Tissue properties of the heterogeneous mouse mesh. [HbT] - total haemoglobin concentration, [StO_2] - oxygen saturation, [H_2O] - water concentration, sa - scatter amplitude, sp - scatter power. Adapted from ref. [149].

Region	Tissue	[HbT] / mM	[StO_2] / %	[H_2O] / %	sa	sp
1	Adipose	0.0033	70	50	0.98	0.53
2	Bone	0.0049	80	15	1.4	1.47
3	Muscle	0.07	80	50	0.14	2.82
4	Stomach	0.01	70	80	0.97	0.97
5	Lungs	0.0056	75	80	1.23	1.51
6	Kidneys	0.3	75	70	0.45	1.05
7	Liver	0.15	85	85	1.7	0.53
8	Pancreas	0.3	75	70	0.45	1.05

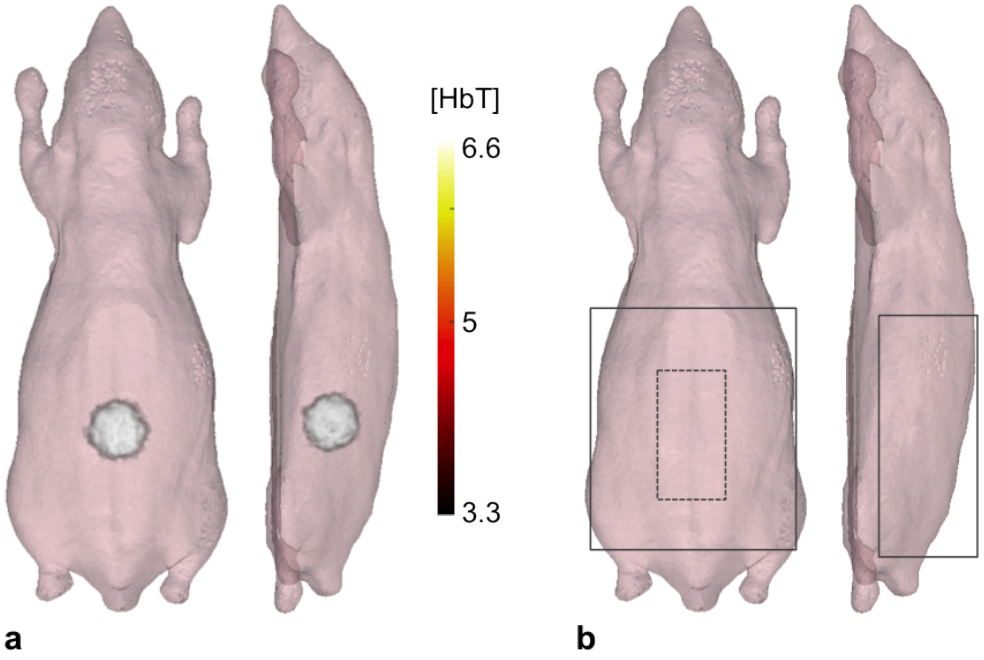

Figure 5.5: (a) simple_200 mesh, spherical anomaly has 200× the [HbT] of the bulk. Colourbar units: mM. The simple_2 model has the same structure, with the anomaly [HbT] = 0.0066 mM. (b) Areas occupied by DOT sources (dotted line), and surface detectors (solid line) in all simulations. DOT sources are positioned on the lower surface, surface detectors across the top surface of the model.

5.2.2.2 Noise Addition to Data

Tomographic DOT reconstructions were performed using both NS and SD algorithms on the noise-free (clean) data, data with 0.5% normally distributed noise added (using the 'add_noise' function in NIRFAST, [35]) and data with 0.5% noise and angular noise added. Angular noise was added in order to assess the efficacy of the SD method in accounting for the angular dependence of measured data at the CCD (which is currently accounted for using the free space model). Figure 5.6 shows the method of calculation of angular noise at each detector location. Assuming Lambertian emission of light from the surface of the animal [203], the maximum intensity emission is normal to the detector location on the surface, and the measurement at the CCD is $\cos\vartheta$ × maximum intensity, where ϑ is the angle between the

detector surface normal and the line connecting the surface detector to the CCD, assuming a point measurement at the CCD. The distance between the imaging platform and the CCD was assumed to be 320 mm, as is the case with the BLDOT system. Due to its geometric nature, this 'noise' is independent of wavelength so should be effectively accounted for using the SD method.

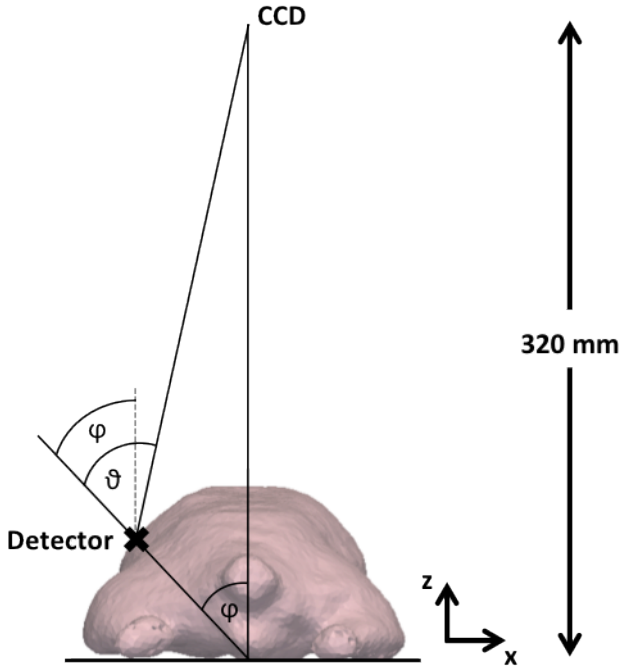

Figure 5.6: Angular noise addition to simulated measurement data. The noise is added in the x-z plane. Each measurement is multiplied by cosφ for each detector location. φ is calculated assuming that the distance between the imaging platform and the CCD is 320 mm (as in the BLDOT system). ϑ is the true angle between the CCD and the detector location but φ is used for simplicity.

To simplify the calculation of ϑ, the surface normal is approximated as the line intersecting the origin (located in these simulations at the central x and minimum z coordinates of the mesh) and the detector, and the line connecting the surface detector to the CCD is approximated as vertical, this results in the angle φ. Angular noise is added to each surface measurement, R, according to the equation:

$$\tilde{R} = R \times cos\varphi \tag{5.8}$$

where $\tilde{R}$ is the measurement with angular noise added. This is done at all measurement wavelengths. The angular noise is calculated considering the x-z plane only, the longitudinal y direction of the animal is ignored. This is in part to simplify the calculation, but also due to the small curvature of the animal in the y-z plane compared to the x-z plane, and so noise in this plane will contribute negligibly to the total angular noise.

If the SD method is able to account for the angular dependence of experimental data from the BLDOT system (and therefore all other non-contact optical imaging systems which require free space modelling) this suggests that the free space model is not a necessary data processing step when performing SD DOT, saving time and computational processing power.

5.2.2.3 Reconstruction of Chromophore Distribution

Data with the three noise levels (clean, 0.5% noise and 0.5% + angular noise) was used to reconstruct the internal chromophore distribution of the two simple models and the heterogeneous Digimouse model. Both the NS and SD algorithms were used to reconstruct in order to compare the capabilities of the two algorithms. No data processing was performed prior to the reconstruction to determine whether the SD method is capable of producing quantitatively accurate chromophore distributions without the data calibration step (as detailed in ref. [194]). The initial guess of optical properties in simple_2 and simple_200 cases is homogeneous 'adipose' (Table 5.3), the chromophore distribution in the heterogeneous case was reconstructed using both homogeneous 'adipose' and NSR or SDR reconstruction as the initial estimate. To simplify reconstructions, scatter is not included, only HbO, deoxyHb and water are reconstructed for. The scatter is assumed to be that of 'adipose'.

Qualitative assessment of the reconstructions was performed based on images of the recovered total haemoglobin concentration. The distribution of HbT only is shown in this section

as haemoglobin is the strongest absorber at NIR wavelengths (see Fig. 1.3 a which required the attenuation of water to be scaled by 1000× in order to enable comparison between water and haemoglobin attenuation), StO_2 is important physiologically but for the purposes of testing the SD method it is not considered here. Quantitative evaluation of the heterogeneous Digimouse recovered chromophore distribution was done by simulating combined DOT-BLT and analysing the quality of the BLT reconstructions (Section 5.3).

5.2.3 Results and Discussion

5.2.3.1 Simple Meshes

The recovered distribution of total haemoglobin content for the two simple models (simple_2 and simple_200) is shown in Fig.'s 5.7 and 5.8. When considering the clean data and data with 0.5% noise added, the recovered distribution of the chromophore is comparable using both NS and SD methods. This is confirmed by the comparable range of HbT concentration recovered by the two methods (Table 5.4). Note that the noise added to the data is more significant in the simple_2 model due to the low contrast in attenuation between the anomaly and the bulk, which explains the poorer performance of both NS and SD methods when applied to the simple_2 model.

When considering the data with angular noise added, a substantial difference in recovered HbT distribution is observed between the two methods used for reconstruction. This variation is particularly clear in the simple_2 case (Fig. 5.7). When scaled to the data range (Fig. 5.7, top right) the recovered distribution of HbT is seen to be concentrated at the central axis of the mesh. This is also true for the simple_200 case (Fig. 5.8). In contrast, the SD method is unaffected by the angular noise, performing comparably to the case with 0.5% random noise only added to the data in both simple_2 and simple_200 cases. This suggests that the SD method is successfully accounting for the angular noise, as expected from the theory detailed

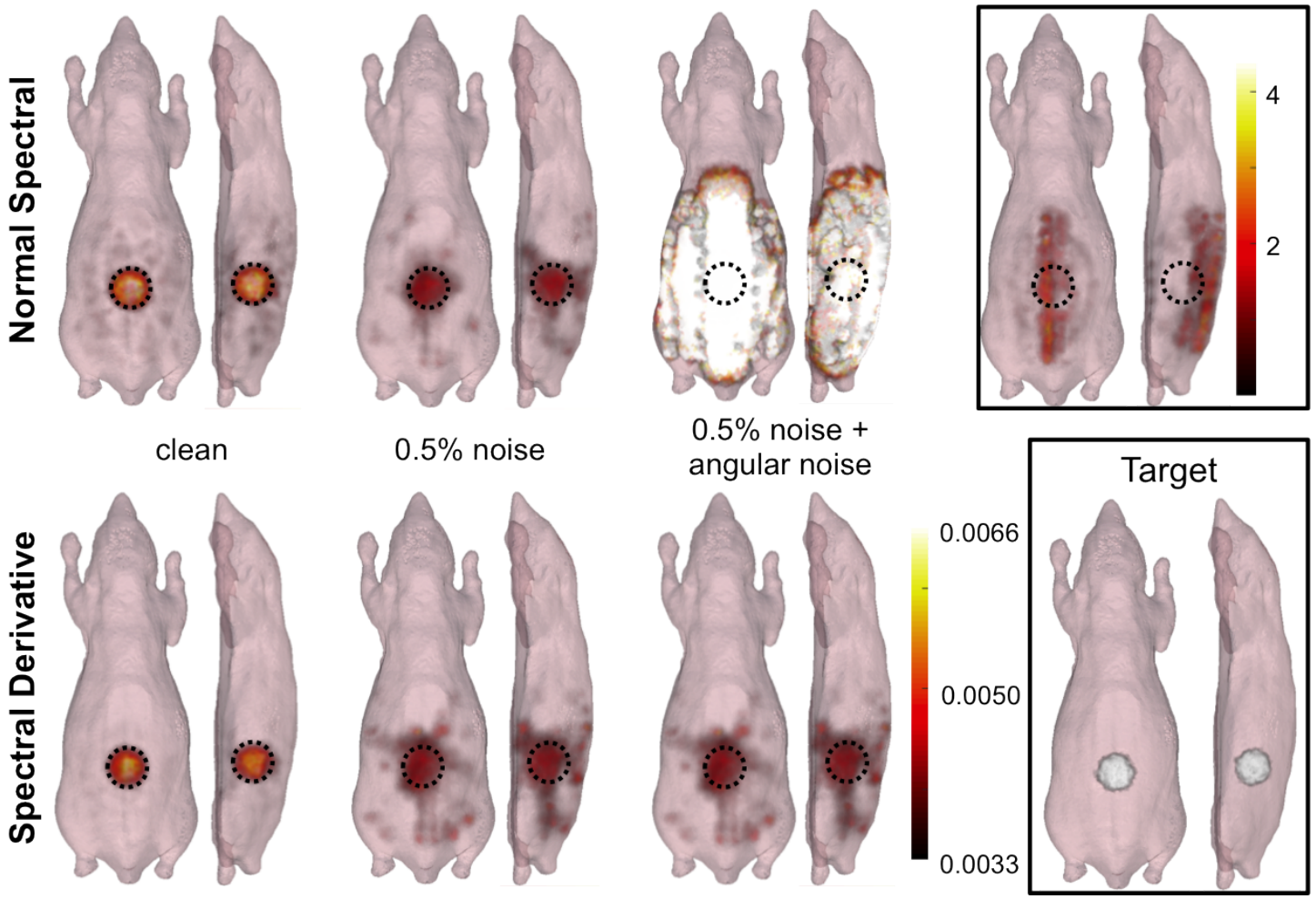

Figure 5.7: DOT reconstructions for total haemoglobin concentration for the simple_2 mouse mesh (spherical anomaly with double the haemoglobin concentration of the bulk) using both NS and SD models and three different noise levels in the measured data. The dotted circle indicates the target anomaly location. A common colourbar scale is used for all reconstructions. Additionally the boxed NS reconstruction (0.5% noise and angular noise) has been scaled to the data range for visualisation. The SD method is able to account for the angular noise, in contrast to the NS model. Colourbar units: mM.

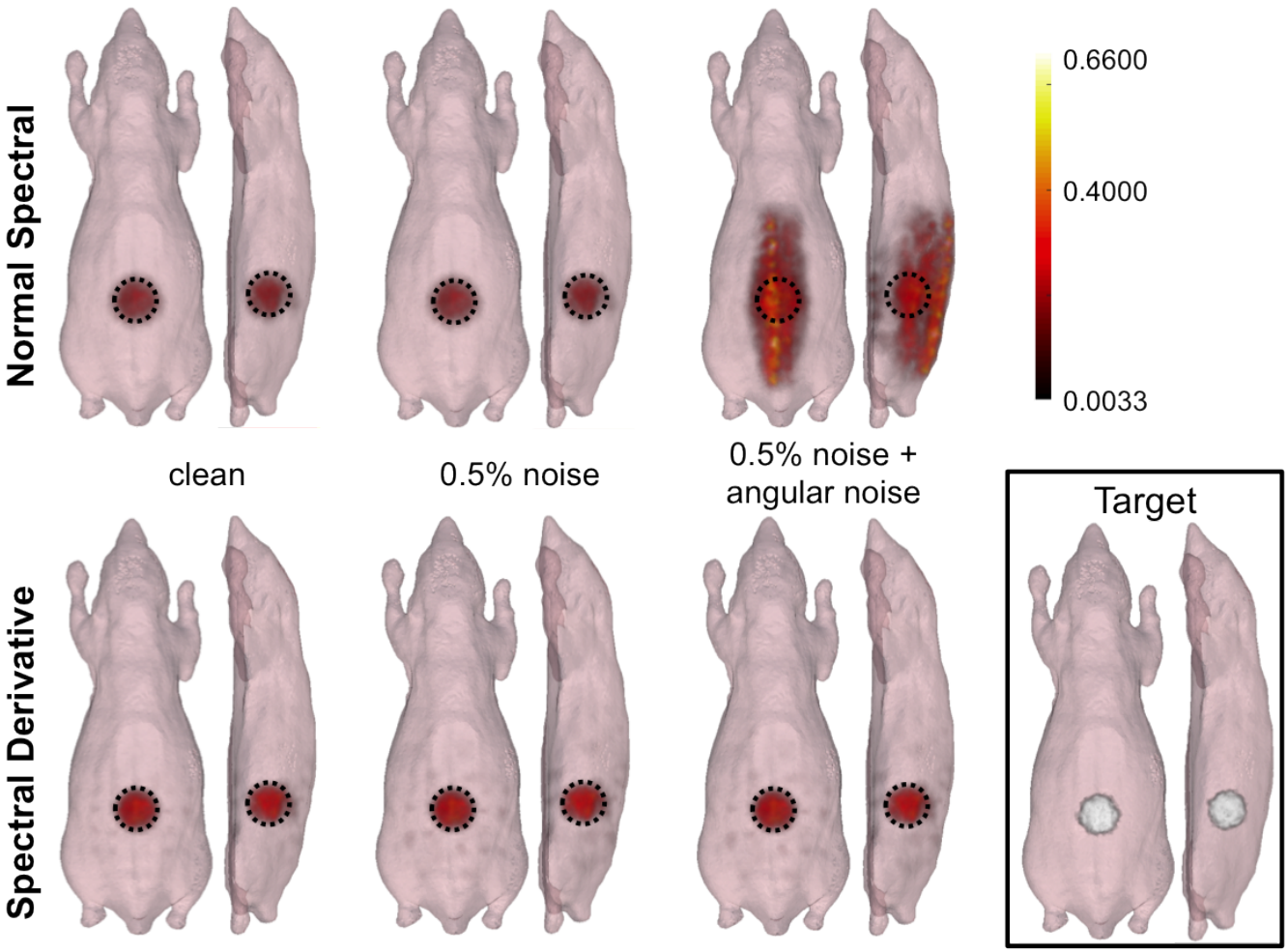

Figure 5.8: DOT reconstructions for total haemoglobin concentration for the simple_200 mouse mesh (anomaly with 200× the haemoglobin concentration of the bulk). The dotted circle indicates the target anomaly location. Reconstructions are shown for the NS and SD methods and using clean data and data with two types of noise added. All reconstructions are plotted on a common colourbar scale. The SD reconstruction algorithm was able to overcome angular noise present, with all reconstructions comparable to each other. The NS reconstruction algorithm was unable to overcome the angular noise present in the data. Colourbar units: mM.

in Section 5.2.1.

The inaccuracy in the range of concentration values recovered for data with angular noise added using the NS method is shown in Table 5.4. The maximum recovered concentration was $> 650\times$ the true value of 0.0066 mM for the simple_2 model, while the SD method has been able to recover a value comparable to the true concentration. The error in the recovered concentration using the NS method for the simple_200 model is less pronounced and the SD method has recovered a concentration which is lower than the target value. Consultation of these values alone would suggest that the NS method has outperformed the SD method in this case. However, the inaccuracy of the NS recovered distribution is shown in Fig. 5.8 and the robustness of the SD method to the change in noise in the data is shown (additionally demonstrated by the consistency of the recovered concentrations, Table 5.4).

The contrast between the anomaly and bulk optical properties in the simple_200 model is more comparable to expected values, as shown in Table 5.3 the variation in [HbT] is up to $91\times$. The enhanced contrast of the anomaly in this model causes the measured data transmitted through this region to be attenuated by a greater extent than in the simple_2 model, enabling more effective reconstruction of the anomaly to be achieved.

The performance of the SD method when applied to this simple model is promising in comparison to the NS method, particularly when considering the recovered chromophore distribution, but the method must be validated in a more complex model if it is to be applied to *in vivo* data.

5.2.3.2 Heterogeneous Mesh

The recovered total haemoglobin distribution for the heterogeneous Digimouse atlas is shown in Fig. 5.9, the initial guess of the chromophore distribution was homogeneous adipose (Table 5.3). Similarly to the simple models in the previous section, both the NS and SD methods recover comparable distributions of HbT when considering clean data. In this heterogeneous

Table 5.4: Minimum and maximum HbT concentration (mM) for distributions recovered using NS and SD models from data at all noise levels and the simple_2, simple_200 and heterogeneous Digimouse model ('Hetero') assuming an initial chromophore distribution of homogeneous 'adipose'. 'Hetero + region initial' refers to the heterogeneous model assuming a homogeneous initial chromophore distribution as determined by the corresponding NSR or SDR method. The target concentration for HbT in each case is indicated in bold.

		Clean		0.5% noise		0.5% noise + angle	
		Min	Max	Min	Max	Min	Max
Simple_2	NS	0.0027	0.0089	0.0018	0.0049	0.00005	4.3730
	SD	0.0030	0.0070	0.0012	0.0054	0.0012	0.0054
	Target	**0.0033**	**0.0066**	**0.0033**	**0.0066**	**0.0033**	**0.0066**
Simple_200	NS	3.43×10^{-5}	0.2187	3.10×10^{-5}	0.2184	0.0001	0.8139
	SD	0.84×10^{-5}	0.3506	2.64×10^{-5}	0.3763	2.67×10^{-5}	0.3763
	Target	**0.0033**	**0.6600**	**0.0033**	**0.6600**	**0.0033**	**0.6600**
Hetero	NS	1.32×10^{-5}	0.3968	7.05×10^{-5}	0.2374	6.77×10^{-5}	0.8987
	SD	0.47×10^{-5}	0.3557	1.27×10^{-5}	0.3847	0.97×10^{-5}	0.3847
	Target	**0.0033**	**0.3000**	**0.0033**	**0.3000**	**0.0033**	**0.3000**
Hetero + region initial	NS	10.1×10^{-5}	0.2309	10.5×10^{-5}	0.2306	10.0×10^{-5}	14.7327
	SD	0.46×10^{-5}	0.4015	1.60×10^{-5}	0.3964	1.47×10^{-5}	0.3964
	Target	**0.0033**	**0.3000**	**0.0033**	**0.3000**	**0.0033**	**0.3000**

model the SD method qualitatively appears to outperform the NS method when any noise is considered in the data. As can be seen in Fig. 5.9 the NS method recovers a lower HbT concentration than the SD method in the kidneys, (true concentration 0.3 mM) in the case of 0.5% random noise in the data. Considering angular noise, the NS method is unable to overcome this type of noise, recovering a HbT distribution along the central axis of the animal similarly to the simple model. The SD method is able to account for the angular noise, recovering a HbT distribution comparable to the case without angular noise added. These early results, which show improvement in recovered chromophore distribution when using the SD method over the NS method, are very encouraging.

The chromophore distributions in Fig. 5.9 have been plotted on a common colourbar scale to enable comparison of the reconstructions. The maximum and minimum recovered HbT concentrations are shown in Table 5.4 ('Hetero'). As shown by these values, in all cases for

both models, the minimum recovered concentration is low, however considering the maximum concentration, the SD method has been able to recover a concentration comparable to the target at all noise levels, further demonstrating the robustness of this model. The NS method has again been unable to account for the angular noise in the data producing a maximum intensity of 3× the true value, while performing well with clean data and reasonably well in the case of 0.5% noise where there was a slight decrease in the maximum concentration.

It is essential to have a good initial estimate of the chromophore distribution within the imaging subject when performing DOT reconstructions. In this simulation case, the background optical properties are known to be 'adipose' optical properties, as can be seen in the atlas model where adipose tissue occupies the whole background of the model not occupied by organs (Fig. 4.1), so this is believed to be a good initial estimate. Experimentally an accurate initial estimate of the optical properties is more difficult to approximate. To determine the efficacy of the SDR method in calculating an initial chromophore distribution, the NSR and SDR methods are applied to data from the heterogeneous model.

Table 5.5: Region reconstruction results for the heterogeneous mouse mesh. The SDR method is able to recover chromophore concentrations closer to the target value than the NSR method in the majority of cases, however the NSR method seems to have performed well for the 0.5% noise + angular noise case. The total haemoglobin concentration and water content of 'adipose' tissue from the Digimouse atlas [149] have been included for reference. The SDR method recovers properties comparable to adipose for all noise levels.

Data	Method	HbO / mM	deoxyHb / mM	HbT / mM	Water / %
Target		**0.0144**	**0.0047**	**0.0191**	**52.65**
Clean	NSR	0.0003	0.000014	0.0003	42.01
	SDR	0.0045	0.0005	0.0050	52.18
0.5% noise	NSR	0.0003	0.000014	0.0003	41.97
	SDR	0.0045	0.0005	0.0050	52.16
0.5% noise + angle	NSR	0.0046	0.0032	0.0078	47.66
	SDR	0.0045	0.0005	0.0050	52.16
Adipose				**0.0033**	**50.00**

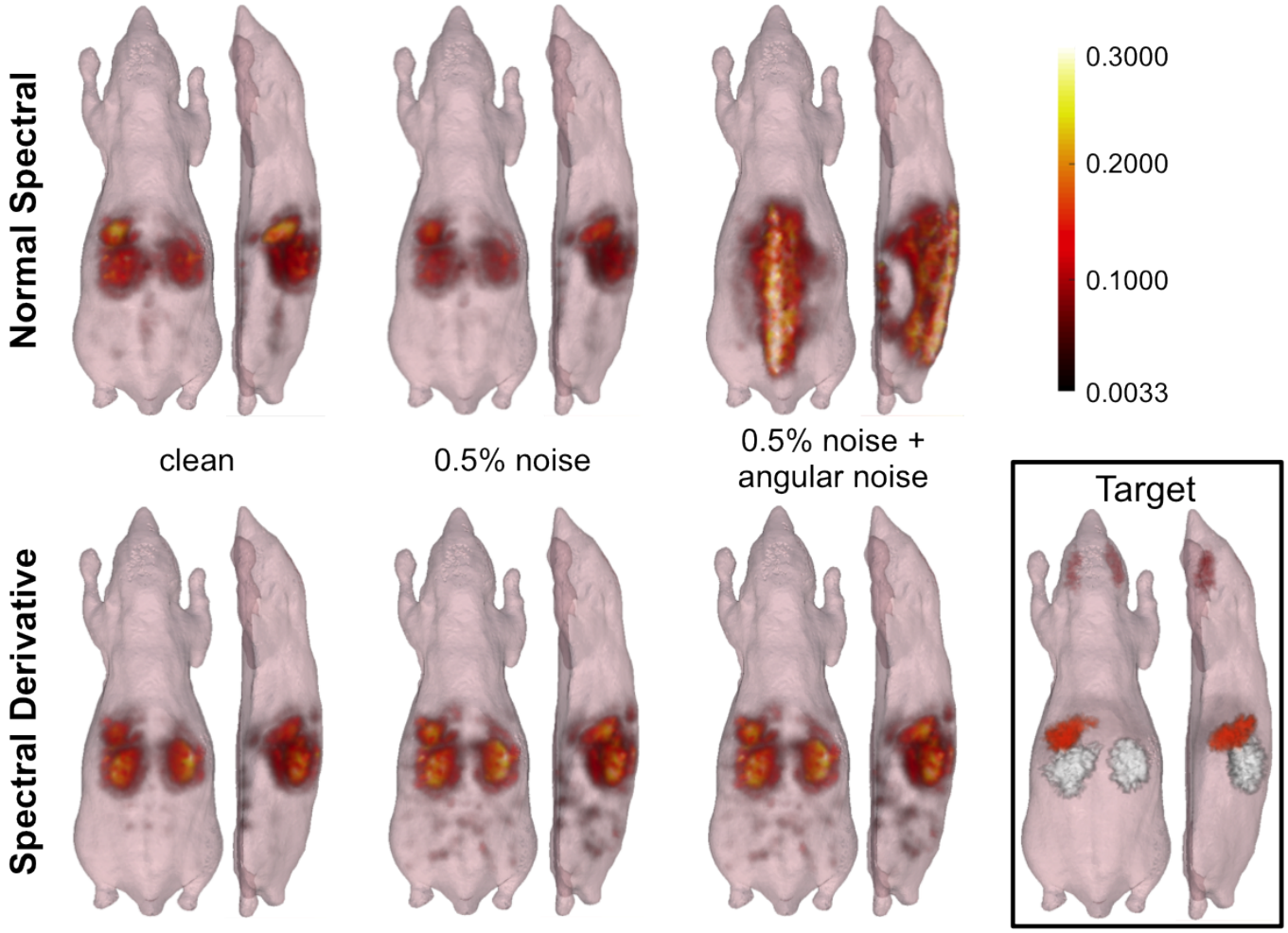

Figure 5.9: DOT reconstructions for total haemoglobin concentration for the complex heterogeneous mouse mesh assuming an initial estimate of chromophore concentrations of homogeneous 'adipose'. The reconstructions were performed on data with three noise levels (clean, 0.5% noise and 0.5% noise + angular noise) and with both NS and SD methods. The SD reconstructions are consistent across all noise levels, whereas the NS method has not accounted for the angular noise present in the data. Colourbar units: mM.

Table 5.5 shows the region reconstruction results (both NSR and SDR) for the heterogeneous Digimouse atlas along with approximate target concentrations. The target concentrations were determined by calculating the node weighted average of optical properties in the region of the mesh covered by the surface detectors. The initial concentrations given to the NSR and SDR algorithms were 0.1 mM, 0.1 mM and 50% for deoxyHb, HbO and water respectively. As can be seen in the table, the SDR method outperforms the NSR method for the clean and 0.5% noise data, however, the concentration estimates are still lower than the target values. Conversely, the concentration of HbT recovered by the NSR method for 0.5% noise + angular noise is closer to the target value than the concentration recovered by the SDR method. Considering water content, both models produce values which are comparable to the target values, however the SDR method has recovered a water content very close to the target value. Although the accuracy of the recovered concentrations of all chromophores varies for all noise levels in the data for the NSR method, the SDR method produces consistent concentration estimates at all noise levels, suggesting that even in this simplified DOT reconstruction the SDR method is successfully accounting for noise in the data. The SDR method has proved to be more robust than the NSR method for determining initial chromophore concentration estimates for the full DOT reconstruction.

These homogeneous values were used as initial estimates of chromophore concentrations to perform full tomographic DOT reconstructions, shown in Fig. 5.10. The internal structure of the HbT distribution can be seen in these reconstructions, similarly to those calculated with an initial estimate of 'adipose' (Fig. 5.9). The NS reconstructions in this case appear to underdetermine HbT concentration in the kidneys, this is due to the lower accuracy of the initial estimate of the optical properties determined by the NSR reconstruction. As with all other examples the NS method was unable to account for the angular noise in the data.

Considering the range of recovered HbT concentrations (Table 5.4), the minimum recovered concentration of HbT is low for data with all noise levels and both NS and SD methods.

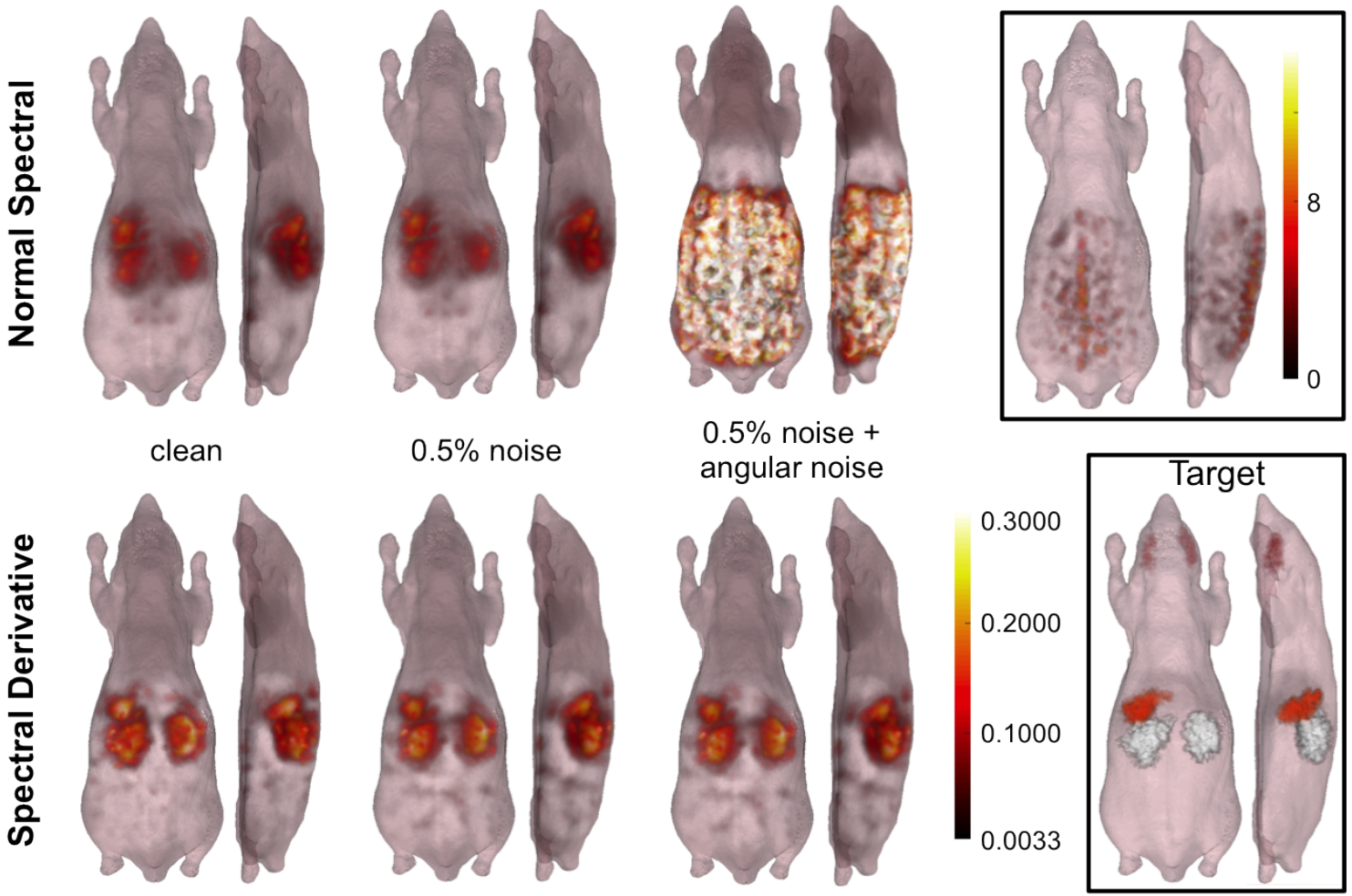

Figure 5.10: DOT reconstructions for total haemoglobin concentration for the complex heterogeneous mouse mesh with an initial estimate of optical properties obtained from the region reconstruction (either NSR or SDR corresponding to the full DOT reconstruction method used), Table 5.5. As with the initial guess of homogeneous adipose the SD reconstructions are consistent across all noise levels and the NS method has not been able to account for the angular noise in the data. Colourbar units: mM.

The maximum concentrations are comparable to the target values for cases with no noise and 0.5% noise added, the NS method produces concentrations which are low but slightly closer to the target value than the SD method, which produces higher values. Where angular noise has been added to the data, the NS method recovers a maximum concentration of 50× the target value. This, compared to the maximum recovered HbT concentration (using the NS method) when using homogeneous adipose as an initial estimate of the chromophore distribution (3× greater than the target value), demonstrates the importance of gaining an accurate initial optical property estimate for full DOT. This data also highlights the inaccuracy of the NSR method. The ability of the SD method to recover comparable HbT distributions from all sets of data, with comparable concentration ranges, is extremely promising when applying this SD processing workflow (SDR reconstruction followed by full SD tomographic reconstruction).

The robustness of the SD method to noise in the data compared to the NS method, when applied to this complex model suggests that the SD method has potential in overcoming noise experimentally in a murine model. This is explored in Chapter 6. In order to quantitatively assess the accuracy of the recovered chromophore distributions, combined DOT-BLT was performed on the Digimouse atlas. The methods and results from this investigation are detailed in the following section.

5.3 DOT Optical Property Distribution as Prior Knowledge for use in BLT

To quantitatively evaluate the efficacy of the SD method in performing DOT reconstructions, the chromophore distributions for the heterogeneous mouse atlas recovered in Section 5.2.3.2, were used as the optical property estimate for performing BLT source recovery. The BLT source distribution was also recovered using a range of optical properties to determine the

efficacy of the SD method in combined DOT-BLT.

5.3.1 Method

The method used in this simulation is as described in Chapter 4. The pancreas of the Digimouse atlas was modelled to be bioluminescently labelled with firefly luciferase and surface measurement data calculated at 600, 623 and 643 nm using NIRFAST [35]. The CSCG reconstruction method [50] was used to reconstruct the internal source distribution. Filter bandwidth was ignored in this study, data were simulated assuming a bandwidth of 1 nm, so the NBW Jacobian only (as defined in Section 4.2) was used in BLT reconstructions. A range of optical properties were used as prior knowledge for the BLT reconstructions, as detailed in Table 5.6.

Table 5.6: Details of the different optical properties used in BLT source recovery of the Digimouse atlas. All DOT determined optical property distributions were recovered in Section 5.2.3.2. The name of the optical property will be used to refer to the optical property in the remainder of the text.

	Optical Property Name	Details
1	True heterogeneous	True Digimouse optical properties
2	Homogeneous adipose	Adipose (Table 5.3)
3	DOT - NS - Clean	Properties recovered from clean data using the NS method
4	DOT - SD - Clean	Properties recovered from clean data using the SD method
5	DOT - NS - noise 0.5% + angle	Properties recovered using the NS method, from data with 0.5% random noise and angular noise added
6	DOT - SD - noise 0.5% + angle	Properties recovered using the SD method, from data with 0.5% random noise and angular noise added
7	DOT - SD - noise 0.5% + angle (from region initial)	Properties recovered using the SD method with an initial estimate of homogeneous optical properties determined using the SDR method, from data with 0.5% random noise and angular noise added

Qualitative inspection of the recovered sources was performed along with quantitative analysis in calculating the error in the centre-of-mass (recovered source considered over 50 % of the maximum intensity) and intensity per unit volume (recovered source considered over

an empirically chosen threshold of 1 % of maximum intensity) of the recovered source.

5.3.2 Results and Discussion

The BLT reconstructions for the range of optical properties along with the target source are shown in Fig. 5.11. All optical properties have achieved a recovered source in qualitatively the correct position within the animal but there is variation in appearance of all sources. Particularly apparent is the appearance of the source recovered using homogeneous adipose attenuation, two regions of recovered source can be seen, one deeper than the other. This suggests that the approximated attenuation is too low, the lateral view of this bioluminescent source distribution has a similar appearance to that shown in Fig. 5.1 d. The inaccuracy in this reconstruction is expected as the underlying attenuation of the mouse atlas is not homogeneous and organs in the abdomen surrounding the pancreas have much higher chromophore concentrations than adipose (Table 5.3). Qualitatively, reconstructions 3 and 4, which used DOT determined optical properties from clean data using NS and SD methods respectively appear similar. This is expected due to the similarity seen in the recovered optical property distribution (Fig. 5.9) and is confirmed by the similarity in the centre-of-mass error of these two sources (Fig. 5.12). The source recovered using the 'DOT-NS-noise 0.5% + angle' optical properties, is surprisingly qualitatively accurate when considering the inaccuracy of the recovered optical property distribution (Fig. 5.9). The source appears deep compared to the true source location, reflected in the centre-of-mass error of the recovered source (Fig. 5.12), but laterally appears in a realistic position. This could be due to the lateral position of the pancreas avoiding the central high concentration of HbT recovered using the NS DOT method, therefore enabling the bioluminescent signal to be detected at lateral detectors. Reconstructions 6 and 7 appear qualitatively very similar, as expected due to the similarity of the recovered optical properties using the SD method, with initial estimates of homogeneous adipose and SDR reconstruction respectively.

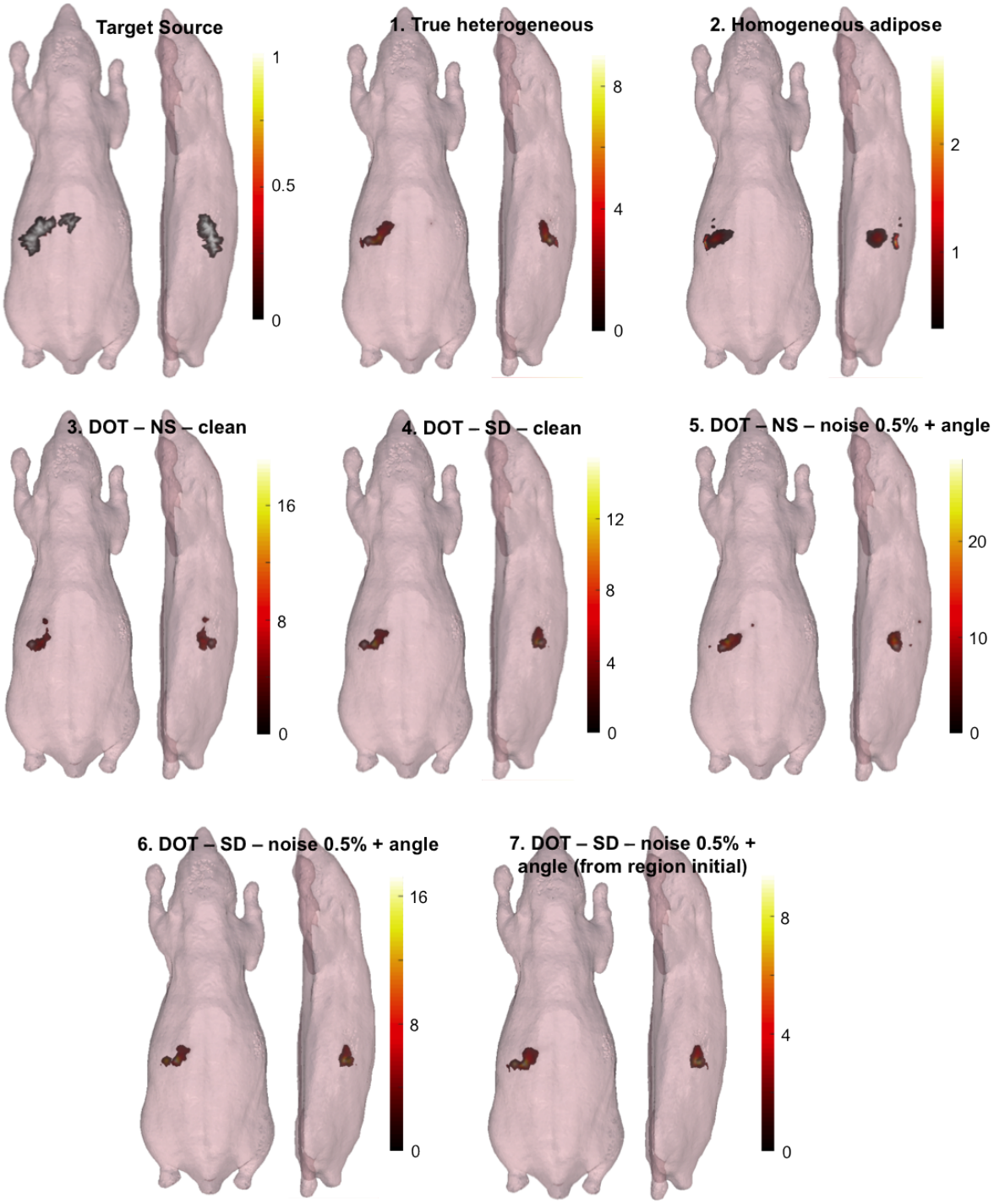

Figure 5.11: Target bioluminescent source and sources recovered from a range of optical properties (indicated in individual cases). The similarity in appearance of all recovered sources can be seen, there are subtle variations however, and there is varition in the intensity of each recovered source. Colourbar units: arbitrary intensity units.

Note the differences in the colourbar scales in all cases in Fig. 5.11, these were scaled individually to aid visualisation, and highlight the differences in the range of intensities of the recovered bioluminescent source due to the differing underlying attenuation assumed in the reconstruction.

Considering the error in centre-of-mass of the recovered sources (Fig. 5.12 a), the lowest error is from the source recovered using the true heterogeneous optical properties, as expected as this is the ideal scenario for BLT reconstruction. The source recovered assuming homogeneous adipose optical properties has the highest error, which is expected due to the known inaccuracy of the optical property distribution and the observed inaccuracy of the recovered source. The similarity in the centre-of-mass errors of sources recovered using the SD method with clean data, and data with 0.5% random noise and angular noise added (reconstructions 4 and 6 respectively), supports qualitative assessment of the recovered sources and the similarity in the optical property distribution (Fig. 5.9) and demonstrates the ability of the SD method to account for noise in the data.

The source recovered assuming 'DOT-SD-noise 0.5% + angle (from region initial)' optical properties, the method which will be adopted experimentally (reconstruction 7), has a small centre-of-mass error which is comparable to that achieved when using the true optical properties to reconstruct. This suggests that using the SDR method to gain an initial estimate of optical properties to use in the full DOT reconstruction will be effective when performing experimental work.

The intensity per unit volume of all recovered bioluminescent sources is shown in Fig. 5.12 b, with the target indicated. Using the true optical properties this value has been calculated as being 28% too high. This could be due to the reconstruction method used. The CSCG algorithm assumes a sparse source distribution and tries to reconstruct the most compact source distribution possible, the compact nature of this recovered source compared to the target source can be seen. Due to this compactness, the intensity must be higher compared

to the true value in order to produce equivalent surface measurements.

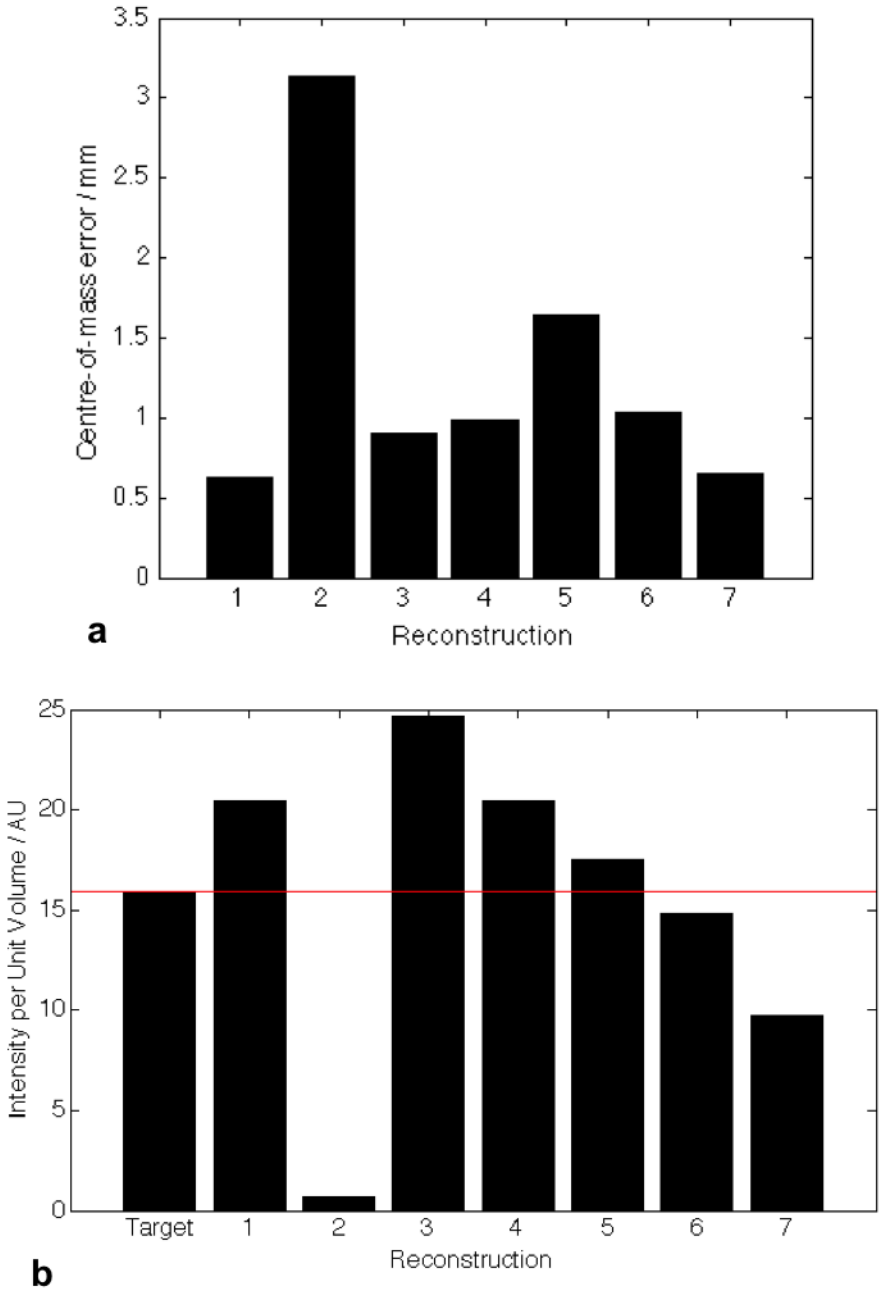

Figure 5.12: Quantitative analysis of BLT recovered sources for a range of optical properties. (a) Error in centre-of-mass of recovered source compared to target (mm); (b) Intensity per unit volume of recovered sources (arbitrary intensity units / mm^3).

As expected, assuming homogeneous adipose optical properties has produced a reconstruction with a large error in the intensity per unit volume (95.7% low). Considering the sources recovered assuming DOT optical properties from clean data (reconstructions 3 and 4), the SD method has achieved an intensity per unit volume comparable to that achieved using the true optical properties (28.31% high), with the NS method having a larger error of 54.6%.

Interestingly, reconstruction 5 (DOT-NS-noise 0.5% + angle) achieved an intensity per unit volume close to the target value, the value is only 9.95% higher than the target value, this is likely to be due to the lateral position of the pancreas avoiding the central high concentration of HbT recovered using the NS DOT method as described above. However when visualising the chromophore distribution (Fig. 5.9) it is clear that the distribution is not anatomically correct. The source recovered using 'DOT-SD-noise 0.5% + angle' properties (reconstruction 6), achieved a bioluminescent source intensity per unit volume just 7.2% lower than the true value. This is really promising when considering use of the method *in vivo*.

However the intensity per unit volume for the source recovered assuming optical properties recovered using SDR and then SD methods is 39.1% lower than expected. Visually the recovered source is larger than reconstruction 6 and with a lower intensity (by inspection of the colourbar), explaining the lower intensity per unit volume calculated comparing the two SD reconstructions.

These results show that the SD method is able to produce optical property distributions that, when used as prior knowledge for BLT source recovery, are able to produce source distributions which are qualitatively and quantitatively comparable to the bioluminescent source distributions recovered with ground truth optical properties. This suggests that the method is able to overcome the need for data calibration and free space modelling. However, there is still some error in the recovered source. The effect of using different optical property distributions on the recovered bioluminescent source when performing BLT is also shown,

and combining BLT and DOT improved the quantitative accuracy of the recovered source compared to that using homogeneous estimates of the optical properties. This suggests that the two imaging techniques are complementary to each other and can be used together in order to increase the quantitative accuracy of BLT agreeing with previous findings [37, 43–45, 48].

The DOT-BLT data presented in this section used a complex-shaped bioluminescent source, the pancreas. In order to determine which optical properties enable the most quantitatively accurate bioluminescent source recovery in BLT with more confidence, it would be advisable to repeat this simulation study with a simpler bioluminescent source. For example a spherical source could be positioned at multiple different locations within the animal and the quantitative accuracy of the recovered source determined using a range of optical properties, such as those used in this section. The shape of the source could then be made gradually more complex and the quantitative accuracy of the recovered source determined for each different bioluminescent source. This would enable the ability of the SD method in gaining prior optical property knowledge for use in BLT source recovery to be evaluated more thoroughly.

5.4 Conclusions

This chapter demonstrates the importance of using accurate optical properties when performing quantitative BLT. A spectral derivative reconstruction algorithm for DOT using a non-contact imaging system was developed and presented as a potential alternative to the spectral reconstruction algorithm (NS) which is traditionally used. The NS method requires data calibration and free space modelling data processing steps before tomographic reconstruction, to account for system offsets and obtain initial estimates of the optical property distribution, and account for angular noise and the passage of light through the free space between the surface of the imaging subject and the CCD. The SD method was shown to

produce chromophore distributions which were quantitatively more accurate than those produced by the NS method and with distributions comparable to the target distributions. The method was able to account for angular noise comparable to that experienced experimentally, which is promising for application of the method to experimental data.

Simulations on simple and complex mouse models demonstrated that the SD method was robust to noise in the measured data, whereas the NS method was affected by the noise, producing inaccurate chromophore distributions where angular noise was added to the data. The robustness of the SD method to varying noise levels in the data was demonstrated by the similar total haemoglobin concentration in all cases, whereas the NS method produced different chromophore concentrations for all noise levels in the data. Although the spacing between adjacent measurement wavelengths in this work was much larger than had been investigated in previous work applying the SD method [200], the efficacy of the method in accounting for the noise in the simulation data in this Chapter suggests that the assumption that noise is constant across adjacent measurement wavelengths is an appropriate assumption to make in this case.

The region-based reconstruction method (SDR), which was used to produce initial homogeneous estimates of chromophore concentrations for use in full DOT reconstructions, was able to produce good initial concentration estimates in replacement of the usual data calibration procedure. At a later date this should be developed so that a further initial guess of the chromophore concentration is not needed for the SDR method. But for the validation of the full SD method the SDR method has been effective. These DOT results suggest that it is possible to perform SD DOT reconstruction without the need for data calibration procedures or free space modelling prior to reconstruction.

Further demonstration of the importance of using accurate optical properties and the efficacy of the SD method was done through DOT-BLT simulation using the heterogeneous Digimouse atlas. When using SD determined optical properties the recovered bioluminescent

source distribution was qualitatively and quantitatively comparable to the bioluminescent source distributions recovered with ground truth optical properties. The homogeneous optical property estimate was found to produce bioluminescent source distributions with a lower accuracy than true and DOT determined optical properties.

All results presented here demonstrate the potential of the SD method in becoming a replacement to the currently used NS method for DOT reconstruction. The method would not require initial data calibration and Free Space modelling prior to reconstruction as is required when using the NS method. The SD method proved to be robust to noise in the data and suggests that with further experimental validation the SD method (combined with the SDR method to gain the initial optical property estimate) can replace the NS method. In order to evaluate this further, experiments were performed using a murine model, results are presented in Chapter 6.

Chapter 6

Dual Modality Diffuse Optical and Bioluminescence Tomography of a Murine Model

Chapter 5 outlined and demonstrated the potential of the Spectral Derivative (SD) method in reconstructing chromophore distributions in a murine simulation model. The enhanced quantitative accuracy of BLT when DOT recovered chromophore concentrations were used was demonstrated. The results suggested that using the SD method in DOT and then subsequent use of the recovered optical properties as prior knowledge for BLT reconstruction has the potential to increase the quantitative accuracy of BLT when applied in an *in vivo* murine model, as the effect of wavelength independent noise can be eliminated or minimised. The work in this chapter takes a step towards this eventual aim and applies combined DOT-BLT in a *post mortem* murine model, using data acquired using the BLDOT system.

In preparation for data collection, modifications were made to the BLDOT system to improve the existing DOT component of the system. The following sections detail these modifications along with characterisation of the updated system. The data collection and

analysis process for DOT in the BLDOT system will then be outlined before applying this process to murine data collection. The murine data will build on simulation data presented in Chapter 5, demonstrating the capability of the SD method and the importance of using accurate optical properties when performing quantitative BLT. The filter bandwidth model for BLT source recovery presented in Chapter 4 (the WBW model) is also validated in a murine model for the first time.

6.1 Updates to the Existing DOT Component of the BLDOT System

The existing DOT hardware is described in ref.'s [48, 49]. Briefly, the system consisted of a pocket projector (PK-102; Optoma, UK) positioned underneath the imaging platform as shown in Fig. 1.5, coupled to an optical fibre (1000 μm diameter, 2 m length, QP1000-2-VIS-BX; Ocean Optics, UK) which was connected to a tungsten-halogen lamp (HL-2000-FHSA; Ocean Optics, UK). During DOT data acquisition the projector projected a sequence of 36 Gaussian sources which mimicked a point fibre source of standard deviation 2 mm at the lower surface of the imaging subject [48]. Multi-spectral images were taken of the light transmitted through the imaging subject from each source. When performing DOT data acquisition for a block phantom (solid plastic of dimensions 33×26×40 mm; Biomimic, INO, Quebec, Canada; see Appendix A.1 of ref. [48], optical properties characterised in ref. [197]) the total acquisition time was more than an hour (including surface capture). This long acquisition time is a disadvantage when performing pre-clinical DOT for use as prior knowledge in BLT as the time which an animal is anaesthetised for is dramatically increased and throughput is decreased. A main factor in the long acquisition time was the low intensity of the diffuse light source due to inefficient fibre-projector coupling. The detected signal from the fibre coupled to the pocket projector was $< 15\%$ of that from the fibre alone (Fig. 6.1) [48].

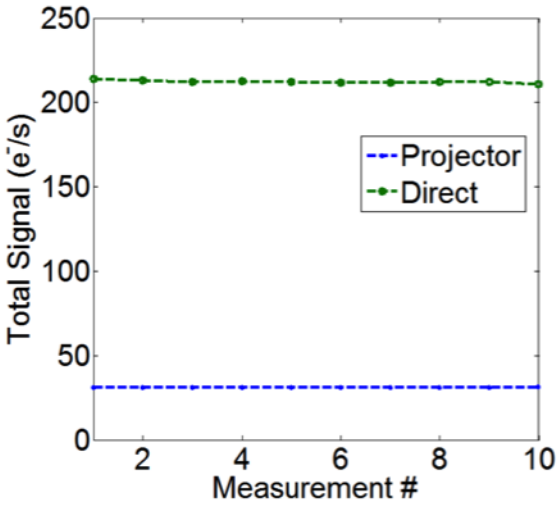

Figure 6.1: Measurements of the optical fibre alone illuminating a plain white sheet of paper (green line, 'Direct') and coupled to the projector which was projecting uniformly white (blue line, 'Projector'). A tungsten-halogen lamp was used for illumination in both cases. The decrease in intensity of the signal when the fibre is coupled to the projector compared to the fibre alone is clear. Reproduced from ref. [48].

In order to decrease the data acquisition time and to increase the intensity of the light available from the DOT source, the DOT component of the BLDOT imaging system was updated. This component remains under the imaging platform and replaces the pocket projector (Fig. 6.2 a). The existing optical fibre was replaced with a more flexible fibre (1000 μm diameter, 2 m length, FP1000URT; Thorlabs) which was mounted onto a two-dimensional linear translational stage (X-Y translational stage, Fig. 6.2 b and c; Thorlabs, MTS50-Z8) with the tip of the fibre positioned as close to the imaging platform as possible (of the order of $\sim$2 mm) to avoid light leakage. Custom LabVIEW software was written to control the position of the translational stage (and therefore the fibre), which could be moved to discrete positions in the range 0-50 mm with a resolution of 0.8 μm, in both x and y dimensions.

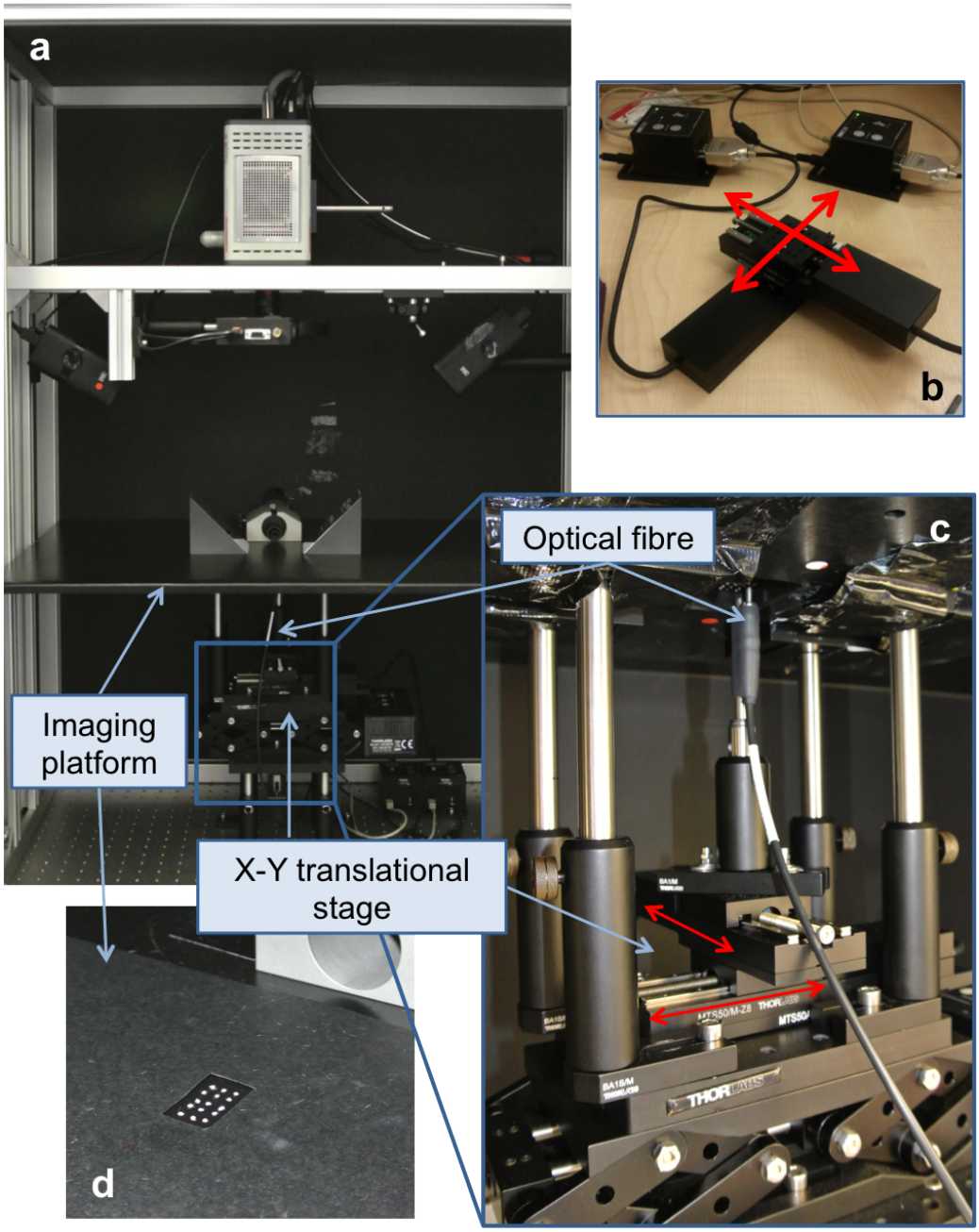

Figure 6.2: Modifications to the existing DOT component of the BLDOT imaging system. (a) Whole imaging system with the X-Y translational stage which provides the DOT illumination indicated. (b) The two-dimensional (X-Y) translational stage before incorporation in to the BLDOT system. (c) Close-up of the X-Y translational stage *in situ* in the BLDOT system, underneath the imaging platform, with the optical fibre mounted on top. (d) Image of the source locations in the imaging platform, a grid of holes are drilled in the platform. The optical fibre is placed underneath this section of the platform and moved underneath each hole during DOT imaging to change the source position.

Initially it was decided that fifteen sources in a 3×5 grid of ∼4 mm spacing would be used for data collection (Fig. 6.2 d), however this can be customised by the user. This covers an area of 8×16 mm which will cover a large proportion of the mouse abdomen. The existing projected Gaussian DOT illumination sources had a standard deviation of ∼2 mm [48] and therefore a spacing of approximately 4 mm (see Fig. 6.3), so the new fibre source distribution has a similar spacing to the old sources but occupies a smaller area (the area covered by the new DOT sources compared to the existing source distribution is shown in Fig. 6.3). Optimisation of the source positions (including drilling further holes in the imaging platform to fully enable customisation) is required but is beyond the scope of this thesis, the 3×5 grid is used in the work presented in this chapter.

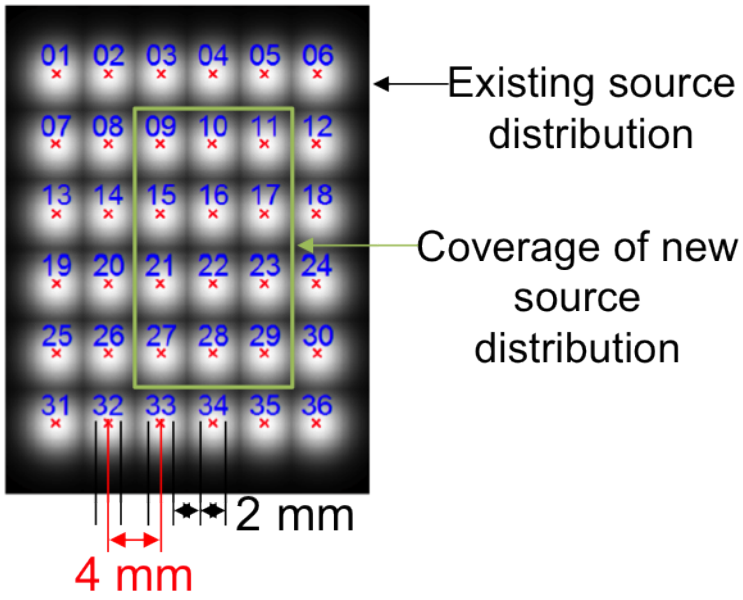

Figure 6.3: Existing distribution of DOT sources showing the standard deviation (black) and spacing (red). The coverage of the new source distribution is indicated in green.

6.1.1 Stability of the Light Source Over Time

To ensure the emission of the light source was constant over time, images were taken of reflected light from a 99% Spectralon reflectance standard (Labsphere, North Sutton, NH, USA). The optical fibre, connected to the tungsten halogen lamp, was mounted above the imaging platform. Images of the reflected light were taken at 620 nm (band pass filter with bandwidth 10 nm, Thorlabs) every minute for 20 mins. To analyse the reflectance images, the total intensity within an ROI encompassing the centre of the phantom was calculated (Fig. 6.4). The data is shown in Fig. 6.4 b and shows the intensity to vary negligibly ($<$ 1%) over the timescale of the experiment.

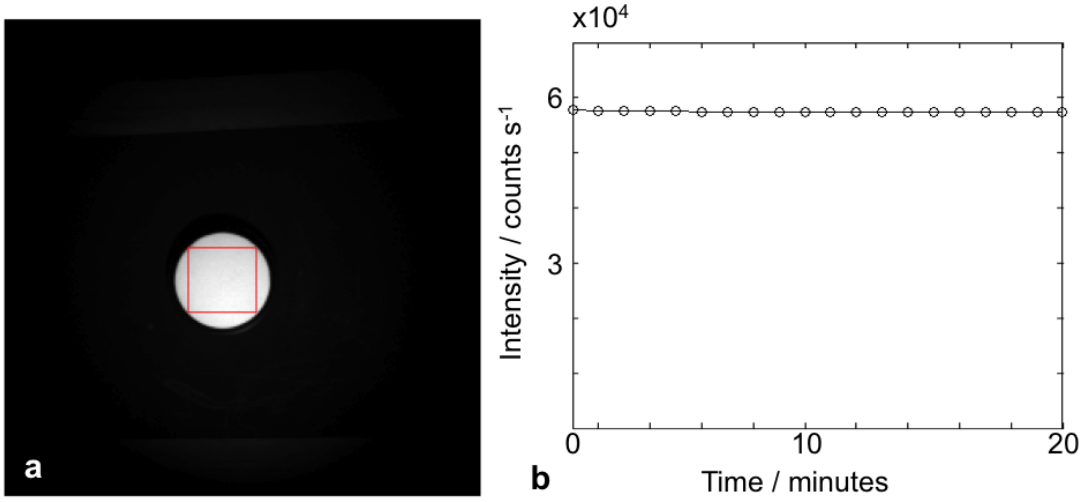

Figure 6.4: (a) Reflectance image of light from the tungsten-halogen lamp in the BLDOT system with ROI used to calculate total intensity indicated. (b) Variation in intensity of the light source at 620 nm over 20 minutes.

6.1.2 Instrument Response Function

The intensity detected at the CCD is not the true intensity of the light emitted within the imaging system, which is subject to attenuation and scatter in free space and is affected by passage through band pass filters and apertures and lenses within the system. The relative

intensity between measurement wavelengths used in the BLDOT system was measured (as detailed below) and the resulting instrument response function (IRF) used to normalise measured DOT transmission data to remove any dependence of the measured data on the spectral response of the imaging system.

To measure the IRF for the BLDOT system, images (5 to enable averaging) were taken of a single DOT source location with a piece of white paper placed on the imaging platform (assuming that the paper has uniform spectral attenuation at near infrared wavelengths), at a number of wavelengths (600, 623, 643, 720 and 850 nm; band pass filters with bandwidth 22, 32, 34 nm [Semrock Inc.] and 10, 10 nm [Thorlabs] respectively). The total intensity within a ROI (20×20 pixels) around the source location for each wavelength was determined and these values normalised to the maximum value to get the IRF (Fig. 6.5). The error bars are not included in Fig. 6.5 as they are smaller than the size of the markers. The intensity was consistent across all five reflectance images taken at each wavelength.

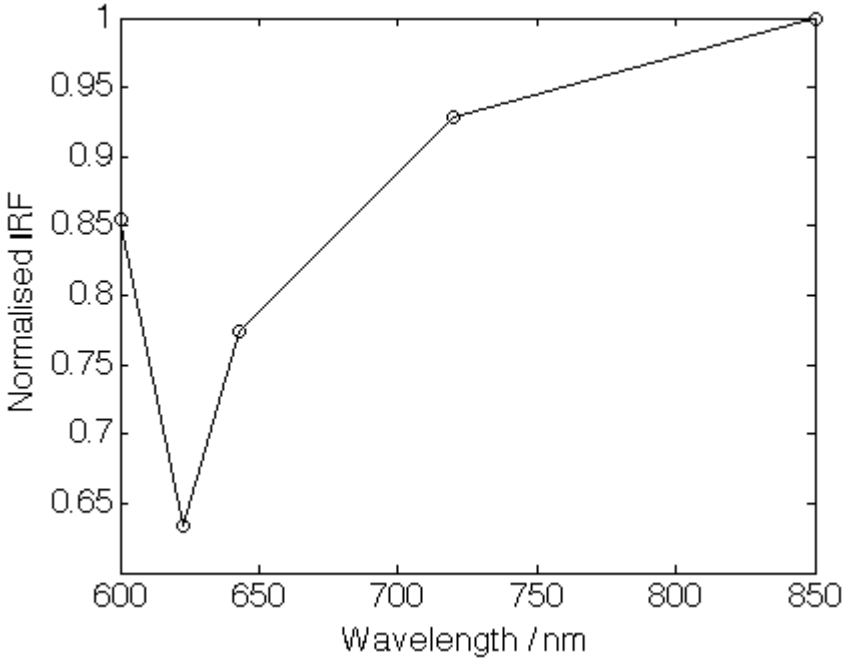

Figure 6.5: Instrument response function for DOT.

6.1.3 DOT Source Positions

The positions of the DOT sources were determined by finding the maximum intensity of images taken of each source position illuminated individually (a composite image of all sources is shown in Fig. 6.6 a). The maximum intensity position was then converted to real-space coordinates from knowledge of the pixel size from system calibration (detailed in Appendix 6 of ref. [48]) and considering the centre of the image as the origin. The calculated source positions for 643, 720 and 850 nm are shown in Fig. 6.6 b. This graph shows that there is negligible difference in the source positions between the three wavelengths, with maximum standard deviations in position of 0.09 and 0.07 mm for x and y coordinates respectively. During data analysis these positions in real-space coordinates are mapped directly onto the lower surface of the subject-specific mesh created from surface capture data for use in DOT reconstruction.

6.1.4 DOT Source Intensity Variation and Light Leakage

The relative intensity of all sources was calculated to enable the measured transmission data to be normalised to account for variations in source intensity, which is important as NIRFAST assumes all sources have equal intensity during DOT reconstruction. Fig. 6.6 c shows the relative intensity of all 15 sources at 643, 720 and 850 nm. This was calculated from the total intensity within a 40×40 pixel ROI (corresponding to 6.47×6.47 mm) around each source in the individual source images. There is up to 10% variation between the intensity of all sources for 720 and 850 nm and 20% for 643 nm. This is due to the holes drilled in the imaging platform which determine the source positions. As can be seen in Fig. 6.6 a and b the grid of sources is not regular, however, the positioning of the optical fibre underneath the imaging platform assumes a regular grid and so the fibre will not accurately line up with all of the holes introducing variation in the source intensity. Further work should be done to replace

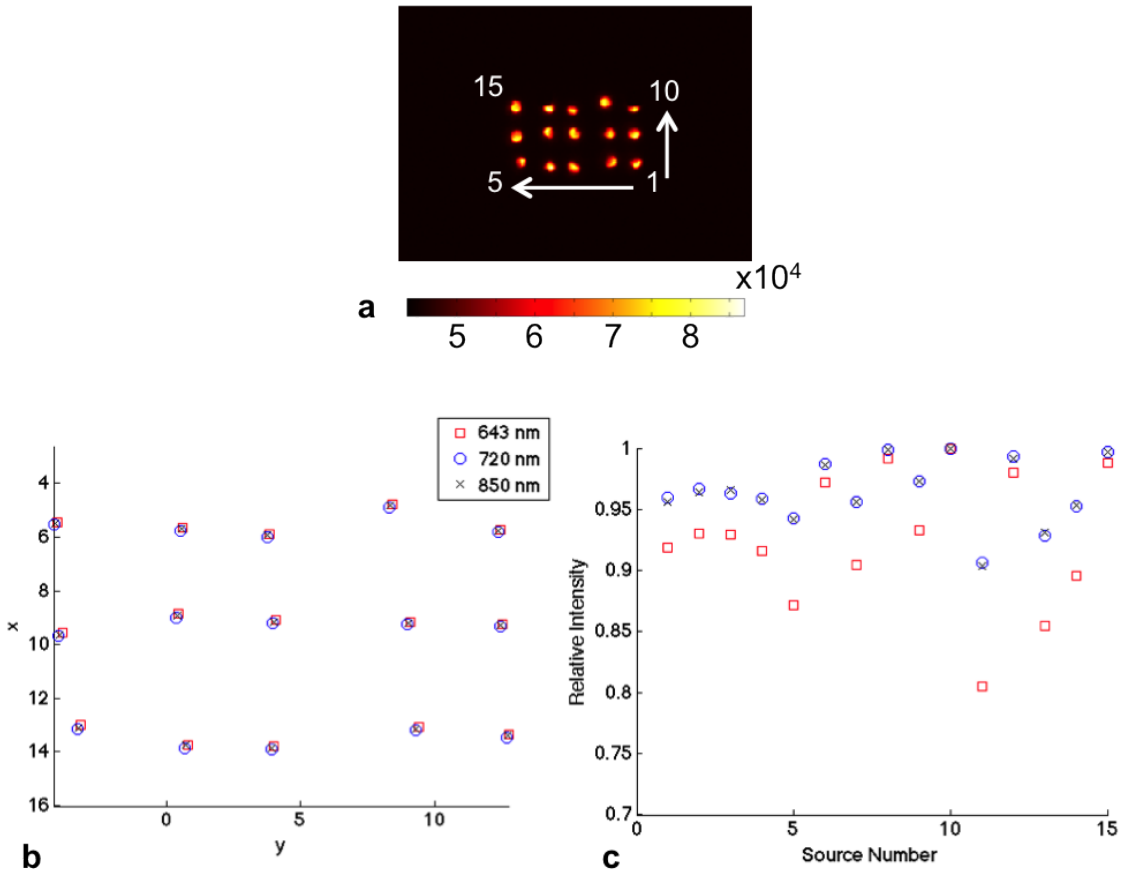

Figure 6.6: (a) All 15 DOT sources, with the number of a selection of the sources shown along with indication of the direction of movement of the source during data collection for DOT. This image is a composite of individual images taken of each source. Colourbar units: counts s^{-1}. (b) Source positions calculated from the individual source images at 643, 720 and 850 nm showing negligible variation in position with wavelength. (c) Relative intensity of all sources at the three wavelengths.

the imaging platform with a larger grid of accurately machined holes. This will reduce the variation in source intensity and increase the number of sources which are available for use, enabling source position to be customised by the user.

It was also important to determine that there was no light leakage between source positions. To do this, ROIs were constructed around all source positions (25×25 pixels corresponding to 4.04×4.04 mm) and the total intensity in all fifteen ROIs was calculated in each of the individual source images. Plots of the total ROI intensity when source 8 was illumi-

nated are shown in Fig. 6.7. It can be seen that although there is a high level of background light in the system (which could indicate that the BLDOT system is not completely light tight, or that there are sources of light within the system, which should be investigated and accounted for in the future) there is no bleed-through to the other sources, this is true when all other sources were illuminated individually. Source 8 is shown here as it is the central source, if there was any significant light leakage to any of the other sources it would be clear here. The nearest sources to source 8 are 3, 7, 9 and 13 so these would be expected to have the next highest intensity if there was any leakage, however the intensity of all source positions which aren't illuminated are constant to within 6% for 643 nm and ~2% for 720 and 850 nm indicating that there is no light leakage.

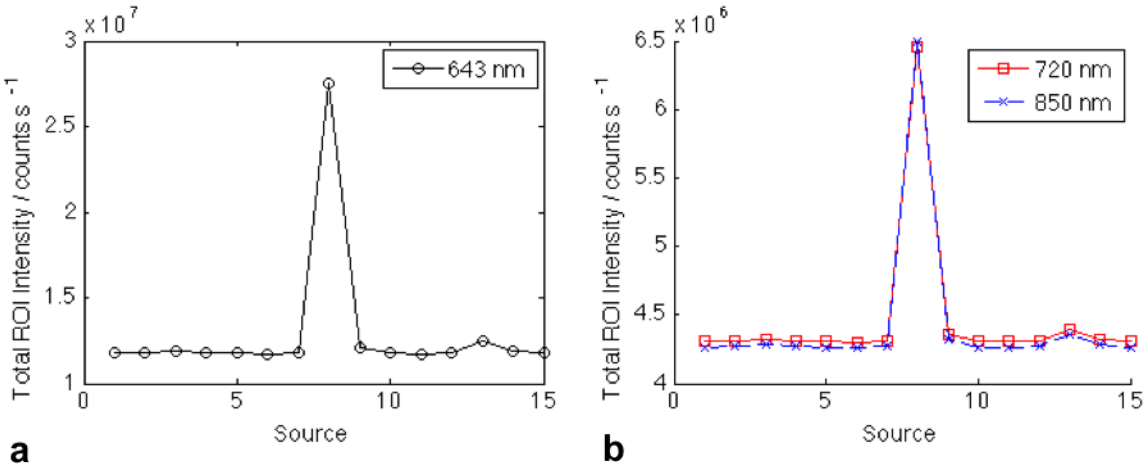

Figure 6.7: Intensity at (a) 643 nm and (b) 720 and 850 nm in ROIs encompassing the location of each DOT source (1-15) with source 8 illuminated. No bleed-through of intensity to the other source positions is seen. This is the case when all other sources are illuminated.

6.2 DOT Data Collection and Processing using the BLDOT System

This section details the method of data collection and processing in preparation for DOT optical property recovery using the reconstruction algorithms detailed in Section 5.2.1.

1. In preparation for animal data collection the animal is shaved and placed on the imaging platform covering the source positions. (If imaging a phantom, the phantom is placed directly on the imaging platform.)

2. Multi-spectral transmission data are collected from each of the fifteen source positions at 643, 720 and 850 nm using band pass filters of bandwidth 34, 10 and 10 nm respectively.

   (a) Currently the same exposure time is used for data collection for each source position, ranging from ∼0.1-1.5 s depending on animal size and light source intensity (different exposure times are used for each wavelength). These are calculated by moving the DOT illumination to a single position, capturing an image using an exposure of 0.1 s and calculating the exposure time required to collect a maximum signal of 60000 counts (the dynamic range of the camera is 65536). This exposure time calculation method needs to be optimised. Due to the shape of an animal, which is thicker nearer the centre and thinner at the edges, calculating an exposure time based on the thinner area of the animal results in low acquired signal for source positions nearer the centre of the animal. However, calculation of the exposure time based on a source nearer the centre of the animal will result in saturation of the signal acquired from the sources nearer the edges. It is therefore important to optimise both source positions and exposure time calculation, possibly with each source having a unique exposure time.

   (b) The three wavelengths chosen maximise the use of the filter wheel which has six

filter locations. 600, 623 and 643 nm are used for bioluminescence imaging, 580 nm is used for surface capture and so two positions in the filter wheel are available for DOT data collection. 720 and 850 nm have been chosen as they are either side of the isobestic point of the attenuation spectra of HbO and deoxyHb so enable the two chromophores to be distinguished.

3. Surface capture data is collected at 580 nm using a fringe projection profilometry method [83, 97]. This wavelength is always used for data collection as the relationship between the input pixel intensity (i.e. the intensity of the sinusoidal image input from the computer to the projector) and the intensity of the light output by the projector is known and the surface capture images corrected for this. See ref. [48], Appendix A.3, for more detail.

4. Data processing in preparation for DOT reconstruction:

   (a) Images are normalised by exposure time, instrument response function (Fig. 6.5) and relative source intensity (on a wavelength-by-wavelength basis, Fig. 6.6).

   (b) CCD data is mapped directly onto the surface of the mesh, which is created from surface capture data. Free space modelling is not performed for DOT data when the SD method is used for reconstruction, due to results presented in Chapter 5 which suggested that the SD method will negate the need for free space modelling and the initial data calibration step performed in NS DOT. Currently only top-view data is used, the mirrors which expand the field of view of the system are not used in DOT imaging. This is due to high intensity signal detected in the mirror views overwhelming the top view data, and so it was decided that only top view data would be used while the new DOT component of the BLDOT imaging system was optimised. Due to the curved shape of animals the top view data contains some information from the sides of the animal. In further development

of this analysis workflow the mirror data should be included to provide additional information.

(c) Source positions (Fig. 6.6 b) are added to the mesh.

(d) Detectors are added to the mesh (using the method described below) and assigned a CCD measurement.

i. A grid of points with a regular spacing of 4 mm is placed above the mesh, encompassing an area which is double the width and height of the source locations.

ii. The z coordinate of the points is decreased until they reach the surface of the mesh.

iii. The CCD image coordinates are converted to real space coordinates from knowledge of the pixel size from BLDOT system calibration (detailed in Section A.6 of ref. [48]). The detectors are assigned measurements from the pixel with corresponding real space (x, y) coordinates.

5. DOT reconstruction is performed as detailed in Chapter 5. First SD or NS region reconstructions (SDR or NSR) are performed to gain an initial homogeneous estimate of the optical properties, which are then used as an initial estimate for the full DOT reconstruction using the SD (or NS) method.

6.3 Murine DOT-BLT

This work combines the SD DOT method (presented in Chapter 5) and filter bandwidth modelling (WBW method presented in Chapter 4), validating both methods in a murine model for the first time. The following sections describe the methods used for murine data collection and analysis, followed by presentation of DOT and combined DOT-BLT results.

6.3.1 Methods

6.3.1.1 Data Collection

DOT and BLT imaging was performed on three mouse cadavers in the BLDOT system. The animals were all culled at the same time but imaged sequentially, with the total imaging time for each animal ranging from 20 to 45 minutes and total imaging time for all animals 1 hour 25 minutes. Each animal was shaved and an artificial light source (tritium-based, Trigalight Orange III; mb-microtec, Switzerland) inserted at a depth of approximately 5 mm right laterally to facilitate BLT imaging, using the method detailed in Section 3.2. As discussed in Section 3.2, the trigalight light source is not truly representative of the behaviour of bioluminescently labelled cancer cells *in vivo*, for example the artificial source is a well-defined volume and does not accurately model tumours *in vivo* which have diffuse margins where the tumour is infiltrating surrounding tissue. The intensity of the source will also be different to bioluminescently labelled cells. Specifically for BLT, which was performed on these animals, using an artificial light source (or sources) simplifies source recovery as the number of 'tumours' which are to be reconstructed is known. *In vivo* the number of sources (tumours) in an animal is unknown, it is possible that the original cluster of cells injected into the animal has dispersed and multiple tumours have grown, or metastases have developed at a different location within the animal. However, this is not a problem when using the BLDOT imaging system and associating algorithms, as the capability of recovering multiple sources simultaneously has been shown previously [48–50,97]. It would be possible in future to perform further experiments where multiple trigalight sources are inserted into the animal to represent situations *in vivo* where multiple regions of bioluminescence are present in different regions of the animal.

Following source insertion the animal was placed on the imaging platform such that the 15 DOT light sources were positioned under the abdomen as in the simulation study (Chapter

5) and transmission data were collected at 643, 720 and 850 nm (band pass filters with bandwidths 34 nm [Semrock Inc.], 10 nm and 10 nm [Thorlabs] respectively) following the method detailed in Section 6.2. The right angled mirrors were then placed on either side of the animal (without moving the animal) in preparation for BLT data collection and surface capture. The DOT light source was turned off and BLI data collected at 600, 623 and 643 nm (band pass filters with bandwidths 22, 32 and 34 nm respectively, Semrock Inc.). Surface capture data collection was then performed at 580 nm without moving the mirrors.

6.3.1.2 Data Analysis

In preparation for DOT reconstruction the data was processed as detailed in Section 6.2. To gain a homogeneous estimate of the optical properties to use in the full DOT reconstruction, the region-based reconstruction method (both NSR and SDR) was performed on the DOT data with an initial chromophore concentration of [0.1 mM, 0.1 mM, 50 %] for HbO, deoxyHb and water respectively. Note that due to data for both BLT and DOT being taken at 643 nm, the BLT image at 643 nm was subtracted from the DOT image at 643 nm to remove any BL signal from the DOT transmission data. The three dimensional chromophore distribution was then recovered using both the NS and SD methods.

Prior to tomographic BLT source recovery, free space modelling was performed on the BLI data. The CSCG method was then used to reconstruct the internal source distribution using a range of optical properties:

1. Homogeneous - Adipose: homogeneous estimate of adipose (Table 5.3).

2. Homogeneous - SDR: homogeneous estimate from the SDR reconstruction method.

3. DOT opt prop - NS - NBW: chromophore distribution recovered using the NS method, and using the NBW Jacobian in BLT reconstruction (which doesn't account for filter bandwidth, Chapter 4).

4. DOT opt prop - SD - NBW: chromophore distribution recovered using the SD method, and using the NBW Jacobian in BLT reconstruction.

5. DOT opt prop - SD - WBW: chromophore distribution recovered using the SD method, and using the WBW Jacobian in BLT reconstruction (accounting for filter bandwidth).

The aim of this work is to show the dependence of the recovered BLT source distribution on the underlying attenuation assumed in the reconstruction and to demonstrate the performance of the SD method and the WBW reconstruction method applied to a murine model for the first time. To assess the accuracy of the BLT reconstructions the x, y, z dimensions of the recovered sources (at FWHM intensity) were compared to the true dimensions of the tritium light source (1×2.5×1 mm). The depth of the recovered source and the maximum intensity were also calculated. The maximum recovered intensity was compared to the maximum intensity of the source imaged alone before implantation into the mice, at 600 nm.

6.3.2 Validation of the Spectral Derivative Method in a Murine Model

Raw transmission data for the three animals for three of the 15 DOT sources is shown in Fig. 6.8. For visualisation, the data was thresholded at 30% of the maximum. The change in appearance of the transmitted light due to the change in position of the source is demonstrated. The intensity of the transmitted light is similar for these three positions due to them having the same longitudinal (y axis) position underneath the animal, and this area of the mouse abdomen is a relatively uniform thickness. All data has a dynamic range of at least 0-1.1 $\times 10^4$ counts s^{-1}. These data (and transmission data at all other source positions) were mapped onto a three-dimensional mesh of each animal created from three-dimensional surface capture data.

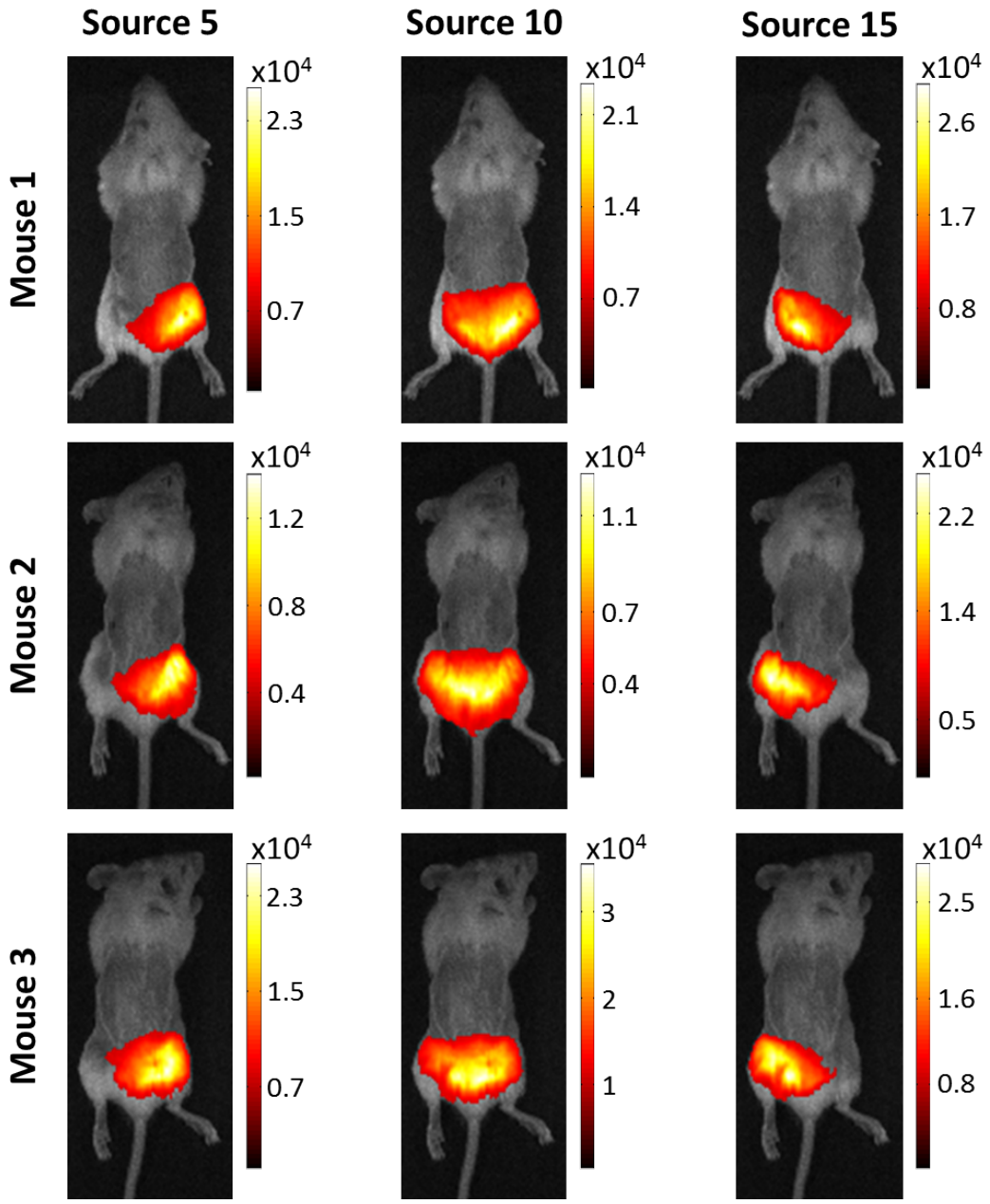

Figure 6.8: Transmission images for the three mice at 850 nm for three different source positions. For visualisation the data was thresholded at 30% of the maximum. Colourbar units: counts s^{-1}.

In order to gain an initial estimate of chromophore concentrations for use in the full DOT reconstruction, NSR and SDR methods were used. The results are shown in Table 6.1. The NSR method was unable to recover biologically relevant (i.e. comparable to the Digimouse

atlas values, Table 4.1) chromophore concentrations. If, after an iteration, the chromophore concentrations are negative, the algorithm defaults the concentration value to 0.001 mM, which is of the order of magnitude of the total haemoglobin concentration of adipose (0.0033 mM), as negative chromophore concentrations are not physically possible. This is why the recovered concentrations of HbO and deoxyHb for all mice are 0.001 mM when using the NSR algorithm.

These negative values arise due to a combination of noise in the data (for the SD method this is minimised) and the ill-posed nature of the DOT reconstruction. To reduce the ill-posedness it would be possible to introduce some structure into the volume (for NS and SD) instead of starting with a homogeneous chromophore concentration. This can be done by registering an atlas, such as the Digimouse atlas, to the mesh created from surface capture measurements and using the associated chromophore concentrations as initial estimates for the full DOT reconstruction. All reconstructions (full and region-based) would benefit from using a larger number of measurement wavelengths than the three used in this work (previous work used five wavelengths for imaging [48, 49]). This would limit the possible number of pathways taken by the light from source to detector as the path must satisfy tissue attenuation at all measurement wavelengths. Constraining the possible range of chromophore concentrations would also limit the possible number of solutions to the problem. Currently the algorithm limits the concentration of HbO and deoxyHb to non-negative values, but there is a physical range of concentrations which are present in a mouse. In the Digimouse atlas the total haemoglobin concentration ranges from 0.0033-0.3 mM [149] and the algorithm could therefore be constrained to values between 0 and 0.5 mM for example. Similarly the water content, which is currently limited to a maximum of 100%, could be constrained further, Digimouse values range from 15-85% [149]. This could also be done by applying a regularisation to the reconstruction. However, this may lead to false confidence in the results as even though the concentration values have been constrained it is not guaranteed that the

recovered values are correct.

Due to all recovered chromophore concentrations being equal to the default value of the algorithm, the NSR method was unable to produce meaningful chromophore concentrations. The recovered water content is 0% which is not biologically relevant (Digimouse soft tissues range from 50 to 85%, Table 4.1). These inaccuracies are thought to be due to the simplification of the analysis process to bypass the usual data calibration step and the inability of the NSR method to account for noise in the data.

Table 6.1: Chromophore concentrations recovered using the region based reconstruction method. Initial concentration of HbO, deoxyHb and water: 0.1 mM, 0.1 mM and 50% respectively.

Mouse	Method	HbO / mM	deoxyHb / mM	HbT / mM	StO_2 / %	Water / %
1	NSR	0.0010	0.0010	0.0020	50	0
2		0.0010	0.0010	0.0020	50	0
3		0.0010	0.0010	0.0020	50	0
1	SDR	0.0007	0.0010	0.0017	41	100
2		0.0007	0.0010	0.0017	41	81
3		0.0007	0.0010	0.0017	41	100

The SDR method also had some difficulty in recovering haemoglobin content, with deoxyHb concentrations given as the default value of 0.001 which indicates that the algorithm calculated negative values. The HbO concentration values suggest that the algorithm was able to recover some positive values. These recovered concentration values lead to a HbT concentration which is low but of the order of magnitude of 'adipose' tissue in the Digimouse atlas. The StO_2 percentage is also low but as the animals are *post mortem* this is expected. Considering the concentration values in combination with the recovered water percentages ($>$ 80 % which is comparable with the values for organs of the abdomen in the Digimouse model, Table 4.1) the SDR method has been able to recover more accurate concentrations than the NSR method, although it is difficult to estimate true values as the animals are *post mortem*.

Although the SDR method was able to recover more meaningful chromophore concentrations than the NSR method, the algorithm failed to recover positive concentrations for deoxyHb. This indicates that although the algorithm performed well in simulation in Chapter 5, it needs further validation and optimisation for experimental data. These optical properties were then used as an initial estimate for the corresponding (NS or SD) full DOT reconstruction.

The total haemoglobin distribution of the three animals recovered using both NS and SD methods are shown in Fig. 6.9. As can be seen from the colourbars, the concentration recovered using SD is much lower than that using NS for all animals. Considering the total haemoglobin content of the heterogeneous Digimouse model used in simulations in Chapter 5 (Table 5.3), this ranges from 0.0033 mM to 0.3 mM for organs in the abdomen. The murine HbT distributions recovered here using the SD method are within the Digimouse range but the NS properties are approximately 3-7× the maximum HbT in the Digimouse atlas.

It is clear that none of the distributions are anatomically correct. The recovered chromophore distribution for simulated Digimouse data showed the underlying anatomy (see Fig.'s 5.9 and 5.10), in particular the kidneys, but these can't be seen in the murine data. The NS recovered HbT distribution for all animals was localised to the base of the animal, at the source positions. This, along with the inaccuracy in the recovered concentration values for HbT, suggests that the NS method is unable to be used without prior implementation of the data calibration procedure described in ref. [194]. The SD chromophore distribution for all animals was localised within the animal, with the highest concentration in the centre of the animal but with diffuse regions of chromophore surrounding this region. This is not anatomically correct but the position of the HbT localisation is improved and the accuracy of the concentration values is increased, when compared to the NS recovered values. The SD method has been able to account for noise in the data, and with further refinement may be a good alternative to the NS method (which must be combined with the data calibration pro-

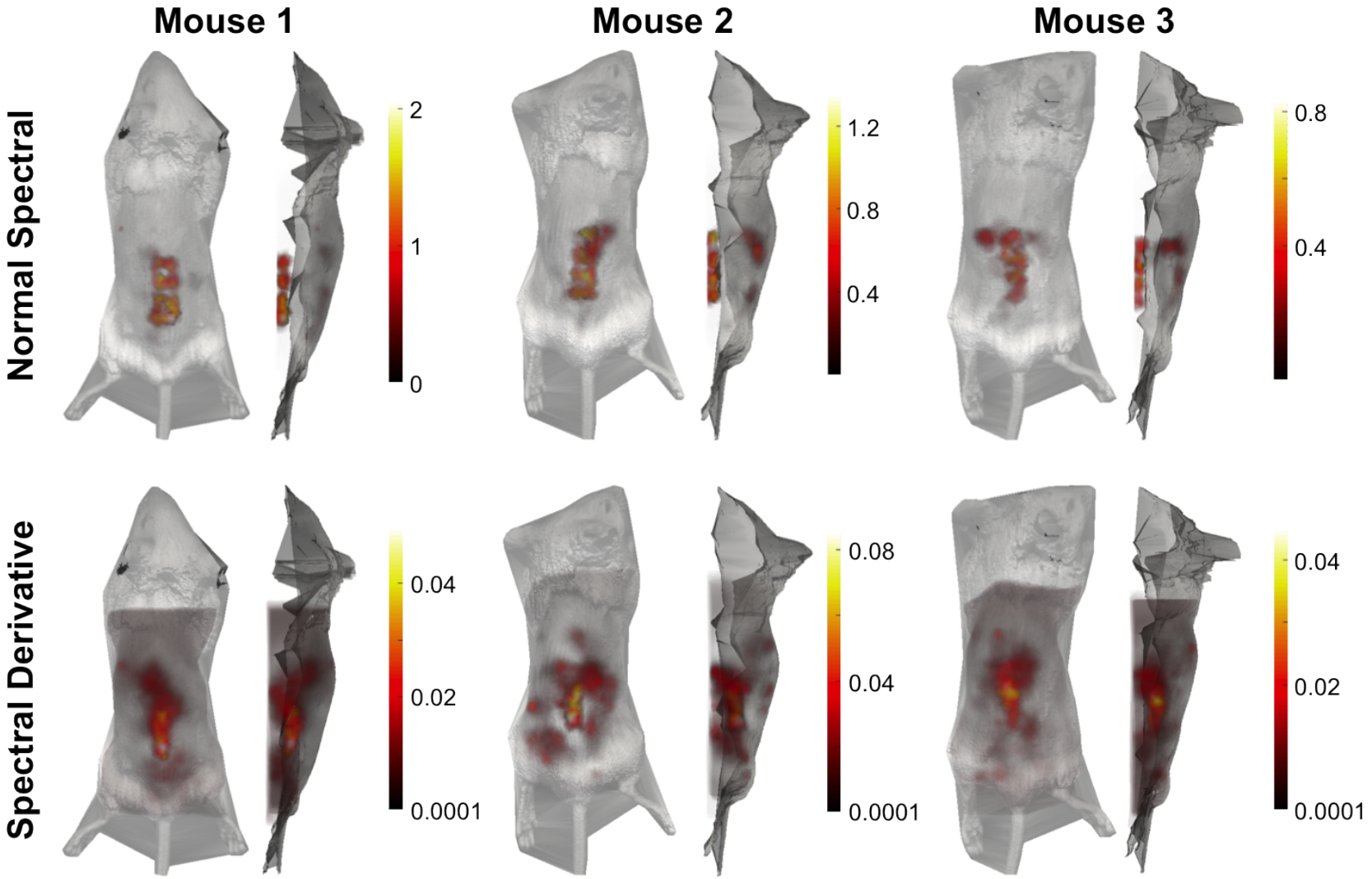

Figure 6.9: Full DOT reconstructions of HbT for mice 1-3 using NS and SD methods. The NS recovered distribution is localised mainly to the source locations on the base of the animal, so hasn't dealt with the noise in the experimental data, the concentration values are extremely high compared to the values in the Digimouse atlas. The SD recovered distribution of HbT is more central in the animal and has more biologically relevant concentration values. More refinement of the model is required to gain biologically relevant distributions. Colourbar units: mM.

cedure). Remaining error in the recovered source distribution may be due to the assumption that noise in the data is constant across adjacent measurement wavelengths and that this noise is multiplicative (Section 5.2.1.1) being incorrect. Work in Chapter 5 demonstrated this assumption to be appropriate for simulation data, but it is possible that non-multiplicative noise is present in experimental data. The effect and cause of this non-multiplicative noise must be considered in future work on the SD method, but these initial results are promising once the method has been optimised for experimental data.

To test these DOT recovered chromophore distributions further, they were used as prior knowledge for BLT source recovery for all animals.

6.3.3 Combined DOT-BLT

Raw and corrected (using the free space model) BLI data at 600 nm is shown in Fig. 6.10. The intensity of the BLI data decreases from mouse 1-3, with the corrected BLI data for mouse 3 being an order of magnitude less intense than that for mice 1 and 2. This variation in intensity could be due to differing depths of the artificial sources, or due to the increase in time since the animals were culled causing differing tissue attenuation. Fig. 5.3 b shows the variation in transmitted light intensity over time after death for an animal with a light source under the lower abdomen, in a similar location to the position of the artificial light sources inserted into these animals, showing that the attenuation increases with time. Mouse 3 was imaged at the longest time after death of the three animals, and so the tissue attenuation is thought to be high, which explains the low BLI signal acquired. The corrected BLI data was then used with a range of different optical properties, as detailed in Section 6.3.1.2, to recover the internal distribution of the bioluminescent source. Note that due to the low BLI signal acquired for mouse 3, the BLT source recovery is not expected to perform well.

The recovered bioluminescent source distribution for mice 1-3 at full width half maximum (FWHM) intensity, along with a table showing the x, y, z dimensions of the source, are shown

in Fig.'s 6.11, 6.12 and 6.13 respectively. For all animals the differing appearance in recovered source distribution with the different optical properties can be seen. The homogeneous estimates (adipose and the SDR reconstruction) recover the largest source distribution, most prominently for mouse 1. Qualitatively, the source recovered using NS recovered optical properties, using the NBW Jacobian model (i.e. the bandwidth of filters are ignored; 'DOT opt prop - NS - NBW') for mouse 1 appears disjointed and more diffuse than that recovered using the SD recovered optical properties (using both NBW and WBW Jacobian models). For mouse 2 this source appears small, and for mouse 3, appears as two regions of bioluminescence.

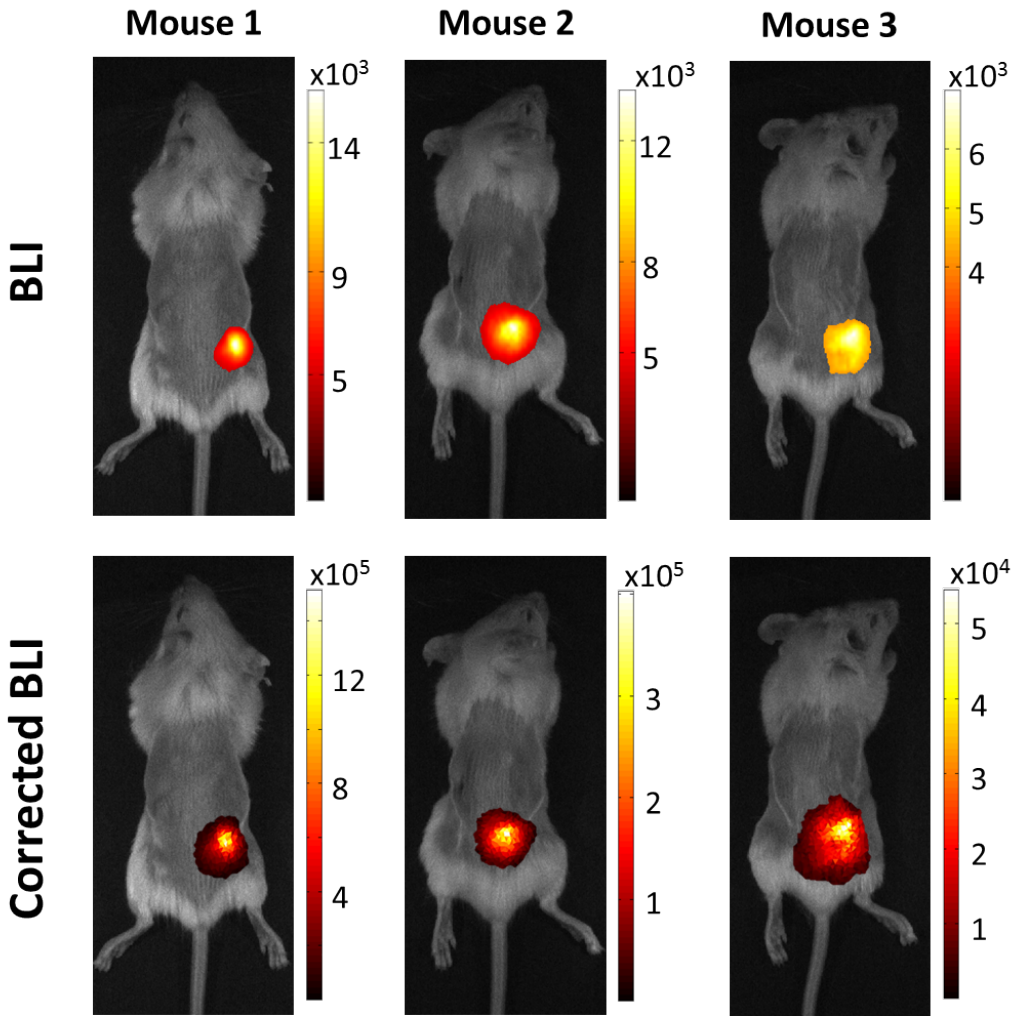

Figure 6.10: Raw and corrected BLI of the three mice at 600 nm. Colourbar units: BLI - counts s^{-1}, corrected BLI - arbitrary intensity units.

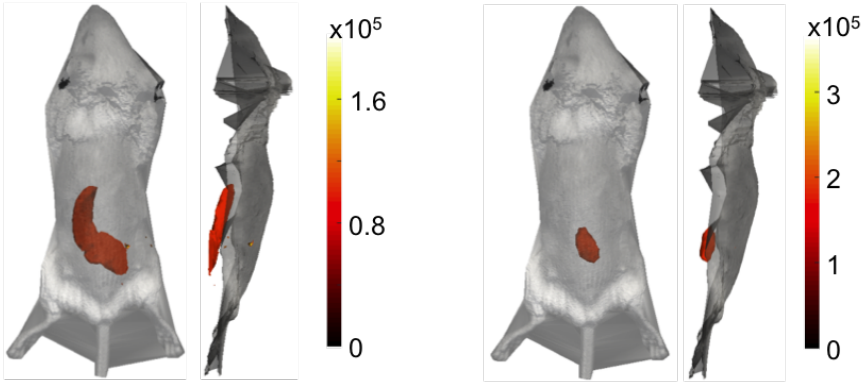

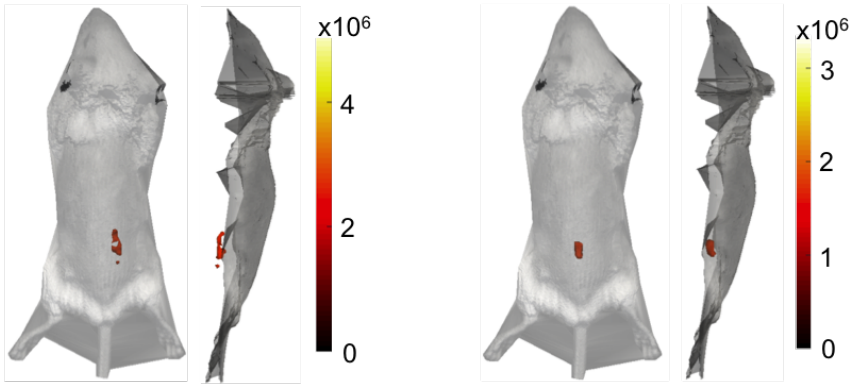

	x	y	z
1	19.68	24.50	10.82
2	7.83	7.50	8.66
3	5.69	7.92	9.10
4	0.53	2.41	1.34
5	2.42	5.41	2.39
Target	***1***	***2.5***	***1***

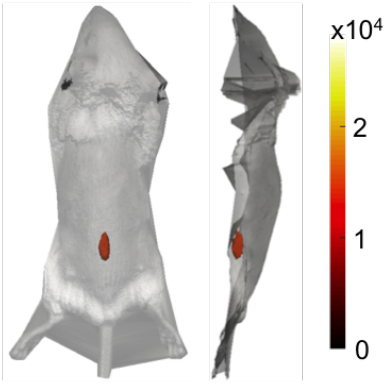

Figure 6.11: Mouse 1 BLT reconstructions (FWHM) using different optical properties. The table shows the dimensions of the recovered sources, with the target source dimensions indicated. The sources recovered using homogeneous estimates of the optical properties are much more diffuse than the DOT determined optical properties. Colourbar units: arbitrary intensity units.

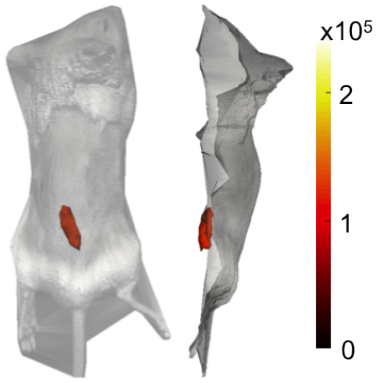

1. Homogeneous – Adipose

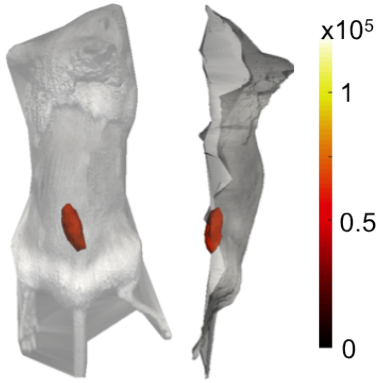

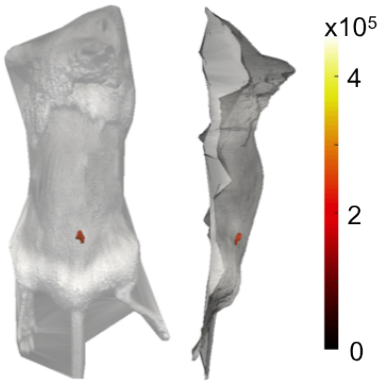

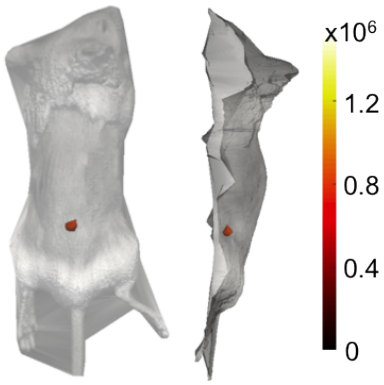

	x	y	z
1	3.89	9.49	2.53
2	5.40	5.60	3.99
3	0.89	2.33	0.91
4	1.63	1.74	0.22
5	1.88	0.22	0.25
Target	***1***	***2.5***	***1***

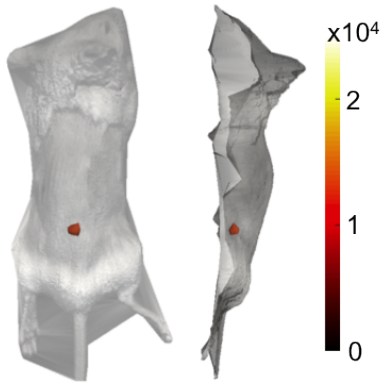

Figure 6.12: Mouse 2 BLT reconstructions (FWHM) using different optical properties. The table shows the dimensions of the recovered sources, with the target source dimensions indicated. The sources recovered using homogeneous estimates of the optical properties are more diffuse than the DOT determined optical properties. Colourbar units: arbitrary intensity units.

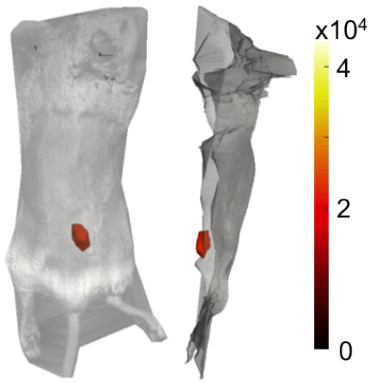

1. Homogeneous – Adipose

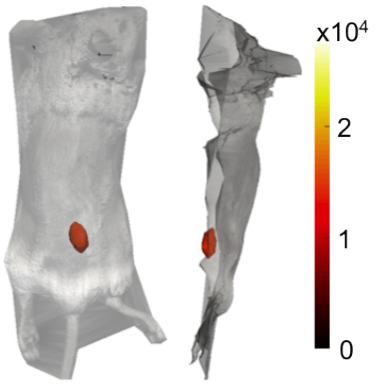

2. Homogeneous – SDR

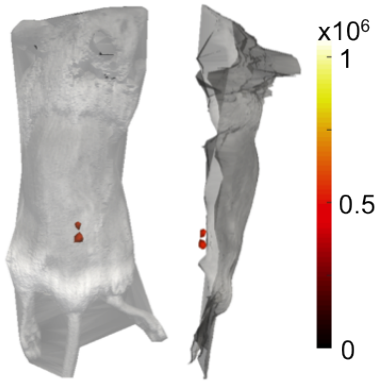

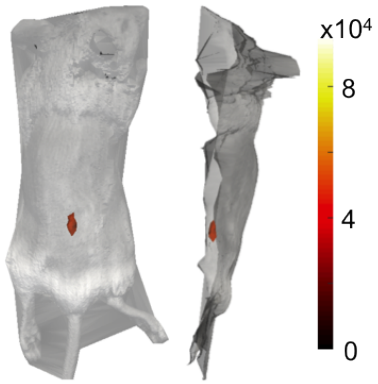

	x	y	z
1	4.00	5.85	2.51
2	4.18	6.25	3.00
3	0.39	3.23	0.13
4	1.27	3.85	0.88
5	1.99	3.85	0.88
Target	***1***	***2.5***	***1***

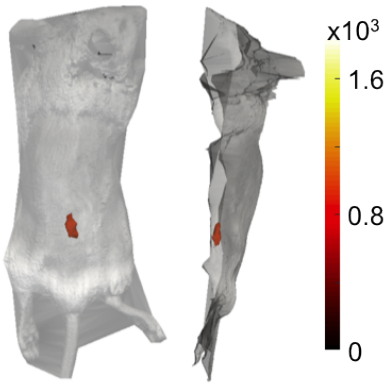

Figure 6.13: Mouse 3 BLT reconstructions (FWHM) using different optical properties. The table shows the dimensions of the recovered sources, with the target source dimensions indicated. The sources recovered using homogeneous estimates of the optical properties are more diffuse than the DOT determined optical properties. Colourbar units: arbitrary intensity units.

Table 6.2: Maximum recovered bioluminescence intensity for the five different optical properties and mice 1-3. The target values are maximum intensity values determined from images of the sources before insertion into the animals at 600 nm.

Optical Properties	Mouse 1	Mouse 2	Mouse 3
1. Homogeneous - Adipose	2.0×10^5	2.4×10^5	4.4×10^4
2. Homogeneous - SD region recon	3.6×10^5	1.2×10^5	2.8×10^4
3. DOT opt prop - NS - NBW	5.2×10^6	4.6×10^5	1.1×10^6
4. DOT opt prop - SD - NBW	3.3×10^6	1.5×10^6	9.4×10^4
5. DOT opt prop - SD - WBW	$\mathbf{2.8 \times 10^4}$	$\mathbf{2.5 \times 10^4}$	1.8×10^3
Target	$\mathbf{6.4 \times 10^4}$	$\mathbf{6.2 \times 10^4}$	$\mathbf{6.2 \times 10^4}$

This supports the findings in Section 6.3.2, that the NS recovered optical properties are inaccurate. For all three mice, the sources recovered using SD recovered optical properties with both NBW and WBW Jacobian methods are visually similar, supported by the similarity in the dimensions of the recovered source.

Quantitatively, the depth of the recovered source varies depending on the optical properties used (Fig. 6.14 top row), supporting the data shown in Fig. 5.1 and Table 5.1. For all animals, the source was inserted at approximately 5 mm. The sources recovered at the closest depth to 5 mm are the sources recovered using SD calculated chromophore distributions, with the NBW and WBW methods both producing very similar source depths, supporting previous findings for the filter bandwidth model (see Chapter 4 and ref. [96]). Considering the maximum intensity of the recovered sources (Fig. 6.14 bottom row), in comparison to the value measured for each artificial source individually, the source recovered using SD optical properties and the WBW Jacobian is closest to the true intensity for mice 1 and 2 (Table 6.2). As the true intensity was measured at 600 nm only and three wavelengths were used in the BLT reconstruction, the maximum intensity of the recovered source is not expected to be exactly the same intensity but of the same order of magnitude. Mouse 3 recovers a lower intensity, this is thought to be due to the poor BLI data, showing that even when subject-specific optical properties determined through DOT measurements are used in BLT

reconstructions, the quality of the BLI data is important for the quantitative accuracy of BLT.

All sources recovered using all other optical properties were one or two orders of magnitude higher than the target intensity. As can be seen in Fig. 6.14, the bioluminescent source recovered using the NBW model and either NS or SD determined DOT optical properties have the highest intensity, which is approximately two orders of magnitude larger than the measured value. This is most likely due to the use of the NBW Jacobian in the BLT reconstruction and is consistent with the high intensity recovered sources using the NBW method in Chapter 4.

This further validates the SD method as a potentially viable method for performing DOT source recovery without the need for either free space modelling or the data calibration which is used with the NS method. The WBW method for BLT source recovery is also shown to be effective in improving the quantitative accuracy of BLT when applied to a murine model.

6.4 Conclusions

This chapter has detailed modifications made to the BLDOT imaging system in preparation for DOT imaging of a murine model. The updated DOT system was used to image three mice *post mortem* and demonstrate the improved efficacy of the SD method over the NS method in a murine model, although anatomically accurate chromophore distributions were not returned in either case. Remaining inaccuracy in the recovered SD DOT chromophore distributions could be due to the bandwidth of the filters used for data collection being ignored in the reconstruction. Chapter 4 demonstrated the importance of accounting for the bandwidth of the filters when considering the quantitative accuracy of BLT, so developments should be made to the DOT reconstruction to account for the filter bandwidth as the quantitative accuracy of recovered chromophore distribution is likely to increase. Chapter 5 demonstrated

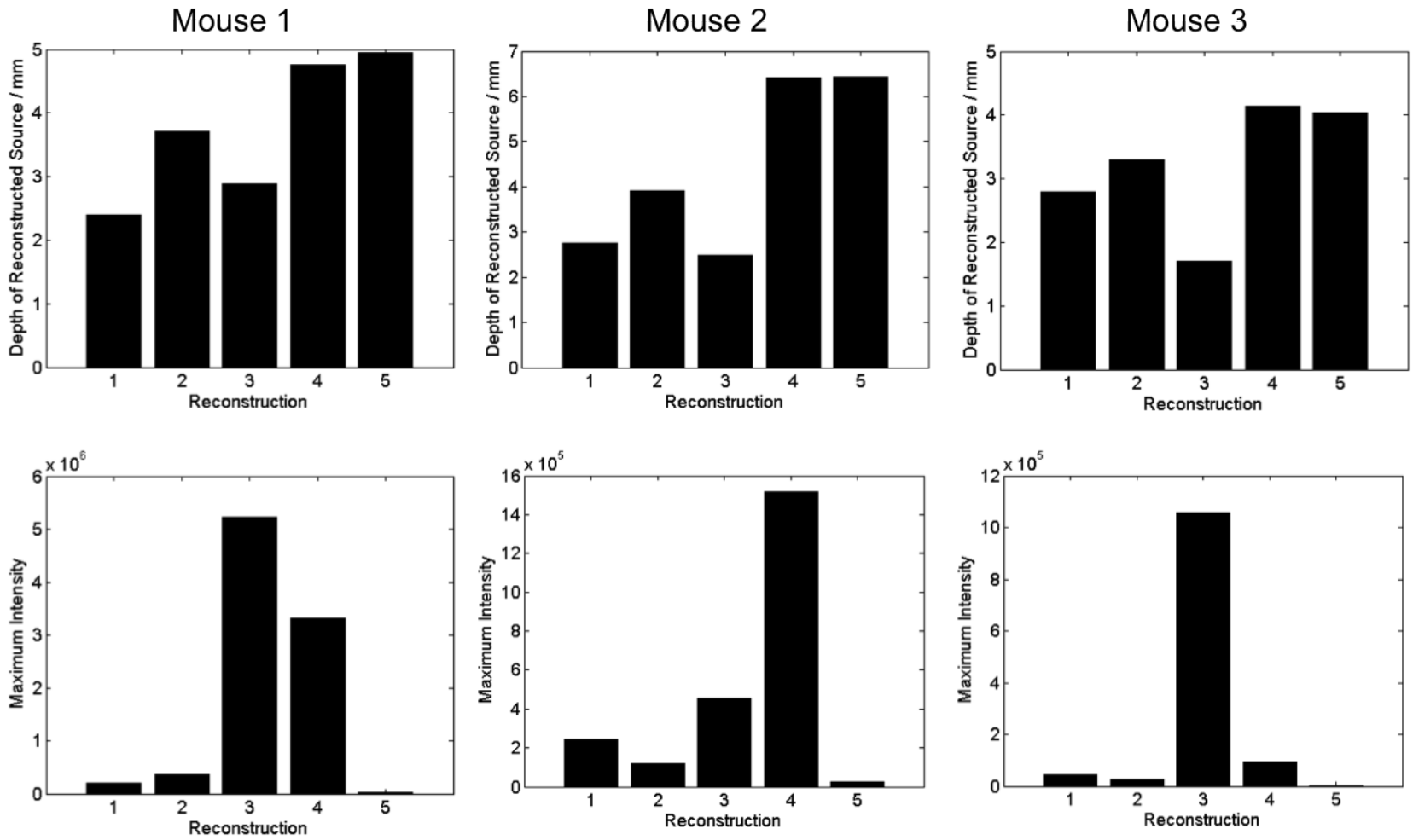

Figure 6.14: Depth (top row) and maximum intensity (bottom row) of recovered sources for mice 1-3. There is a variation of both metrics with optical properties assumed in the reconstruction, with the SD recovered optical properties producing the most accurate depth and maximum intensity in all animals.

the capability of the SD method via simulation using a heterogeneous mouse model but the data was simulated at a single wavelength, ignoring filter bandwidth. Future work should determine the effect of filter bandwidth on the recovered chromophore distributions and account for bandwidth in the reconstruction algorithm. Inaccuracies could also be due to only three wavelengths being used for data collection, and with a large spacing between wavelengths. Previous work on the spectral derivative method applied to a contact imaging system showed the method to be effective when using data at 100 wavelengths with 2 nm spacing [200]. Using a larger number of wavelengths in analysis may increase the quantitative accuracy of the SD method when applied to a non-contact imaging system such as the BLDOT system, but this would increase the total imaging time. Performing measurements on phantoms with known optical properties to optimise measurement wavelengths and data analysis procedures for the SD method applied to a non-contact imaging system will prove useful in further development of this technique.

The results presented here are promising for the potential of the SD model in performing both DOT and combined DOT-BLT imaging in murine models *in vivo,* although further work is required to optimise the efficacy of the SD method before moving into *in vivo* work. Combining DOT and BLT has been shown to enhance the quantitative accuracy of BLT, with the highest quantitative accuracy results obtained when using the SD method combined with the WBW method for BLT reconstruction. This suggests that, once optimised, the SD method may provide a large impact on the quantitative accuracy of BLT. Work in this chapter also demonstrated the importance of using good quality multi-spectral BLI data when performing DOT-BLT. This work has validated the SD method and WBW model for the first time in a murine model, demonstrating the efficacy of the two techniques in enhancing the quantitative accuracy of BLT.

Chapter 7

Conclusions and Further Work

Bioluminescence imaging is widely used in pre-clinical research, but there remain limitations to the quantitative accuracy achievable by the technique. Bioluminescence tomography provides three-dimensional tomographic information about the bioluminescent source distribution. However, BLT is rarely used in pre-clinical studies despite the advantages over BLI in the ability to use orthotopic models, where tumour development can be monitored in the correct biological location within the animal, for example. There also remain limitations to the quantitative accuracy of BLT. This work aimed to enhance the quantitative accuracy of BLI and BLT through hardware and software developments to an existing developmental imaging system, the BLDOT system.

BLI measurements are highly dependent on the position of the animal, with a small change in position affecting the measurement. This can lead to incorrect conclusions being drawn during pre-clinical experiments about the rate of tumour growth or response to treatment, for example. Previous work has shown a free space model [27] to be effective in accounting for positional changes of a cylindrical phantom. The work presented here built on previous work by applying the model to murine BLI data taken from *post mortem* animals with artificial sources inserted, and imaged in two different positions in the BLDOT system. The free space

model was able to improve the quantitative accuracy of the BLI measurements, however this improvement was limited by changes in the tissue attenuation of the animals over the course of data collection due to the time after death of the animals increasing. The results were promising but the model must be validated both in more controlled *post mortem* experiments with consistent source depth, rotation angles and time after death, and *in vivo* before routine use in pre-clinical research.

Previously the bandwidth of the filters used for multi-spectral data collection for BLT was ignored (using the NBW model), with all data assumed to be collected at the central wavelength of the band pass filter. However, when using band pass filters, data collected encompass the range of wavelengths transmitted through the filter, which is governed by the bandwidth. Not accounting for the filter bandwidth in the BLT reconstruction ignores the spectral attenuation of tissue and the spectral source emission, resulting in a model-data mismatch when performing model-based image recovery. Increasing the bandwidth of the filters increases this model-data mismatch, resulting in a dependence of the recovered bioluminescent source intensity on the bandwidth of the filters. The WBW model was proposed as a method of accounting for filter bandwidth in the BLT reconstruction. Simulation (using the heterogeneous Digimouse atlas) and experimental data (using the XPM2 mouse shaped phantom) showed the WBW model to be effective in removing the dependence of recovered bioluminescence intensity on filter bandwidth, improving the quantitative accuracy of BLT. The model was also shown to improve the quantitative accuracy of BLT in a *post mortem* murine model. Future work with the WBW model should include optimisation of Jacobian calculation to minimise the increase in data processing time as compared to NBW reconstruction, inclusion of filter transmission profile in the WBW model and validation of the WBW model *in vivo*.

The BLT data presented in the filter bandwidth modelling study used multi-spectral bioluminescence data at only three wavelengths (rather than five or six which were used

previously in the BLDOT system). This, combined with data acquisition using wider bandwidth filters (increasing to ∼20 nm from 10 nm), resulted in a reduction in data acquisition time by $\frac{2}{3}$ when considering the BLDOT system. Simulation data, using a heterogeneous mouse atlas, and experimental data, using the XPM2 mouse shaped phantom in the BLDOT system, showed that the decrease in measurement wavelengths did not detrimentally effect the quantitative accuracy of the recovered source in BLT. This is provided that the WBW model is used to account for the bandwidth of the filters used for data collection and that the measurement wavelengths are chosen by consulting the spectral attenuation of tissue and emission spectrum of the bioluminescent source, with optimum measurement wavelengths when the source emission is high and tissue attenuation low. Due to this work involving a variation in both the number of wavelengths used for data collection and the spectral range of these measurement wavelengths, in the future it is important to determine the effect of spectral range of measurement wavelengths on the quantitative accuracy of BLT. The work must also be repeated in order to produce statistically significant results.

These modifications to the data collection and analysis process were shown to improve the quantitative accuracy of BLT when applied to simulation and phantom experiments, but must be validated *in vivo* if they are to be used routinely in pre-clinical research.

The above work involved use of models and phantoms which had well characterised optical properties. However, in pre-clinical BLT using a murine model the optical properties of the animal are unknown and in order to perform quantitatively accurate BLT, accurate knowledge of these properties is vital. A spectral derivative DOT method was presented as a method of calculating subject-specific optical properties for use in BLT and validated using the heterogeneous Digimouse atlas via simulation. The SD method was found to be more robust to noise in the data than the traditionally used NS method, particularly when considering angular noise in the data which is currently accounted for during free space analysis. This suggests that the SD method can bypass the need for the free space model in

analysis of DOT data. When using the DOT-derived optical properties as prior knowledge for use in BLT reconstructions of the Digimouse model, the recovered bioluminescent source distribution when using the SD derived optical properties was quantitatively comparable to the true bioluminescent source distribution.

Validation of the SD method was performed on a *post mortem* murine model by taking DOT measurements using the BLDOT system and then using the DOT data as prior knowledge for BLT source recovery, as with the simulation study. Modifications were made to the existing DOT component of the BLDOT system to maximise the achievable intensity of the DOT sources, minimising the exposure times required to collect transmission data at each source position. Supporting the simulation conclusions, the SD method performed superiorly to the NS method. However, the quantitative accuracy of the recovered optical property distribution was limited. The appearance of the distributions was not anatomically accurate but the results were promising for this first validation of the method experimentally. When used as prior knowledge for BLT source recovery, the SD optical property distribution enabled bioluminescent source recovery of a higher degree of quantitative accuracy than that achievable using NS determined optical properties or a homogeneous estimate. The results for this first application of the SD method in a murine model suggest that when applied *in vivo* the method may enhance the quantitative accuracy of BLT, however, further work is required to consider the effect of non-multiplicative noise. This experiment included validation of the WBW Jacobian model, with the bioluminescent source distribution with the highest quantitative accuracy recovered using a combination of SD determined optical properties and the WBW Jacobian model. This is an encouraging result, suggesting that the use of the SD method and WBW models complement each other and will enhance the quantitative accuracy of BLT in *in vivo* pre-clinical research.

Due to the remaining inaccuracy in the optical property distribution recovered using the SD method, imaging of phantoms with known optical property distributions should be done

in order to optimise the number of wavelengths used for data collection and the position and number of DOT sources to use (this work used 15 sources in a 3×5 grid with 4 mm spacing). Previous work has shown a SD method, when applied to a contact imaging system, to be effective experimentally when 100 measurement wavelengths, with 2 nm spectral spacing, were used. This work used three wavelengths, with a spectral spacing of >75 nm. The SD method is based on the assumption that noise present in the data is constant at adjacent measurement wavelengths and therefore will cancel out. Further work should be done to ensure that the assumption that noise contributions remain constant between measurement conducted under the same experimental conditions is valid, and to optimise the wavelengths which are used for data collection. Additionally, scatter should be included in the reconstruction. This work assumed the scatter was known and only reconstructed chromophore concentrations, which may account for some inaccuracy still present in the murine data presented in Chapter 6.

The DOT reconstructions in this work do not account for the bandwidth of the filters used for data collection. As shown by the increase in quantitative accuracy for BLT when using the WBW model, incorporation of filter bandwidth modelling into model-based recovery is important when using band pass filters for data collection. DOT data collection also uses band pass filters and so future work on DOT optical property recovery should incorporate filter bandwidth into the model-based reconstruction algorithm. This will likely improve the quantitative accuracy of the technique.

A large proportion of the future work required to develop this work further, is to apply many of the algorithms *in vivo*. In preparation for *in vivo* work the BLDOT imaging system requires some modification to incorporate a heated imaging platform for temperature regulation of the animals during imaging, and addition of an anaesthesia system for induction and maintenance of anaesthesia.

The work in this thesis has been shown to improve the quantitative accuracy of BLI,

through validation of the free space model in a murine environment, and BLT through incorporation of filter bandwidth modelling into the source reconstruction and use of a SD DOT reconstruction method to obtain a subject-specific optical property distribution for use in BLT. Further work is required to optimise the capability of the methods, and validation *in vivo* is vital, but the results presented here are encouraging for increasing the future use of BLT in pre-clinical studies.

Bibliography

[1] D. E. Jenkins, Y. Oei, Y. S. Hornig, S.-F. Yu, J. Dusich, T. Purchio, and P. R. Contag. Bioluminescent imaging (BLI) to improve and refine traditional murine models of tumor growth and metastasis. *Clinical & Experimental Metastasis*, 20:733–744, 2003.

[2] C. H. Contag and M. H. Bachmann. Advances in *in vivo* bioluminescence imaging of gene expression. *Annu. Rev. Biomed. Eng.*, 4:235–60, 2002.

[3] Lorenzo, Jorge Ripoll. *Principles of Diffuse Light Propagation: Light Propagation in Tissues with Applications in Biology and Medicine*. World Scientific Publishing Co., 2012.

[4] K. O'Neill, S. K. Lyons, W. M. Gallagher, K. M. Curran, and A. T. Byrne. Bioluminescent imaging: a critical tool in pre-clinical oncology research. *Journal of Pathology*, 220:317–327, 2010.

[5] E. H. White, E. Rapaport, H. H. Seliger, and T. A. Hopkins. The chemi- and bioluminescence of firefly luciferin: An efficient chemical production of electronically excited states. *Bioorganic Chemistry*, 1:92–122, 1971.

[6] C. Bolin, C. Sutherland, K. Tawara, J. Moselhy, and C. L. Jorcyk. Novel mouse mammary cell lines for *in vivo* bioluminescence imaging (BLI) of bone metastasis. *Biological Procedures Online*, 14, 2012.

[7] D. M. Barrett, A. E. Seif, C. Carpenito, D. T. Teachey, J. D. Fish, C. H. June, S. A. Grupp, and G. S. D. Reid. Noninvasive bioluminescent imaging of primary patient acute lymphoblastic leukemia: a strategy for preclinical modelling. *Blood*, 118:e112–e117, 2011.

[8] D. E. Jenkins, Y. S. Hornig, Y. Oei, J. Dusich, and T. Purchio. Bioluminescent human breast cancer cell lines that permit rapid and sensitive *in vivo* detection of mammary tumors and multiple metastases in immune deficient mice. *Breast Cancer Research*, 7:R444–R454, 2005.

[9] Y.-P. Sher, C.-M. Chang, C.-G. Juo, C.-T. Chen, J. L. Hsu, C.-Y. Lin, Z. Han, S.-G. Shiah, and M.-C. Hung. Targeted endostatin-cytosine deaminase fusion gene therapy plus 5-fluorocytosine suppresses ovarian tumour growth. *Oncogene*, 32:1082–1090, 2013.

[10] P. Ru, R. Steele, P. Newhall, N. J. Phillips, K. Toth, and R. B. Ray. miRNA-29b suppresses prostate cancer metastases by regulating epithelial-mesenchymal transition signaling. *Molecular Cancer Therapeutics*, 11:1166–1173, 2012.

[11] A. B. Kunnumakkara, S. Guha, S. Krishnan, P. Diagaradjane, J. Gelovani, and B. B. Aggarwal. Curcumin potentiates antitumor activity of gemcitabine in an orthotopic model of pancreatic cancer through suppression of proliferation, angiogenesis, and inhibition of nuclear factor-kB-regulated gene products. *Cancer Res*, 67:3853–3861, 2007.

[12] B. A. Rabinovich, Y. Ye, T. Etto, J. Q. Chen, H. I. Levitsky, W. W. Overwijk, L. J. N. Cooper, J. Gelovani, and P. Hwu. Visuavisual fewer than 10 mouse T cells with an enhanced firefly luciferase in immunocompetent mouse models of cancer. *PNAS*, 105:14342–14346, 2008.

[13] N. F. Huang, J. Okogbaa, A. Babakhanyan, and J. P. Cooke. Bioluminescence imaging of stem cell-based therapeutics for vascular regeneration. *Theranostics*, 2:346–354, 2012.

[14] A. Sacco, R. Doyonnas, P. Kraft, S. Vitorovic, and H. M. Blau. Self-renewal and expansion of single transplanted muscle stem cells. *Nature*, 456:502–506, 2008.

[15] X. Wang, M. Rosol, S. Ge, D. Peterson, H. McNamara, G. amd Pollack, D. B. Kohn, M. D. Nelson, and G. M. Crooks. Dynamic tracking of human hematopoietic stem cell engraftment using *in vivo* bioluminescence imaging. *Blood*, 102, 2003.

[16] J. Hardy, M. Edinger, M. H. Bachmann, R. S. Negrin, C. G. Fathman, and C. H. Contag. Bioluminescence imaging of lymphocyte trafficking *in vivo*. *Experimental Hematology*, 29:1353–1360, 2001.

[17] O. Ibrahim-Granet, G. Jouvion, T. M. Hohl, S. Droin-Bergere, F. Philippart, O. Y. Kim, M. Adib-Conquy, R. Schwendener, J-M. Cavaillon, and M. Brock. *In vivo* bioluminescence imaging and histopathologic analysis reveal distinct roles for resident and recruited immune effector cells in defense against invasive aspergillosis. *BMC Microbiology*, 10, 2010.

[18] C. H. Contag, P. R. Contag, J. I. Mullins, S. D. Spilman, D. K. Stevenson, and D. A. Benaron. Photonic detection of bacterial pathogens in living hosts. *Molecular Microbiology*, 18:593–603, 1995.

[19] T. C. Doyle, S. M. Burns, and C. H. Contag. *In vivo* bioluminescence imaging for integrated studies of infection. *Cellular Microbiology*, 6:303–317, 2004.

[20] T. N. Demidova, F. Gad, T. Zahra, K. P. Francis, and M. R. Hamblin. Monitoring photodynamic therapy of localized infections by bioluminescence imaging of genetically

engineered bacteria. *Journal of Photochemistry and Photobiology B: Biology*, 81:15–25, 2005.

[21] T. Chuzel, V. Sanchez, M. Vandamme, S. Martin, O. Flety, A. Pager, C. Chabanel, L. Magnier, M. Foskolos, O. Petit, B. Rokbi, and E. Chereul. Impact of anesthesia protocols on *in vivo* bioluminescent bacteria imaging results. *PLoS ONE*, 10:e0134048, 2015.

[22] A. A. Murphy, P. C. Rosato, Z. M. Parker, A. Khalenkov, and D. A. Leib. Synergistic control of herpes simplex virus pathogenesis by IRF-3, and IRF-7 revealed through non-invasive bioluminescence imaging. *Virology*, 444:71–79, 2013.

[23] K. E. Luker and G. D. Luker. Applications of bioluminescence imaging to antiviral research and therapy: Multiple luciferase enzymes and quantitation. *Antiviral Research*, 78:179–187, 2008.

[24] M. Dobbs, D. Hughes, J. Narahari, J. Choi, G. Los, and B. Webb. Simultaneous dual-emission detection of luciferase reporter assays. *BMG LABTECH Application Note*, 233, 2013.

[25] H. Zhao, T. C. Doyle, O. Coquoz, F. Kalish, B. W. Rice, and C. H. Contag. Emission spectra of bioluminescent reporters and interaction with mammalian tissue determine the sensitivity of detection *in vivo*. *Journal of Biomedical Optics*, 10, 2005.

[26] H. Dehghani, S. C. Davis, and B. W. Pogue. Spectrally resolved bioluminescence tomography using the reciprocity approach. *Med. Phys.*, 35:4863–4871, 2008.

[27] J. A. Guggenheim, H. R. A. Basevi, I. B. Styles, J. Frampton, and H. Dehghani. Quantitative surface radiance mapping using multiview images of light-emitting turbid media. *J. Opt. Soc. Am. A*, 30:2572–2584, 2013.

[28] S. L. Taylor, J. A. Guggenheim, I. B. Styles, M. Carvalho-Gaspar, M. Cobbold, and H. Dehghani. Importance of free space modelling on quantitative non-contact imaging. In *Biomedical Optics 2014*, page BM3A.46. Optical Society of America, 2014.

[29] G. Wang, W. Cong, K. Durairaj, X. Qian, H. Shen, P. Sinn, E. Hoffman, K. McLennan, and M. Henry. *In vivo* mouse studies with bioluminescence tomography. *Optics Express*, 14:7801–7809, 2006.

[30] J. Liu, Y. Wang, X. Qu, X. Li, X. Ma, R. Han, Z. Hu, X. Chen, D. Sun, R. Zhang, D. Chen, D. Chen, X. Chen, J. Liang, F. Cao, and J. Tian. *In vivo* quantitative bioluminescence tomography using heterogeneous and homogeneous mouse models. *Optics Express*, 18:13102–13113, 2010.

[31] M. Keyaerts, I. Remory, V. Caveliers, K. Brekpot, T. J. Bos, J. Poelaert, A. Bossuyt, and T. Lahoutte. Inhibition of firefly luciferase by general anesthestics: Effect on *in vitro* and *in vivo* bioluminescence imaging. *PLoS ONE*, 7:e30061, 2012.

[32] G. Wang, H. Shen, W. Cong, S. Zhao, and G. W. Wei. Temperature-modulated bioluminescence tomography. *Optics Express*, 14:7852–7871, 2006.

[33] M. Keyaerts, C. Heneweer, L. O. Tchouate-Gainkam, V. Caveliers, B. J. Beattie, G. A. Martens, C. Vanhouve, A. Bossuyt, R. Blasberg, and T. Lahoutte. Plasma protein binding of luciferase substrates influences sensitivity and accuracy of bioluminescence imaging. *Mol. Imaging Biol.*, 13:59–66, 2011.

[34] H. Dehghani, S. C. Davis, S. Jiang, B. W. Pogue, K. D. Paulsen, and M. S. Patterson. Spectrally resolved bioluminescence tomography. *Opt. Lett.*, 31:365–367, 2006.

[35] H. Dehghani, M. E. Eames, P. K. Yalavarthy, S. C. Davis, S. Srinivasan, C. M. Carpenter, B. W. Pogue, and K. D. Paulsen. Near infrared optical tomography using

NIRFAST: Algorithm for numerical model and image reconstruction. *Commun. Numer. Meth. Engng.*, 2008.

[36] G. Alexandrakis, F. R. Rannou, and A. F. Chatziionnaou. Effect of optical property estimation accuracy on tomographic bioluminescence imaging: simulation of a combined opticalPET (OPET) system. *Phys. Med. Biol.*, 51:2045–2053, 2006.

[37] M. A. Naser and M. S. Patterson. Algorithm for bioluminescence tomography incorporating anatomical information and reconstruction of tissue optical properties. *Biomedical Optics Express*, 1:512–526, 2010.

[38] Y. Lv, J. Tian, W. Cong, and G. Wang. Experimental study on bioluminescence tomography with multimodality fusion. *International Journal of Biomedical Imaging*, 2007.

[39] Caliper Life Sciences. *Concept Tech Note 6: Planar Spectral Imaging*, 2011.

[40] C. Kuo, O. Coquoz, T. L. Troy, H. Xu, and B. W. Rice. Three-dimensional reconstruction of *in vivo* bioluminescent sources based on multispectral imaging. *Journal of Biomedical Optics*, 12:024007, 2007.

[41] S. Ren, H. Hu, G. Li, X. Cao, S. Zhu, X. Chen, and J. Liang. Multi-atlas registration and adaptive hexahedral voxel discretisation for fast bioluminescence tomography. *Biomedical Optics Express*, 7:1549–1560, 2016.

[42] B. Dogdas, D. Stout, A. F. Chatziionnaou, and R. M. Leahy. Digimouse: A 3D whole body mouse atlas from CT and cryosection data. *Phys. Med. Biol.*, 52:577–587, 2007.

[43] Q. Zhang, L. Yin, Y. Tan, Z. Yuan, and H. Jiang. Quantitative bioluminescence tomography guided by diffuse optical tomography. *Optics Express*, 16:1481–1486, 2008.

[44] M. A. Naser, M. S. Patterson, and J. W. Wong. Algorithm for localized adaptive diffuse optical tomography and its application in bioluminescence tomography. *Phys. Med. Biol.*, 59:2089–2109, 2014.

[45] W. Han, R. Gong, and X. Cheng. A general framework for integration of bioluminescence tomography and diffuse optical tomography. *Inverse Problems in Science and Engineering*, 22:458–482, 2014.

[46] H. Yan, M. B. Unlu, O. Nalcioglu, and G. Gulsen. Bioluminescence tomography with structural and functional *a priori* information. *Proc. of SPIE*, 7557:755712, 2010.

[47] H. Yan, Y. Lin, W. C. Barber, M. B. Unlu, and G.§ Gulsen. A gantry-based tri-modality system for bioluminescence tomography. *Review of Scientific Instruments*, 83:043708, 2012.

[48] J. A. Guggenheim. *Multi-modal diffuse optical tomography and bioluminescence tomography system for preclinical imaging*. PhD thesis, College of Engineering & Physical Sciences, 2014.

[49] J. A. Guggenheim, H. R. A. Basevi, J. Frampton, I. B. Styles, and H. Dehghani. Multimodal molecular diffuse optical tomography system for small animal imaging. *Meas. Sci. Technol.*, 24:10545, 2013.

[50] Hector R. A. Basevi, Kenneth M. Tichauer, Frederic Leblond, Hamid Dehghani, James A. Guggenheim, Robert W. Holt, and Iain B. Styles. Compressive sensing based reconstruction in bioluminescence tomography improves image resolution and robustness to noise. *Biomedical Optics Express*, 3:2131–2141, 2012.

[51] C. Qin, S. Zhu, J. Feng, J. Zhong, X. Ma, P. Wu, and J. Tian. Comparison of permissible source region and multispectral data using efficient bioluminescence tomography method. *J. Biophotonics*, 4:824–839, 2011.

[52] J. Virostko, A. C. Powers, and E. D. Jansen. Validation of luminescent source reconstruction using single-view spectrally resolved bioluminescence images. *Applied Optics*, 46:2540–2547, 2007.

[53] S. M. Liao, S. L. Ferradal, B. R. White, N. Gregg, T. E. Inder, and J. P. Culver. High-density diffuse optical tomography of term infant visual cortex in the nursery. *Journal of Biomedical Optics*, 17:081414, 2012.

[54] S. L. Ferradal, S. M. Liao, A. T. Eggebrecht, J. S. Shimony, T. E. Inder, J. P. Culver, and C. D. Smyser. Functional imaging of the developing brain at the bedside using diffuse optical tomography. *Cerebral Cortex*, pages 1–11, 2015.

[55] A. T. Eggebrecht, S. L. Ferradal, A. Robichaux-Viehoever, M. S. Hassanpour, H. Dehghani, A. Z. Snyder, T. Hershey, and J. P. Culver. Mapping distributed brain function and networks with diffuse optical tomography. *Nature Photonics*, 8:448–454, 2014.

[56] H. Singh, R. J. Cooper, C. W. Lee, L. Dempsey, A. Edwards, S. Brigadoi, D. Airantzis, N. Everdell, A. Michell, D. Holder, J. C. Hebden, and T. Austin. Mapping cortical haemodynamics during neonatal seizures using diffuse optical tomography: A case study. *NeuroImage: Clinical*, 5:256–265, 2014.

[57] V. Ntziachristos, A. G. Yodh, M. Schnall, and B. Chance. Concurrent MRI and diffuse optical tomography of breast after indocynanine green enhancement. *PNAS*, 97:2767–2772, 2000.

[58] T. Huppert, J. Barker, B. Schmidt, S. Walls, and A. Ghuman. Comparison of group-level, source localized activity for simultaneous functonal near-infrared spectroscopy-magnetoencephalography and simultaneous fNIRS-fMRI during parametric median nerve stimulation. *Neurophotonics*, 4:015001, 2017.

[59] M. Chalia, C. W. Lee, L. Dempsey, A. D. Edwards, H. Singh, A. W. Michell, N. L. Everdell, R. W. Hill, J. C. Hebden, T. Austin, and R. J. Cooper. Hemodynamic response to burst-suppressed and discontinuous electroencephalography activity in infant with hypoxic ischemic encephalopathy. *Neurophotonics*, 3:031408, 2016.

[60] Y. Hoshi and Y. Yamada. Overview of diffuse optical tomography and its clinical applications. *Journal of Biomedical Optics*, 21:091312, 2016.

[61] L. Lin, M. Cazzell, O. Babawale, and H. Liu. Automated voxel classification used with atlas-guided diffuse optical tomography for assessment of functional brain networks in young and older adults. *Neurophotonics*, 3:045002, 2016.

[62] A. N. Sen, P. Gopinath, and C. S. Robertson. Clinical application of near-infrared spectroscopy in patients with traumatic brain injury: a review of the progress of the field. *Neurophotonics*, 3:031409, 2016.

[63] B. J. Tromberg, A. Cerussi, N. Shah, M. Compton, A. Durkin, D. Hsiang, J. Butler, and R. Mehta. Diffuse optics in breast cancer: detecting tumors in pre-menopausal women and monitoring neoadjuvant chemotherapy. *Breast Cancer Research*, 7:279–285, 2005.

[64] M. L. Flexman, M. A. Khalil, R. A. Abdi, H. K. Kim, C. J. Fong, E. Desperito, D. L. Hershman, R. L. Barbour, and A. H. Hielscher. Digital optical tomography system for dynamic breast imaging. *Journal of Biomedical Optics*, 16:076014, 2011.

[65] M. E. Eames, B. W. Pogue, C. M. Carpenter, and H. Dehghani. Three dimensional near infrared tomography of the breast. *Proc. SPIE 6629*, 2007.

[66] A. Godavarty, S. Rodriguez, Y.-J. Jung, and S. Gonzalez. Optical imaging for breast cancer prescreening. *Breast Cancer: Targets and Therapy*, 7:193–209, 2015.

[67] W. Zhi, X. Gu, J. Qin, P. Yin, X. Sheng, and Q. Gao, S. P. an Li. Solid breast lesions: Clinical experience with US-guided diffuse optical tomography combined with conventional US. *Radiology*, 262:371–378, 2012.

[68] A. D. Klose, A. H. Hielscher, K. M. Hanson, and J. Beuthan. Two- and three-dimensional optical tomography of finger joints for diagnostics of rheumatoid arthritis. *Proc. SPIE 3566, Photon Propagation in Tissues IV*, 1998.

[69] A. H. Hielscher, H. K. Kim, L. D. Montejo, S. Blaschke, U. J. Netz, P. A. Zwaka, G. Illing, G. A. Muller, and J. Beuthan. Frequency-domain optical tomographic imaging of arthritic finger joints. *IEEE Transactions on Medical Imaging*, 30:1725–1736, 2011.

[70] Q. Zhang, Z. Yuan, E. S. Sobel, and H. Jiang. Three-dimensional diffuse optical tomography of osteoarthritis: a study of 38 finger joints. *Proc. SPIE 7166, Optics in Bone Biology and Diagnostics*, 2009.

[71] H. Y. Wu, A. Filer, I. Styles, and H. Dehghani. Development of multispectral diffuse optical tomography system for early diagnosis of rheumatoid arthritis. *In Biomedical Optics (pp. BM3A-47). Optical Society of America*, 2014.

[72] X. Gu, Q. Zhang, L. Larcom, and H. Jiang. Three-dimensional bioluminescence tomography with model-based reconstruction. *Optics Express*, 12:3996–4000, 2004.

[73] J. Feng, K. Jia, C. Qin, G. Yan, S. Zhu, X. Zhang, J. Liu, and J. Tian. Three-dimensional bioluminescence tomography based on bayesian approach. *Optics Express*, 17:16834–16848, 2009.

[74] R. Han, J. Liang, X. Qu, Y. Hou, N. Ren, J. Mao, and J. Tian. A source reconstruction algorithm based on adaptive *hp*-FEM for bioluminescence tomography. *Optics Express*, 17:14481–14494, 2009.

[75] Caliper Life Sciences. *Biology Tech Note 1: Kinetic Analysis of Bioluminescent Sources*, 2008.

[76] J. S. Burgos, M. Rosol, R. A. Moats, V. Khankalyyan, D. B. Kohn, M. D. Jr Nelson, and W. E. Laug. Time course of bioluminescent signal in orthotopic and heterotopic brain tumors in nude mice. *BioTechniques*, 34:1184–1188, 2003.

[77] A. J. Chaudhari, F. Darvas, J. R. Bading, R. A. Moats, P. S. Conti, D. J. Smith, S. R. Cherry, and R. M. Leahy. Hyperspectral and multispectral bioluminescence optical tomography for small animal imaging. *Phys. Med. Biol.*, 50:5421–5441, 2005.

[78] C. Li, G. S. Mitchell, J. Dutta, S. Ahn, R. M. Leahy, and S. R. Cherry. A three-dimensional multispectral fluorescence optical tomography imaging system for small animals based on a conical mirror design. *Optics Express*, 17:7571–7585, 2009.

[79] G. Wang, H. Shen, K. Durairaj, X. Qian, and W. Cong. The first bioluminescence tomography system for simultaneous acquisition of multiview and multispectral data. *International Journal of Biomedical Imaging*, pages 1–8, 2006.

[80] A. D. Klose, B. J. Beattie, H. Dehghani, L. Vider, C. Le, V. Ponomarev, and R. Blasberg. *In vivo* bioluminescence tomography with a blocking-off finite-difference SP_3 method and mri/ct coregistration. *Med. Phys.*, 37:329–338, 2010.

[81] L. Cao and J. Peter. Bayesian reconstruction strategy of fluorescence-mediated tomography using an integrated SPECT-CT-OT system. *Phys. Med. Biol.*, 55:2693–2708, 2010.

[82] Y. Lu, I-C. Tan, C. Darne, B. Zhu, N. Wilganowski, H. Robinson, J. Rasmussen, and E. Sevick. Multimodal tomography of orthotopic prostate cancer with far-red fluorescent gene reporter using an optical/PET/CT scanner. *J. Nucl. Med.*, 53 (Supplement 1), 2012.

[83] H. R. A. Basevi, J. A. Guggenheim, H. Dehghani, and I. B. Styles. Simultaneous multiple view high resolution surface geometry acquisition using structured light and mirrors. *Optics Express*, 21:7222–7239, 2013.

[84] Caliper Life Sciences. *Tech Note 4b: Bioluminescence Tomography - Topography*, 2009.

[85] J. Pekar. *Multispectral bioluminescence tomography with X-ray CT spatial priors*. PhD thesis, McMaster University, 2011.

[86] J. Chen, V. Venugopal, F. Lesage, and X. Intes. Time-resolved diffuse optical tomography with patterned-light illumination and detection. *Optics Letters*, 35:2121–2123, 2010.

[87] V. Venugopal, J. Chen, and X. Intes. Development of an optical imaging platform for functional imaging of small animals using wide-field excitation. *Biomedical Optics Express*, 1:143–156, 2010.

[88] Caliper Life Sciences. *IVIS Spectrum User Manual*, 2009.

[89] Caliper Life Sciences. *Tech Note 4c: Bioluminescence Tomography - Source Reconstruction and Analysis*, 2009.

[90] Caliper Life Sciences. *Tech Note 4: Fluorescent Imaging*, 2011.

[91] T. A. Sasser, J. McHattan, and J. Waldeck. *The Bruker In-Vivo Xtreme II System for Flexible and Sensitive Multimodal Preclinical Imaging*. Bruker BioSpin, November 2015.

[92] Bruker BioSpin. In-Vivo Xtreme II: Flexible imaging to support evolving research, January 2017.

[93] Biospace. Biospace lab: PhotonIMAGER-TM: The next generation of optical imagers, 2015.

[94] LICOR. Pearl trilogy: Near-infrared fluorescent and bioluminescent small animal imaging system, 2015.

[95] LICOR. *Pearl Trilogy: Pearl Trilogy Imaging System Operator's Manual*, December 2016.

[96] S. L. Taylor, S. K. G. Mason, S. L. Glinton, M. Cobbold, and H. Dehghani. Accounting for filter bandwidth improves the quantitative accuracy of bioluminescence tomography. *Journal of Biomedical Optics*, 20:096001, 2015.

[97] H. R. A. Basevi. *Use of prior information and probabilistic image reconstruction for optical tomographic imaging*. PhD thesis, College of Engineering & Physical Sciences, 2015.

[98] I. H. J. Ploemen, M. Prudencio, B. G. Douradinha, J. Ramesar, J. Fonanger, G.-J. van Gemert, A. J. F. Luty, C. C. Hermsen, R. W. Sauerwein, F. G. Baptista, M. M. Mota, A. P. Waters, I. Que, C. W. G. M. Lowik, S. M. Kahn, C. J. Janse, and B. M. D. Franke-Fayard. Visualisation and quantitative analysis of the rodent malaria liver stage by real time imaging. *PLoS ONE*, 4:e7881, 2009.

[99] Caliper Life Sciences. *Biology Tech Note 2: IVIS Imaging Protocols*, 2009.

[100] A. Van Praagh, A. Bahadur, M. Saaussan, and T. A. Sasser. Monitoring lung tumor progression from onset to late stage, and *ex vivo* using complementary bioluminescence-, fluorescence-, and microct imaging. Technical report, Bruker, 2017.

[101] Z. Bai, Y. Shi, J. Wang, L. Qiu, E. J. Monroe, G. Teng, F. Zhang, and X. Yang. Intratumoral radiofrequency hyperthermia-enhanced direct chemotherapy of pancreatic cancer. *Oncotarget*, 8:3591–3599, 2016.

[102] Y. Vedvyas, E. Shevlin, M. Zaman, I. M. Min, A. Amor-Coarasa, S. Park, S. Park, K.-W. Kwon, T. Smith, Y. Luo, D. Kim, Y. Kim, B. Law, R. Ting, J. Babich, and M. M. Jin. Longitudinal pet imaging demonstrates biphasic car t cell rresponse in survivors. *JCI Insight*, 1:e90064, 2016.

[103] Bruker BioSpin. Preclinical *in vivo* imaging, January 2014.

[104] M. Keyaerts, J. Verschueren, T. J. Bos, L. O. Tchouate-Gainkam, C. Peleman, K. Brekpot, C. Vanhove, V. Caveliers, A. Bossuyt, and T. Lahoutte. Dynamic bioluminescence imaging for quantitative tumour brurden assessment using iv or ip administration of d-luciferin: effect on intensity, time kkinetic and repeatability of photon emission. *European Journal of Nuclear Medicine and Molecular Imaging*, 35:999–1007, 2008.

[105] M.-A. Shibata, E. Shibata, J. Morimoto, N. A. S. Eid, Y. Tanaka, M. Watanabe, and Y. Otsuki. An immunocompetent murine model of metastatic mammary cancer accessible to bioluminescence imaging. *Anticancer Research*, 29:4389–4396, 2009.

[106] A. Tennestaedt, M. Aswendt, J. Adamczak, and M. Hoehn. Noninvasive multimodal imaging of stem cell transplants in the brain using bioluminescence imaging and magnetic resonance imaging. *Methods Molecular Biology*, 1052:153–166, 2013.

[107] M. Aswendt, J. Adamczak, S. Couillard-Despres, and M. Hoehn. Boosting bioluminescence neuroimaging: An optimized protocol for brain studies. *PLoS ONE*, 8:e55662, 2013.

[108] K. M. Tichauer, R. W. Holt, F. El-Ghussein, Q. Zhu, H. Dehghani, F. Leblond, and B. W. Pogue. Imaging workflow and calibration for CT-guided time-domain fluorescence tomography. *Biomedical Optics Express*, 2:3021–3036, 2011.

[109] V. Ntziachristos and R. Weissleder. Experimental three-dimensional fluorescence reconstruction of diffuse media by use of a normalised Born approximation. *Optics Letters*, 26:893–895, 2001.

[110] V. Ntziachristos. Going deeper than microscopy: the optical imaging frontier in biology. *Nature Methods*, 7:603–614, 2010.

[111] K. M. Tichauer, R. W. Holt, K. S. Samkoe, F. El-Ghussein, J. R. Gunn, M. Jermyn, H. Dehghani, F. Leblond, and B. W. Pogue. Computed tomography-guided time-domain diffuse fluorescence tomography in small animals for localization of cancer biomarkers. *Journal of Visualized Experiments*, 65:e4050, 2012.

[112] T. Troy, D. Jekic-McMullen, L. Sambucetti, and B. Rice. Quantitative comparison of the sensitivity of detection of fluorescent and bioluminescent reporter in animal models. *Molecular Imaging*, 3:9–23, 2004.

[113] X. Chen, P. S. Conti, and R. A. Moats. *In vivo* near-infrared fluorescence imaging of integrin alpha-v-beta-3 in brain tumor xenografts. *Cancer Res.*, 64:8009–8014, 2004.

[114] M. H. Katz, S. Takimoto, D. Spivack, A. R. Moossa, R. M. Hoffman, and M. Bouvet. A novel red fluorescent protein orthotopic pancreatic cancer model for the preclinical evaluation of chemotherapeutics. *Journal of Surgical Research*, 113:151–160, 2003.

[115] D. Hyde, R. de Kleine, S. A. MacLaurin, E. Miller, D. H. Brooks, T. Krucker, and V. Ntziachristos. Hybrid FMT-CT imaging of amyloid-beta plaques in a murine Alzheimer's disease model. *Neuroimage*, 44:1304–1311, 2009.

[116] J. Chen, C-H. Tung, U. Mahmood, V. Ntziachristos, R. Gyurko, M. C. Fishman, P. L. Huang, and R. Weissleder. *In vivo* imaging of proteolytic activity in atherosclerosis. *Circulation*, 105:2766–2771, 2002.

[117] K. M. Tichauer, K. S. Samkoe, K. J. Sexton, J. R. Gunn, T. Hasan, and B. W. Pogue. Improved tumor contrast achieved by single time point dual-reported fluorescence imaging. *Journal of Biomedical Optics*, 17:066001, 2012.

[118] K. M. Tichauer, K. S. Samkoe, K. J. Sexton, S. K. Hextrum, H. H. Yang, W. S. Klubben, J. R. Gunn, T. Hasan, and B. W. Pogue. *In vivo* quantification of tumor receptor binding potential with dual-reporter molecular imaging. *Mol. Imaging Biol.*, 14:584–592, 2012.

[119] F. Leblond, S. C. Davis, P. A. Valdes, and B. W. Pogue. Preclinical whole-body fluorescence imaging: Review of instruments, methods and applications. *J. Photochem. Photobiol. B*, 98:77–94, 2010.

[120] D. Kepshire, N. Mincu, M. Hutchins, J. Gruber, H. Dehghani, J. Hypnarowski, F. Leblond, M. Khayat, and B. W. Pogue. A microcomputed tomography guided fluorescence tomography system for small animal molecular imaging. *Review of Scientific Instruments*, 80:043701, 2009.

[121] D. W. McRobbie, E. A. Moore, M. J. Graves, and M. R. Prince. *MRI: From Picture to Proton*. Cambridge University Press, 2009.

[122] B. D. Ross, B. A. Moffat, T. S. Lawrence, S. K. Mukherji, S. S. Gebarski, D. J. Quint, T. D. Johnson, L. Junck, P. L. Robertson, K. M. Muraszko, Q. Dong, C. R. Meyer, P. H. Bland, P. McConville, H. Geng, A. Rehemtulla, and T. L. Chenevert. Evaluation of cancer therapy using diffusion magnetic resonance imaging. *Molecular Cancer Therapeutics*, 2:581–587, 2003.

[123] M. Neeman. Preclinical MRI experience in imaging angiogenesis. *Cancer and Metastasis Reviews*, 19:39–43, 2000.

[124] S. J. Zhang and J. C. Wu. Comparison of imaging techniques for tracking cardiac stem cell therapy. *J Nucl Med*, 48:1916–1919, 2007.

[125] E. T. Ahrens and J. W. M. Bulte. Tracking immune cells *in vivo* using magnetic resonance imaging. *Nature Reviews*, 13:755–763, 2013.

[126] D. P. Cardenas, E. R. Muir, S. Huang, A. Boley, D. Lodge, and T. Q. Duong. Functional MRI during hyperbaric oxygen: Effects of oxygen on neurovascular coupling and BOLD fMRI signals. *NeuroImage*, 119:382–389, 2015.

[127] C. Fennema-Notestine, D. J. Hagler Jr., L. K. McEvoy, A. S. Fleisher, E. H. Wu, D. S. Karow, A. M. Dale, and Alzheimer's Disease Neuroimaging Initiative. Structural MRI biomarkers for preclinical and mild Alzheimer's disease. *Human Brain Mapping*, 30:3238–3253, 2009.

[128] A. Rehemtulla, L. D. Stegman, S. J. Cardozo, S. Gupta, D. E. Hall, C. H. Contag, and B. D. Ross. Rapid and quantitative assessment of cancer treatment response using *in vivo* bioluminescence imaging. *Neoplasia*, 2:491–495, 2000.

[129] J. Zhang, D. Chen, J. Liang, H. Xue, J. Lei, Q. Wang, D. Chen, M. Meng, Z. Jin, and J. Tian. Incorporating MRI structural information into bioluminescence tomography: system, heterogeneous reconstruction and *in vivo* quantification. *Biomedical Optics Express*, 5:1861–1876, 2014.

[130] M. Allard, D. Cote, L. Davidson, J. Dazai, and R. M. Henkelman. Combined magnetic resonance and bioluminescence imaging of live mice. *Journal of Biomedical Optics*, 12:034018, 2007.

[131] PerkinElmer. *IVIS Spectrum Pre-clinical In Vivo Imaging System*, 2013.

[132] C. H. Szentirmai, O. Baker, N. Lin, S. Szucs, M. Takahashi, S. Kiryu, A. L. Kung, R. C. Mulligan, and B. S. Carter. Noninvasive bioluminescence imaging of luciferase expressing intracranial U87 xenografts: correlation with magnetic resonance imaging determined tumor volume and longitudinal use in assessing tumor growth and antiangiogenic treatment effect. *Neurosurgery*, 58:365–72, 2006.

[133] D. R. Dance, S. Christofides, A. D. A. Maidment, I. D. McLean, and K. H. Ng, editors. *Diagnostic Radiology Physics: A Handbook for Teachers and Students*. International Atomic Energy Agency, 2014.

[134] Computed tomography (CT), October 2016.

[135] C. A. Wathen, N. F. Foje, T. van Avermaete, B. Miramontes, S. E. Chapaman, T. A. Sasser, R. Kannan, S. Gerstler, and W. M. Leevy. *In vivo* X-ray computed tomographic imaging of soft tissue with native, intravenous, or oral contrast. *Sensors*, 13:6957–6980, 2013.

[136] M. J. Paulus, S. S. Gleason, S. J. Kennel, P. R. Hunsicker, and D. K.1 Johnson. High resolution X-ray computed tomography: An emerging tool for small animal cancer research. *Neoplasia*, 2:62–70, 2000.

[137] N. M. Das, S. Hatsell, K. Nannuru, L. Huang, X. Wen, L. Wang, L.-H. Wang, V. Idone, J. A. Meganck, A. Murphy, A. Economides, and L. Xie. *In vivo* quantitative microcomputed tomographic analysis of vasculature and organs in a normal and disease mouse model. *PLoS ONE*, 11:e0150085, 2016.

[138] D. W. Holdsworth and M. M. Thornton. Micro-CT in small animal and specimen imaging. *Trends in Biotechnology*, 20:S34–S39, 2002.

[139] D. P. Clark, K. Ghaghada, E. J. Moding, D. G. Kirsch, and C. T. Badea. *In vivo* characterization of tumor vasculature using iodine and gold nanoparticles and dual energy micro-CT. *Phys. Med. Biol.*, 58:1683–1704, 2013.

[140] E. L. Ritman. Micro-computed tomography of the lungs and pulmonary-vascular system. *Proc. Am. Thorac. Soc.*, 2:477–480, 2005.

[141] B. Vandeghinste, B. Trachet, M. Renard, C. Casteleyn, S. Staelens, B. Loeys, P. Segers, and S. Vandenberghe. Replacing vascular corrosion casting by *in vivo* micro-CT imaging for building 3D cardiovascular models in mice. *Mol. Imaging Biol.*, 13:78–86, 2011.

[142] E. De Langhe, G. V. Vande, J. Hostens, U. Himmelreich, B. Nemery, F. P. Luyten, J. Vanoirbeek, and R. J. Lories. Quantification of lung fibrosis and emphysema in mice using automated micro-computed tomography. *PLoS ONE*, 7:e43123, 2012.

[143] X. Artaechevarria, D. Blanco, G. de Biurrun, M. Ceresa, D. Perez-Martin, G. Bastarrika, J. P. de Torres, J. J. Zulueta, L. M. Montuenga, C. Ortiz-de Solorzano, and A. Munoz-Barrutia. Evaluation of micro-CT for emphysema assessment in mice: comparison with non-radiological techniques. *Eur. Radiol*, 21:954–962, 2011.

[144] A. C. Antill, D. H. Ballard, A. M. Hollister, E. J. Rogers, S. Yang, and S. J. Lokitz. Micro-CT evaluation of rheumatoid arthritis mouse model disease progression: Manual tracings versus semi-automated routines. *Diagnostic and Interventional Imaging*, 97:651–655, 2016.

[145] James Brown. *Articulated statistical shape models for the analysis of bone destruction in mouse models of rheumatoid Arthritis*. PhD thesis, College of Engineering & Physical Sciences, 2015.

[146] I. Szanda, J. Mackewn, G. Patay, P. Major, K. Sunassee, G. E. Mullen, G. Nemeth, Y. Haemisch, P. J. Blower, and P. K. Marsden. National electrical manufacturers

association NU-4 performance evaluation of the pet component of the nanoPET/CT preclinical PET/CT scanner. *J. Nucl. Med.*, 52:1741–1747, 2011.

[147] T. Maina, H. Bergsma, H. R. Kulkarni, D. Mueller, D. Charalambidis, E. P. Krenning, B. A. Nock, M. de Jong, and R. P. Buam. Preclinical and first clinical experience with the gastrin-releasing peptide receptor-antagonist 68-Ga-SB3 and PET/CT. *Eur. J. Nucl. Med. Mol. Imaging*, 43:964–973, 2016.

[148] C. M. Deroose, A. De, A. M. Loening, P. L. Chow, P. Ray, A. F. Chatziionnaou, and S. S. Gambhir. Multimodality imaging of tumor xenografts and metastases in mice with combined small-animal PET, small-animal CT, and bioluminescence imaging. *J. Nucl. Med.*, 48:295–303, 2007.

[149] Q. Zhu, H. Dehghani, K. M. Tichauer, R. W. Holt, K. Vishwanath, F. Leblond, and B. W. Pogue. A three-dimensional finite element model and image reconstruction algorithm for time-domain fluorescence imaging in hihigh scattering media. *Phys. Med. Biol.*, 56:7419–7434, 2011.

[150] D. J. Rowland and S. R. Cherry. Small-animal preclinical nuclear medicine instrumentation and methodology. *Semin. Nucl. Med.*, 38:209–222, 2008.

[151] A. F. Chatziionnaou. Instrumentation for molecular imaging in preclinical research: Micro-PET and micro-CT. *Proceedings of the American Thoracic Society*, 2:533–536, 2005.

[152] S. S. Gambhir. Molecular imaging of cancer with positron emission tomography. *Nature Reviews*, 2:683–693, 2002.

[153] F. J. Beekman, F. van der Have, B. Vastenhouw, A. J. A. van der Linden, P. P. van Rijk, J. P. H. Burbach, and M. P. Smidt. U-SPECT-I: A novel system for submillimeter-

resolution tomography with radiolabeled molecules in mice. *J. Nucl. Med.*, 46:1194–1200, 2005.

[154] M. Hofmann, K. C. Wollert, G. P. Meyer, A. Menke, L. Arseniev, B. Hertenstein, A. Ganser, W. H. Knapp, and H. Drexler. Monitoring of bone marrow cell homing into the infarcted human myocardium. *Circulation*, 111:2198–2202, 2005.

[155] N. Tran, S. Poussier, P. R. Franken, F. Maskali, F. Groubatch, C. Vanhouve, L. Antunes, G. Karcher, J-P. Villemot, and P-Y. Marie. Feasibility of *in vivo* dual-energy myocardial SPECT for monitoring the distribution of transplanted cells in relation to the infarction site. *Eurpoean Journal of Nuclear Medicine and Molecular Imaging*, 33:709–715, 2006.

[156] M. M. Welling, M. Duijvestein, A. Signore, and L. van der Weerd. *In vivo* biodistribution of stem cells using molecular nuclear medicine imaging. *J. Cell. Physiol.*, 226:1444–1452, 2011.

[157] B. H. Hasegawa, K. H. Wong, K. Iwata, W. C. Barber, A. B. Hwang, A. E. Sakdinawat, M. Ramaswamy, D. C. Price, and R. A. Hawkins. Dual-modality imaging of cancer with SPECT/CT. *Technology in Cancer Research & Treatment*, 1, 2002.

[158] M. Shokeen and C. J. Anderson. Molecular imaging of cancer with copper-64 radiopharmaceuticals and positron emission tomography (PET). *Accounts of Chemical Research*, 42:832–841, 2009.

[159] C. C. Rowe, U. Ackerman, W. Browne, R. Mulligan, K. L. Pike, G. O'Keefe, H. Tochon-Danguy, G. Chan, S. U. Berlangieri, G. Jones, K. L. Dickinson-Rowe, H. P. Kung, W. Zhang, M. P. Kung, D. Skovronsky, T. Dyrks, G. Holl, S. Krause, M. Friebe, L. Lehman, S. Lindemann, L. M. Dinkelborg, C. L. Masters, and V. L. Villemagne.

Imaging of amyloid-beta in Alzheimer's disease with 18-F-BAY94-9172, a novel PET tracer: proof of mechanism. *Lancet Neurology*, 7:129–135, 2008.

[160] V. L. Villemagne, K. E. Pike, D. Darby, P. Maruff, G. Savage, S. Ng, U. Ackerman, T. F. Cowie, J. Currie, S. G. Chan, G. Jones, H. Tochon-Danguy, G. O'Keefe, C. L. Masters, and C. C. Rowe. A-beta deposits in older non-demented individuals with cognitive decline are indicative of preclinical Alzheimer's disease. *Neuropsychologia*, 46:1688–1697, 2008.

[161] S-C. Huang, D. Truong, H-M. Wu, A. F. Chatziionnaou, W. Shao, A. M. Wu, and M. E. Phelps. An internet-based "kinetic imaging system" (KIS) for microPET. *Mol. Imaging Biol.*, 7:330–341, 2005.

[162] P. E. Kinahan, M. Defrise, and R. Clackdoyle. *Emission Tomography: The Fundamentals of PET and SPECT, Chapter 20: Analytic Image Reconstruction Methods*. Elsevier Inc., 2004.

[163] E. U. Mumcuoglu, R. M. Leahy, and S. R. Cherry. Bayesian reconstruction of PET images: methodology and performance analysis. *Phys. Med. Biol.*, 41:1777–1807, 1996.

[164] K. Thielemans, C. Tsoumpas, S. Mustafovic, T. Biesel, P. Aguiar, N. Dikaios, and M. W. Jacobson. STIR: software for tomographic image reconstruction release 2. *Phys. Med. Biol.*, 57:867–883, 2012.

[165] D. W. Townsend. Dual-modality imaging: Combining anatomy and function. *J. Nucl. Med.*, 49:938–955, 2008.

[166] J. Culver, W. Akers, and S. Achilefu. Multimodality molecular imaging with combined optical and SPECT/PET modalities. *J. Nucl. Med.*, 49:169–172, 2008.

[167] S. Lee, S-W. Kang, J. H. Ryu, J. H. Na, D-E. Lee, S. J. Han, C. M. Kang, Y. S. Choe, K. C. Lee, J. F. Leary, K. Choi, K-H. Lee, and K. Kim. Tumor-homing glycol chitosan-based optical/PET dual imaging nanoprobe for cancer diagnosis. *Bioconjugate Chemistry*, 25:601–610, 2014.

[168] K. Ferrara, R. Pollard, and M. Borden. Ultrasound microbubble contrast agents: Fundamentals and application to gene and drug delivery. *Annu. Rev. Biomed. Eng.*, 9:415–447, 2007.

[169] K. C. Graham, L. A. Wirtzfeld, and L. T. MacKenzie. Three-dimensional high-frequency ultrasound imaging for longitudinal evaluation of liver metastases in pre-clinical models. *Cancer Res.*, 65:5231–5237, 2005.

[170] L. A. Wirtzfeld, G. Wu, M. Bygrave, Y. Yamasaki, H. Sakai, M. Moussa, J. I. Izawa, D. B. Downey, N. M. Greenberg, A. Fenster, J. W. Xuan, and J. C. Lacefield. A new three-dimensional ultrasound microimaging technology for preclinical studies using a transgenic prostate cancer mouse model. *Cancer Res*, 65:6337–6345, 2005.

[171] F. S. Foster, J. Hossack, and S. L. Adamson. Micro-ultrasound for pre-clinical imaging. *Interface Focus*, 2011.

[172] O. F. Kaneko and J. K. Willmann. Ultrasound for molecular imaging and therapy in cancer. *Quant Imaging Med Surg*, 2:87–97, 2012.

[173] A. Greco, M. Mancini, S. Gargiulo, M. Gramanzini, P. P. Claudio, A. Brunetti, and M. Salvatore. Ultrasound biomicroscopy in small animal research: Applications in molecular and preclinical imaging. *Journal of Biomedicine and Biotechnology*, 2012.

[174] N. Deshpande, A. Needles, and J. K. Willmann. Molecular ultrasound imaging: current status and future directions. *Clinical Radiology*, 65:567–581, 2010.

[175] A. Barua, A. Yellapa, J. M. Bahr, M. K. Adur, C. W. Utterback, P. Bitterman, S. Basu, S. Sharma, and J. S. Abramowicz. Interleukin 16- (il-16-) targeted ultrasound imaging agent improves detection of ovarian tumors in laying hens, a preclinical model of spontaneous ovarian cancer. *BioMed Research International*, 2015.

[176] L. V. Wang and S. Hu. Photoacoustic tomography: *In vivo* imaging from organelles to organs. *Science*, 335:1458–1462, 2012.

[177] P. K. Upputuri and M. Pramanik. Recent advances toward preclinical and clinical translation of photoacoustic tomography: a review. *Journal of Biomedical Optics*, 22:041006, 2017.

[178] S. Mallidi, G. P. Luke, and S. Emelianov. Photoacoustic imaging in cancer detection, diagnosis, and treatment guidance. *Trends in Biotechnology*, 29:213–221, 2011.

[179] J. Laufer, P. Johnson, E. Zhang, B. Treeby, B. Cox, B. Pedley, and P. Beard. *In vivo* preclinical photoacoustic imaging of tumour vasculature development and therapy. *Journal of Biomedical Optics*, 17:056016, 2012.

[180] T. Wang, N. Sun, R. Cao, B. Ning, R. Chen, Q. Zhou, and S. Hu. Multiparametric photoacoustic microscopy of the mouse brain with 300-kHz A-line rate. *Neurophotonics*, 3:045006, 2016.

[181] S. Hu and L. V. Wang. Photoacoustic imaging and characterization of the microvasculature. *Journal of Biomedical Optics*, 15, 2009.

[182] B. Zabihian, Z. Chen, E. Rank, C. Sinz, M. Bonesi, H. Sattmann, J. Ensher, M. P. Minnemann, E. Hoover, J. Weingast, L. Ginner, R. Leitgeb, H. Kittler, E. Zhang, P. Beard, W. Drexler, and M. Liu. Comprehensive vascular imaging using optical coherence tomography-based angiography and photoacoustic tomography. *Journal of Biomedical Optics*, 21:096011, 2016.

[183] J. A. Guggenheim, T. J. Allen, A. Plumb, E. Z. Zhang, M. Rodriguez-Justo, S. Punwani, and P. Beard. Photoacoustic imaging of human lymph nodes with endogenous lipid and hemoglobin contrast. *Journal of Biomedical Optics*, 20:050504, 2015.

[184] M. Nasiriavanaki, J. Xia, H. Wan, A. Q. Bauer, J. Culver, and L. V. Wang. High-resolution photoacoustic tomography of resting-state functional connectivity in the mouse brain. *PNAS*, 111:21–26, 2014.

[185] L. Xiang, B. Wang, L. Ji, and H. Jiang. 4-D photoacoustic tomography. *Scientific Reports*, 3:1113, 2013.

[186] M. Firbank. *The design, calibration and usage of a solid scattering and absorbing phantom for near infra red spectroscopy.* PhD thesis, Department of Medical Physics and Bioengineering, 1994.

[187] T. Durduran, R. Choe, W. B. Baker, and A. G. Yodh. Diffuse optics for tissue monitoring and tomography. *Rep. Prog. Phys.*, 73:076701, 2010.

[188] A. Yodh and B. Chance. Spectroscopy and imaging with diffusing light. *Physics Today*, 48:34–40, 1995.

[189] H. Dehghani, S. Srinivasan, B. W. Pogue, and A. Gibson. Numerical modelling and image reconstruction in diffuse optical tomography. *Phil. Trans. R. Soc. A*, 367:3073–3093, 2009.

[190] J. Ripoll, R. B. Schulz, and V. Ntziachristos. Free-space propagation of diffuse light: Theory and experiments. *Phys. Rev. Lett.*, 91:103901, 2003.

[191] X. Chen, X. Gao, X. Qu, J. Liang, L. Wang, D. Yang, A. Garofalakis, J. Ripoll, and J. Tian. A study of photon propagation in free-space based on hybrid radiosity-radiance theorem. *Optics Express*, 17:16266–16280, 2009.

[192] X. Chen, X. Gao, X. Qu, D. Chen, X. Ma, J. Liang, and J. Tian. Generalized free-space diffusion photon transport model based on the influence analysis of a camera lens diaphragm. *Applied Optics*, 49:5654–5664, 2010.

[193] C. Qin, J. Feng, S. Zhu, X. Ma, J. Zhong, P. Wu, Z. Jin, and J. Tian. Recent advances in bioluminescence tomography: methodology and system as well as application. *Laser Photonics Rev.*, 8:94–114, 2014.

[194] T. O. McBride. *Spectroscopic Reconstructed Near Infrared Tomographic Imaging for Breast Cancer Diagnosis*. PhD thesis, Thayer School of Engineering, 2001.

[195] Q. Chen, F. Li, F. Zhou, W. Wang, Y. Xu, W. Sun, and Y. Zhou. Construction of a tumor-specific bioluminescent eukaryotic expression vector and analysis of its expression *in vitro* and *in vivo*. *Oncology Letters*, 6:207–211, 2013.

[196] S. L. Taylor, S. K. G. Mason, S. L. Glinton, M. Cobbold, I. B. Styles, and H. Dehghani. Optimisation of acquisition time in bioluminescence imaging. *Proc. SPIE 9319, Optical Tomography and Spectroscopy of Tissue XI, 93191T*, 2015.

[197] J. A. Guggenheim, I. Baragigia, A. Farina, A. Pifferi, and H. Dehghani. Time resolved diffuse optical spectroscopy with geometrically accurate models for bulk parameter recovery. *Biomedical Optics Express*, 7:3784–3794, 2016.

[198] Shelley L. Taylor, Philip N. Newsome, and Hamid Dehghani. Development of a multi-modal optical imaging system. In *Biomedical Optics 2016*, page OTu2C.2. Optical Society of America, 2016.

[199] G. Alexandrakis, F. R. Rannou, and A. F. Chatziionnaou. Tomographic bioluminescence imaging by use of a combined optical-PET (OPET) system: a computer simulation feasibility study. *Phys. Med. Biol.*, 50:4225–4241, 2005.

[200] H. Dehghani, F. Leblond, B. W. Pogue, and F. Chauchard. Application of spectral derivative data in visible and near infrared spectroscopy. *Phys. Med. Biol.*, 55:3381–3399, 2010.

[201] H. Xu, B. W. Pogue, R. Springett, and H. Dehghani. Spectral derivative based image reconstruction provides inherent insensitivity to coupling and geometric errors. *Optics Letters*, 30:2912–2914, 2005.

[202] H. Dehghani, B. W. Pogue, J. Shudong, B. Brooksby, and K. D. Paulsen. Three-dimensional optical tomography: resolution in small-object imaging. *Applied Optics*, 42:3117–3128, 2003.

[203] A. E. F. Taylor. *Illumination Fundamentals: 4. Basic Radiometric and Photometric Measurement*. Rensselaer Polytechnice Institute, 2000.